

DESIGN AND DEVELOPMENT OF BOTTLEBRUSH POLYMERS
FOR ADVANCED TECHNOLOGIES

A Dissertation

by

NARI KANG

Submitted to the Office of Graduate and Professional Studies of
Texas A&M University
in partial fulfillment of the requirements for the degree of

DOCTOR OF PHILOSOPHY

| | |
|---------------------|---------------------|
| Chair of Committee, | Karen L. Wooley |
| Committee Members, | Yossef A. Elabd |
| | Lei Fang |
| | Jodie L. Lutkenhaus |
| | Hung-Jue Sue |
| Head of Department, | Ibrahim Karaman |

August 2020

Major Subject: Materials Science and Engineering

Copyright 2020 Nari Kang

ABSTRACT

Bottlebrush polymers or molecular bottlebrushes are unique polymers with a complex architecture. This cylindrical bottlebrush structure can be constructed *via* a “bottom-up” method through controlled radical polymerizations to synthesize macromonomers, followed by living ring-opening olefin metathesis polymerizations of macromonomer frameworks. This “bottom-up” synthetic strategy allows bottlebrush polymers to be deliberately designed to tailor their properties and their site-specific functionalization. The compositions and dimensions of bottlebrush polymers can be refined with a high degree of control over the synthetic chemistry using predetermined kinetic parameters of living free radical polymerizations throughout synthetic pathways.

Additionally, the functionalities of bottlebrush polymers can be determined by a wide selection of functional monomers which can be used as building blocks for bottlebrush polymer fabrication. Employing a series of monomers with varied functionalities, from the wide range of choices, enables the realization of numerous potential applications of bottlebrush polymers. The new design, fabrication and scientific investigation of bottlebrush polymer systems for several advanced technologies will be explored and presented in this dissertation—hole transport materials for organic light-emitting diodes (Chapter II), porous membranes for gas adsorption and separation (Chapter III), and amphiphilic BBPs with high graft densities as potential templating materials for the anisotropic growth of inorganic nanoparticles (Chapter IV). Each

bottlebrush macromolecule includes one or more functional moieties that assume a role to improve device performances.

DEDICATION

To my family

ACKNOWLEDGEMENTS

First, I sincerely appreciate my great advisor Dr. Karen L. Wooley, for her substantial support, guidance, and patience during my graduate study at Texas A&M University. It has been a great honor to work in Wooley group having her as my advisor. I also would like to thank my committee members, Dr. Yossef A. Elabd, Dr. Lei Fang, Dr. Jodie L. Lutkenhaus, and Dr. Hung-Jue Sue for their guidance and support throughout the course of my Ph.D. research. And I acknowledge Dr. Micah J. Green and Dr. Quentin Michaudel for their intellectual discussion and time as serving as substituted committee members for my oral examination, of the preliminary exam and the final defense, respectively.

I would like to acknowledge Dr. Guorong Sun for his great contribution and support as my mentor and Dr. Eric E. Leonhardt for his help and implemental discussion to make our collaboration fruitful and exciting. I want to thank my collaborators from DuPont or Dow Chemical Company, Dr. Peter Trefonas, Dr. Mingqi Li, Dr. Liam P. Spencer, and Dr. W. Hunter Woodward for their helpful discussions on our collaborative work.

My gratitude also goes to past and present Wooley group members, especially Mei Dong, Yen-Nan Lin, Tan Nguyen, Yue Song, Mariela Vazquez for making my time at Texas A&M University enjoyable and delightful with their emotional supports.

Finally, I would like to give special thanks to my mother and a role model in my life, Chunlae Lee, for her endless love, support, and encouragement.

CONTRIBUTORS AND FUNDING SOURCES

Contributors

This work was supervised by a dissertation committee consisting of Professor Karen L. Wooley (advisor, chair of the committee) of the Department of Chemistry, Chemical Engineering, and Materials Science and Engineering, Professor Hung-Jue Sue (committee member) of the Department of Materials Science and Engineering, Professor Lei Fang (committee member) of the Department of Chemistry and Materials Science and Engineering, and Professor Yossef A. Elabd (committee member) and Professor Jodie L. Lutkenhaus (committee member) of the Department of Chemical Engineering and Materials Science and Engineering.

Its contents were completed through the use of the Laboratory for Synthetic Biologic Interactions, the Materials Characterization Facility, and the Microscopy and Imaging Center at Texas A&M University.

In Chapter II, portions of syntheses were done by Dr. Guorong Sun, Dr. Sangho Cho, Dr. Eric E. Leonhardt, Dr. Ashlee A. Janke, and Dr. Yannick Borguet. The different types of materials characterizations were done by Dr. Emile A. Scheweikert, Dr. Stanislav V. Verkhoturov, Dr. Michael J. Eller, Dr. Chun Liu, Dr. Yen-Hao Lin, Dr. Fan Yang, Dr. Yang Zou, Dr. Tianyu Yuan, Dr. Lei Fang, and Dr. Thomas C. Fitzgibbon. The characterizations of fabricated devices' performances were done by Dr. W. Hunter Woodward, Dr. Anatoliy N. Sokolov, and Dr. Guohua Xie. Dr. Peter Trefonas, Dr. Mingqi Li, Dr. Travis McIntire, Dr. Carl Reinhardt, Dr. Liam P. Spencer, and Dr. Chuluo

Yang are acknowledged for the helpful discussions, and Ms. Rui Wang for help with illustrations. In Chapter III, Dr. Guorong Sun is acknowledged for intellectual discussion and Dr. Eric E. Leonhardt for creating the illustrations. Gas sorption isotherms were obtained by Dr. Jiandong Pang. Lastly, Dr. Guorong Sun helped with the design and synthesis of the work in Chapter IV.

All other work conducted for the dissertation was completed by the student independently.

Funding Sources

The Ph.D. research was supported by Dow Chemical Company and DuPont through the continued annual collaborative research agreements for 4 years. This work was also made possible in part by the grants from the National Science Foundation (DMR-1507429 and DMR-1905818), and the Welch Foundation (W. T. Doherty-Welch Chair, A-0001). The resources at the Advanced Photon Source, a U.S. Department of Energy (DOE) Office of Science User Facility by Argonne National Laboratory were used for portions of the work in Chapter II, under Contract No. DE-AC02-06CH11357.

The contents herein do not necessarily represent the official views of the National Science Foundation, the Welch Foundation, Dow Chemical Company, DuPont, or the Department of Energy (DOE), and they are solely the responsibility of the authors.

NOMENCLATURE

| | |
|---------|---|
| AFM | Atomic force microscopy |
| AIBN | 2,2'-Azobis(2-methylpropionitrile) |
| APCI-MS | Atmospheric pressure chemical ionization mass spectrometry |
| ATR | Attenuated total reflection |
| ATRP | Atom transfer radical polymerization |
| BBP | Bottlebrush polymer |
| BET | Brunauer-Emmett-Teller |
| BIBB | α -Bromoisobutyryl bromide |
| CAR | Chemically amplified resist |
| CE | Current (density) efficiency |
| CM | Control membrane |
| CRP | Controlled radical polymerization |
| CTA | Chain-transfer agent |
| CzDBA | 9,10-Bis(4-(9 <i>H</i> -carbazol-9-yl)-2,6-dimethyl phenyl)-9,10-diboraanthracene |
| d-BBP | Dual-chain bottlebrush polymer |
| d-MM | Dual-chain macromonomer |
| d-S | Dual-chain (atom transfer radical polymerization) initiator |
| db-BBP | Double-chain bottlebrush polymer |
| db-MM | Double-chain macromonomer |

| | |
|-----------------------|---|
| db-S | Double-chain (atom transfer radical polymerization) initiator |
| DCM | Dichloromethane |
| DFT | Density functional theory |
| DMSO | Dimethylsulfoxide |
| <i>DP</i> | Degree of polymerization |
| <i>DP_n</i> | Number-average degree of polymerization |
| DSC | Differential scanning calorimetry |
| E-BBP | Extractable bottlebrush polymer |
| ECPMA | 1-Ethylcyclopentyl methacrylate |
| E-MM | Extractable macromonomer |
| EBL | Electron-beam lithography |
| EBL-TF | Post-electron-beam lithography thin film |
| EL | Electroluminescence |
| EQE | External quantum efficiency |
| ETL | Electron transport layer |
| FT | Film thickness |
| FTIR | Fourier-transform infrared spectroscopy |
| G3 | Grubbs' third-generation catalyst |
| GISAXS | Grazing-incidence small-angle X-ray scattering |
| GIWAXS | Grazing-incidence wide-angle X-ray scattering |
| HDPE | High-density polyethylene |
| HIL | Hole injection layer |

| | |
|-------|---|
| HMMM | <i>N,N,N',N',N'',N'''</i> -Hexakis(methoxymethyl)-1,3,5-triazine-2,4,6-triamine |
| HOD | Hole-only device |
| HOMO | Highest occupied molecular orbital |
| HOPG | Highly oriented pyrolytic graphite |
| HPLC | High-Performance Liquid Chromatography |
| HT | Hole transporting |
| HTB | Hole transporting bottlebrush |
| HTL | Hole transport layer |
| ITO | Indium tin oxide |
| LC | Linear control |
| LDPE | Low-density polyethylene |
| Liq | 8-Hydroxyquinolatolithium |
| LS | Light scattering |
| LUMO | Lowest unoccupied molecular orbital |
| M_n | Number-average molecular mass |
| MP | Matrix polymer |
| NB | Norbornene |
| NFHBS | 3,3,4,4,5,5,6,6,6-Nonafluorohexyl- <i>para</i> -benzyloxy styrene |
| NIR | Near-infrared |
| NMR | Nuclear magnetic resonance |
| NP | Nanoparticle |

| | |
|--------------|--|
| NR | Nanorod |
| OFT | Organic film transistor |
| OLED | Organic light-emitting diode |
| OPV | Organic photovoltaic |
| PAA | Poly(acrylic acid) |
| PE | Power efficiency |
| PEDOT:PSS | Poly(3,4-ethylene dioxythiophene):polystyrene sulfonate |
| PhMI | <i>N</i> -Phenylmaleimide |
| <i>p</i> HS | <i>para</i> -Hydroxystyrene |
| PNB | Polynorbornene |
| PNFHBS | Poly(3,3,4,4,5,5,6,6,6-nonafluorohexyl- <i>para</i> -benzyloxy styrene |
| PS | Polystyrene |
| PSA | Pressure swing adsorption |
| <i>Pt</i> BA | Poly(<i>tert</i> -butyl acrylate) |
| PVTPA | Poly(4-vinyl triphenylamine) |
| RAFT | Reversible addition-fragmentation chain-transfer |
| RBF | Round bottom flask |
| ROMP | Ring-opening metathesis polymerization |
| SCK | Shell-crosslinked knedel-like nanoparticle |
| SEC | Size exclusion chromatography |
| SEC-MALS | Size exclusion chromatography multi-angle light scattering |
| SEM | Scanning electron microscopy |

| | |
|-----------|---|
| SIMS | Secondary-ion mass spectrometry |
| TAA | Triarylamine |
| TADF | Thermally activated delayed fluorescence |
| TBAF | Tetrabutylammonium fluoride |
| TFB | Poly(9,9-dioctylfluorene- <i>alt</i> -N-(4-sec-butyl phenyl)-diphenylamine) |
| T_g | Glass transition temperature |
| TGA | Thermogravimetric analysis |
| THF | Tetrahydrofuran |
| TMAH | Tetramethylammonium hydroxide |
| TmPyPB | 1,3,5-Tri(3-pyridyl)-phen-3-ylbenzene |
| TOF-MS | Time-of-flight mass spectrometry |
| TSA | Temperature swing adsorption |
| ttc-Brush | Bottlebrush polymer with trithiocarbonate chain-ends |
| TPA | Triphenylamine |
| TPS-DFEMA | Triphenylsulfonium 1,1-difluoro-2-(methacryloxy)ethanesulfonate |
| UV | Ultraviolet |
| UV-PM | Ultraviolet lithographic polymer membrane |
| UV-vis | Ultraviolet-visible spectrophotometry |
| VASE | Variable angle spectral ellipsometry |
| VTPA | 4-Vinyl triphenylamine |

TABLE OF CONTENTS

| | Page |
|--|------|
| ABSTRACT | ii |
| DEDICATION | iv |
| ACKNOWLEDGEMENTS | v |
| CONTRIBUTORS AND FUNDING SOURCES..... | vi |
| NOMNCLATURE | viii |
| TABLE OF CONTENTS | xiii |
| LIST OF FIGURES..... | xv |
| LIST OF SCHEMES | xxi |
| LIST OF TABLES | xxii |
| CHAPTER I INTRODUCTION | 1 |
| 1.1 Hierarchical Polymer Architectures in Advanced Technology Applications | 1 |
| 1.2 Bottlebrush Polymers from Living Radical Polymerizations..... | 3 |
| 1.3 Scope of the Dissertation..... | 5 |
| CHAPTER II TOPOLOGICAL DESIGN OF A HOLE TRANSPORTING MOLECULAR BOTTLEBRUSH SYSTEM FOR HIGHLY ANISOTROPIC ALIGNMENT IN SOLUTION-PROCESSED THIN FILMS | 8 |
| 2.1 Introduction | 8 |
| 2.2 Results and Discussion | 10 |
| 2.3 Conclusion..... | 53 |
| 2.4 Experimental Section..... | 54 |
| 2.4.1 Materials..... | 54 |
| 2.4.2 Instrumentation and Characterization..... | 54 |
| 2.4.3 Synthesis and Film Preparation | 61 |
| CHAPTER III PHOTOTRIGGERED PORE GENERATION IN POLYMER FILM WITH THE CONTROL OF POROSITY | 75 |

| | | |
|---|--|-----|
| 3.1 | Introduction | 75 |
| 3.2 | Results and Discussion | 78 |
| 3.3 | Conclusion | 92 |
| 3.4 | Experimental Section..... | 92 |
| 3.4.1 | Materials | 92 |
| 3.4.2 | Instrumentation and Characterization..... | 93 |
| 3.4.3 | Details of Syntheses and Film Preparations | 95 |
| | | |
| CHAPTER IV SYNTHESIS OF AMPHIPHILIC MOLECULAR BOTTLEBRUSHES WITH HIGHER GRAFTING DENSITY OF SIDE-CHAIN POLYMERS | | 105 |
| 4.1 | Introduction | 105 |
| 4.2 | Results and Discussion | 108 |
| 4.3 | Conclusion | 113 |
| 4.4 | Experimental Section..... | 114 |
| 4.4.1 | Materials | 114 |
| 4.4.2 | Instrumentation and Characterization..... | 114 |
| 4.4.3 | Synthesis and Sample Preparations | 116 |
| | | |
| CHAPTER V CONCLUSIONS | | 137 |
| | | |
| REFERENCE | | 140 |

LIST OF FIGURES

| | Page |
|---|------|
| Figure 1.1. Schematics of HDPE (left) and LDPE (right) branching structures..... | 2 |
| Figure 1.2. Illustration of a bottlebrush molecular architecture. Bottlebrush polymer consisting of side chains (blue) emerging out from the backbone polymer (red) with an end-to-end distance of R | 3 |
| Figure 2.1. Schematic diagram of the overall design..... | 10 |
| Figure 2.2. THF-SEC profiles of (a) M6, M3, ttc-Brush I, and Brush I, (b) M6, M4, ttc-Brush II, and Brush II, (c) M6, M5, ttc-Brush III, and Brush III, (d) M7, M5, ttc-Brush IV, and Brush IV, (e) M7, M5, ttc-Brush V, and Brush V, respectively..... | 16. |
| Figure 2.3. ^1H NMR (500 MHz, CD_2Cl_2) spectra of (a) ttc-Brush I (olive), and Brush I (black), (b) ttc-Brush II (olive), and Brush II (black), (c) ttc-Brush III (olive), and Brush III (black), (d) ttc-Brush IV (olive), and Brush IV (black), (e) ttc-Brush V (olive), and Brush V (black), respectively..... | 17 |
| Figure 2.4. (a) SEC profiles of Brush II, using CHCl_3 as eluent. The royal lines indicated the “cut-off points” during CHCl_3 -SEC purification. (b) SEC profiles of Brush II before (dotted) and after (solid) CHCl_3 -SEC purification, using THF as eluent. The magenta line indicated the aligned solvent peaks. | 18 |
| Figure 2.5. Photophysical properties of polymers bearing pendant TPA functionalities. (a) Representative UV–vis spectra of HTBs and PVTPAs in THF (red, Brush V; blue, Brush I; black, M4). (b) Fluorescence emission spectra excitation at 660 nm of Brush V (red), Brush I (blue), and M4 (black) in THF, respectively. (c) Solvent polarity-responsive fluorescence emission spectra of Brush I (blue) and V (red). (d) Fluorescence emission spectra excitation at varied wavelengths of Brush V in THF. The insertion was the fluorescence emission profiles in the NIR range. Sample concentrations: 0.1 mg/mL..... | 21 |
| Figure 2.6. (a) Emission spectra of ttc-Brush V excitation at 660 nm in THF (solid), CH_2Cl_2 (dot), and CHCl_3 (dash). Sample concentration: 0.1 mg/mL. (b) UV–vis spectrum between 200 and 455 nm of Brush V in THF with indications of excitation wavelengths..... | 22 |
| Figure 2.7. Summary of Brushes I-V (D_0 : contour length of polynorbornene backbone). The fluorine content was calculated from ttc-Brushes I-V..... | 23 |
| Figure 2.8. Tapping-mode AFM height (left) and phase (right) images of as-cast thin films of (a) Brush I (FT = 20 ± 1 nm), (b) Brush II (FT = 49 ± 1 nm), (c) Brush | |

| | |
|--|----|
| III (FT = 23 ± 1 nm), (d) Brush IV (FT = 29 ± 1 nm), (e) Brush V (FT = 20 ± 1 nm). The images were obtained with a 5×5 μm area. Scale-bars: 1 μm | 26 |
| Figure 2.9. Tapping-mode AFM height (left) and phase (right) images of thermally-annealed thin films of (a) Brush I (FT = 20 ± 1 nm), (b) Brush II (FT = 49 ± 1 nm), (c) Brush III (FT = 22 ± 1 nm), (d) Brush IV (FT = 26 ± 1 nm), (e) Brush V (FT = 19 ± 1 nm). The images were obtained with a 5×5 μm area. Scale-bars: 1 μm | 27 |
| Figure 2.10. Au ₄₀₀ ⁴⁺ SIMS spectra of thin films of Brush III (negative mode; (a) as-cast, (b) thermally-annealed) and Brush IV (positive mode; (c) as-cast, (d) thermally-annealed). | 28 |
| Figure 2.11. Tapping-mode AFM height (top row) and phase (bottom row) images of as-cast (left column, FT = 55 ± 2 nm) and thermally-annealed (right column, FT = 54 ± 2 nm) thin films of CHCl ₃ -SEC purified Brush II. The images were obtained with a 5×5 μm area. Scale-bar: 1 μm | 29 |
| Figure 2.12. SIMS fluorine depth profiles (left, as-cast; right, thermally-annealed) of (a) Brush I, (b) Brush III, (c) Brush V, (d) Brush II, and (e) Brush IV films on Si wafers, respectively. | 30 |
| Figure 2.13. Representative thermal characterizations of HTBs and related macromonomer precursors. (a) DSC traces of Brush V (left) and ttc-Brush V (right), respectively. (b) DSC traces of NB-PVTPA ₃₉ (M5, left) and NB-PVTPA ₂₂ - <i>b</i> -PNFHBS ₉ (M7, right), respectively. DSC traces were obtained under N ₂ atmosphere with a heating and cooling rate of 10 °C/min. The glass transition temperatures (<i>T</i> _{gs}) were labeled on the thermograms. (c) TGA traces of M5, M7, ttc-Brush V, and Brush V. TGA traces were obtained under Ar atmosphere with a heating rate of 5 °C/min. | 31 |
| Figure 2.14. Optical constants (<i>n</i> : refractive index; <i>k</i> : extinction coefficient; subscripts o and e refer to the ordinary and extraordinary directions, respectively) vs. wavelength profiles at (0, 0) coordinates of as-cast (left column) and thermally-annealed (right column) (a) Brush I, (b) Brush III, (c) Brush V, (d) Brush II, and (e) Brush IV films on neat Si wafers, respectively. | 33 |
| Figure 2.15. Tapping-mode AFM height (top) and phase (bottom) images of thermally-annealed (a) Brush III thin films on PEDOT:PSS coated Si wafer (HTL FT = 25 ± 1 nm), (b) Brush III thin films on PEDOT:PSS coated ITO glass (HTL FT = 24 ± 1 nm), (c) Brush I thin films on PEDOT:PSS coated ITO glass (HTL FT = 24 ± 1 nm), and (d) Brush V thin films on PEDOT:PSS coated ITO glass (HTL FT = 25 ± 2 nm), respectively. The images were obtained with a 5×5 μm area. Scale-bars: 1 μm | 36 |

| | |
|---|----|
| Figure 2.16. GISAXS (top row) and GIWAXS (bottom row) characterizations of thermally-annealed Brush III thin films on neat (a and c) and PEDOT:PSS-coated (b and d) Si wafers, respectively. q_{xy} and q_z were defined as coordinates of the reciprocal space. | 37 |
| Figure 2.17. (a) GISAXS characterizations of thermally-annealed Brush III thin films on neat (top) and PEDOT:PSS-coated (bottom) Si wafers, respectively. The plots (right column) show the in-plane line cuts (red rectangle) through the full patterns (left column). The corresponding FTs at $q_z = 0.03$ and 0.032 \AA^{-1} (indicated by blue arrows) were 21 and 20 nm, respectively. (b) GIWAXS 1D diffraction curves along with the q_z directions for thermally-annealed Brush III thin films on neat and PEDOT:PSS coated Si wafer, respectively. q_{xy} and q_z were defined as coordinates of the reciprocal space. | 38 |
| Figure 2.18. Cyclic voltammetry profiles of Brush III in CH_2Cl_2 | 39 |
| Figure 2.19. Molecular fragment structures for DFT calculations of HOMO and LUMO levels to define a selection of the bottlebrush composition and structural design. | 40 |
| Figure 2.20. Performance evaluations of HODs comprising Brush III (HOD-III) and LC (HOD-LC), respectively. (a) Current density vs. voltage plots. (b) Hole mobility vs. square root of electric field plots. | 41 |
| Figure 2.21. (a) Molecular structures of additional components used in the OLED devices. Liq: 8-hydroxyquinolinolato-lithium, CzDBA: 9,10-bis(4-(9H-carbazol-9-yl)-2,6-dimethylphenyl)-9,10-diboraanthracene, TmPyPB: 1,3,5-tri(<i>m</i> -pyridin-3-ylphenyl)benzene, TFB: poly(9,9-dioctylfluorene- <i>alt</i> - <i>N</i> -(4-sec-butylphenyl)-diphenylamine). (b) Device configuration and (c) Energy level diagram (The LUMO value, ca. -1.7 eV, of Brush III was estimated from the UV-vis spectrum and the cyclic voltammetry characterizations)..... | 43 |
| Figure 2.22. EL characterizations of TFB device. (a) Current density vs. voltage plots, (b) luminance vs. voltage plots, (c) current density efficiency, (d) power efficiency, (e) external quantum efficiency plots. Multilayered OLED device structure: ITO/PEDOT:PSS (40 nm)/TFB (25 nm)/CzDBA (40 nm)/TmPyPB (45 nm)/Liq (1nm)/Al (100 nm). | 44 |
| Figure 2.23. EL characterizations of LC device. (a) Current density vs. voltage plots, (b) luminance vs. voltage plots, (c) current density efficiency, (d) power efficiency, (e) external quantum efficiency plots. Multilayered OLED device structure: ITO/PEDOT:PSS (40 nm)/LC (25 nm)/CzDBA (40 nm)/TmPyPB (45 nm)/Liq (1nm)/Al (100 nm). | 45 |

| | |
|--|----|
| Figure 2.24. EL characterizations of Brush I device. (a) Current density vs. voltage plots, (b) luminance vs. voltage plots, (c) current density efficiency, (d) power efficiency, (e) external quantum efficiency plots. Multilayered OLED device structure: ITO/PEDOT:PSS (40 nm)/Brush I (25 nm)/CzDBA (40 nm)/TmPyPB (45 nm)/Liq (1nm)/Al (100 nm). | 46 |
| Figure 2.25. EL characterizations of Brush III device. (a) Current density vs. voltage plots, (b) luminance vs. voltage plots, (c) current density efficiency, (d) power efficiency, (e) external quantum efficiency plots. Multilayered OLED device structure: ITO/PEDOT:PSS (40 nm)/Brush III (25 nm)/CzDBA (40 nm)/TmPyPB (45 nm)/Liq (1nm)/Al (100 nm). | 47 |
| Figure 2.26. EL characterizations of Brush V device. (a) Current density vs. voltage plots, (b) luminance vs. voltage plots, (c) current density efficiency, (d) power efficiency, (e) external quantum efficiency plots. Multilayered OLED device structure: ITO/PEDOT:PSS (40 nm)/Brush V (25 nm)/CzDBA (40 nm)/TmPyPB (45 nm)/Liq (1nm)/Al (100 nm). | 48 |
| Figure 2.27. Performance evaluations of green OLED full devices comprising Brush I, III, and V, and LC and TFB, respectively, as HTLs. (a) Normalized electroluminescence spectra of devices. (b–c) Current density (b) and luminance (c) vs. voltage plots, respectively. (d–f) External quantum efficiency (d), power efficiency (e), and current efficiency (f) vs. current density plots, respectively | 52 |
| Figure 2.28. NMR spectra for NB-CTA. (a) ^1H NMR (400 MHz, CDCl_3) and (b) ^{13}C NMR (101 MHz, CDCl_3). | 65 |
| Figure 2.29. ^1H NMR spectra of (a) M5 (500 MHz, CD_2Cl_2), (b) M6 (500 MHz, CD_2Cl_2) and (c) M7 (500 MHz, CDCl_3). | 69 |
| Figure 3.1. Illustrative diagram of the porous membrane preparation. Positive-tone photoresist moiety of BBPs (dark blue) is deprotected (red) upon exposure to light and extracted after the lithographic development process, while negative-tone matrix polymers (light blue) are crosslinked..... | 77 |
| Figure 3.2. ^1H NMR (400 MHz, CDCl_3) spectra of E-MM1. | 81 |
| Figure 3.3. (a) ^1H NMR (400 MHz, CDCl_3) of E-BBP1. (b) SEC traces of E-MM1 (black) and E-BBP1 (red). | 82 |
| Figure 3.4. Tapping-mode AFM height (left) and phase (right) images. (a) as-cast polymer thin film, (b-c) EBL-TFs generated at exposure dosages of (b) 200 and (c) $400 \mu\text{C}/\text{cm}^2$. Scale bars: 200 nm. | 85 |

| | |
|---|-----|
| Figure 3.5. Tapping-mode AFM height images of EBL-TFs generated triangle patterns at exposure dosages of (a) 100 $\mu\text{C}/\text{cm}^2$ (upper, FT = 8 ± 2 nm) and 200 $\mu\text{C}/\text{cm}^2$ (lower, FT = 15 ± 2 nm), and (c) 400 $\mu\text{C}/\text{cm}^2$ (FT = 15 ± 2 nm). Scale bars: 10 μm | 86 |
| Figure 3.6. SEM images of (a-d) UV-PM-a, (c-d) UV-PM-b, and (e-f) CM. Membranes of (a-b) and (e) had no protective coatings, while membranes of (c-d) and (f) were coated with 3nm Pt/Pd coatings prior to SEM imaging. Scale bars: 10000 nm (a-b, black), 1000 nm (b-c, white), 100 nm (c-f, red). | 87 |
| Figure 3.7. (a) N_2 sorption isotherms of UV-PM-b (red) and CM (olive) at 77K. The filled symbols represent adsorption and the empty symbols represent desorption data. (b) CO_2 adsorptions of UV-PM-b at 273K (blue) and 298K (red) and of CM at 298K (olive). | 89 |
| Figure 3.8. ^1H NMR spectra of (a) E-MM2 (500 MHz, CDCl_3) and (b) E-MM3 (500 MHz, CD_2Cl_2)..... | 97 |
| Figure 3.9. TGA traces of (a) E-MM2, and (b) E-MM3. TGA traces were obtained under Ar atmosphere with a heating rate of 5 $^\circ\text{C}/\text{min}$ | 98 |
| Figure 3.10. ^1H NMR spectra of (a) E-BBP2 (500 MHz, CDCl_3) and (b) E-BBP3 (500 MHz, CD_2Cl_2)..... | 101 |
| Figure 3.11. TGA trace of E-BBP1. TGA traces were obtained under Ar atmosphere with a heating rate of 5 $^\circ\text{C}/\text{min}$ | 102 |
| Figure 3.12. ^1H NMR (400 MHz, $\text{DMSO}-d_6$) of MP..... | 103 |
| Figure 4.1. (a) Illustration of an amphiphilic PAA- <i>b</i> -PS bottlebrush polymer before the growth of inorganic nanorod (left) and after the completion of nanorod formation (right). (b) Chemical compositions of the overall design to increase the grafting density or side-chain density of BBP. | 107 |
| Figure 4.2. SEC traces of d-MM2 (black) and d-BBP1 (red). | 111 |
| Figure 4.3. Multi-mode AFM height images (500×500 nm area) of individual db-BBP2s on a HOPG substrate. The inserted red box is a zoomed-in image of an individual bottlebrush. Scale bars: 50 nm (red), 100 nm (white)..... | 112 |
| Figure 4.4. (a) Histogram of the size distribution of db-BBP2 by AFM characterization. The average of db-BBP2 size was calculated by counting 100 individual particles from AFM height images. (b) Schematic depicts of bottlebrush polymers on the HOPG substrates. An illustration of BBP on the left is showing the possible morphology with extending side-chains parallel to backbone polymer..... | 113 |

| | |
|---|-----|
| Figure 4.5. ^1H NMR (500 MHz) spectra of (a) d-S2 (CD_2Cl_2), (b) d-S3 (CDCl_3), and (c) d-S4 (CD_2Cl_2). | 120 |
| Figure 4.6. ^1H NMR (500 MHz) spectra of (a) d-MM1 (CDCl_3), and (b) d-MM2 (CD_2Cl_2). | 123 |
| Figure 4.7. ^1H NMR (500 MHz) spectra of (a) db-S3 (CD_2Cl_2), and (b) db-S4 (CDCl_3). | 127 |
| Figure 4.8. ^1H NMR (500 MHz, CDCl_3) spectra of (a) db-S5, (b) d-S6, and (c) d-S7. | 131 |
| Figure 4.9. ^1H NMR (500 MHz) spectra of (a) db-MM1 (CDCl_3), and (b) db-MM2 (CD_2Cl_2). | 134 |
| Figure 4.10. ^1H NMR (500 MHz) spectra of (a) db-BBP1 (CD_2Cl_2), and (b) db-BBP2 ($\text{DMSO}-d_6$). | 136 |

LIST OF SCHEMES

| | Page |
|---|------|
| Scheme 2.1. Synthesis of NB-CTA..... | 12 |
| Scheme 2.2. Syntheses of macromonomers (a) and HT bottlebrushes (b). | 12 |
| Scheme 3.1. Syntheses of macromonomers, E-MMs (a) and extractable bottlebrush polymers, E-BBPs (b). | 79 |
| Scheme 3.2. Synthesis of matrix polymer (MP). | 84 |
| Scheme 4.1. Synthesis of d-BBP through ATRP and ROMP..... | 109 |
| Scheme 4.2. Synthesis of db-BBP through ATRP and ROMP..... | 110 |
| Scheme 4.3. Synthesis of dual ATRP initiator (d-S4)..... | 116 |
| Scheme 4.4. Synthesis of double ATRP initiator (db-S7)..... | 125 |

LIST OF TABLES

| | Page |
|---|------|
| Table 2.1. RAFT polymerization of VTPA..... | 13 |
| Table 2.2. RAFT chain extension of NFHBS. | 13 |
| Table 2.3. Sequential ROMP of NB-PVTPA- <i>b</i> -PNFHBS (ROMP I) and NB-PVTPA (ROMP II)..... | 14 |
| Table 2.4. Molecular mass (using LS detection, based on injected mass) of HT brushes before/after RAFT chain-ends removal. | 15 |
| Table 2.5. Number of triphenylamine hole transporting functionalities in the single molecule of LC and Brush I-V..... | 25 |
| Table 2.6. Brush coverage of Brush III and Brush IV calculated from Au ₄₀₀ ⁴⁺ SIMS surface analysis data..... | 28 |
| Table 2.7. Summary of green TADF-OLED characteristics..... | 52 |
| Table 3.1. RAFT copolymerizations of ECPMA and TPS-DFEMA..... | 79 |
| Table 3.2. The comparison of porous materials for the CO ₂ uptakes from the literature. | 91 |
| Table 3.3. ROMP of NB-P(ECPMA- <i>co</i> -(TPS-DFEMA))..... | 100 |

CHAPTER I

INTRODUCTION

1.1 Hierarchical Polymer Architectures in Advanced Technology Applications

Molecular architectures of polymers wield strong influence over their material properties, such as elasticity, viscosity, stimuli-responsiveness, degradability, surface energy, molecular assemblies, or electrical and thermal conductivities. Structure-property relationships of polymers are a crucial factor that allows a great number of applications. One everyday example showing the effect of molecular architectures is the branching of polyethylene (Figure 1.1). Two types of polyethylene categorized by the different degrees of branching, low-density polyethylene (LDPE) with a high degree of branching and high-density polyethylene (HDPE) with no or a low degree of branching exhibit very different material properties in terms of crystallinity and tensile strength. As result, LDPE and HDPE have distinct applications they are used for—the common uses of LDPE are in plastic bags, plastic wraps, snap-on lids, and dispensing bottles, whereas HDPE is applied to piping materials, ballistic plates, playground equipment, and snowboards. Molecular architecture has a significant role in applications of polymers, and is an important factor for consideration in material design.

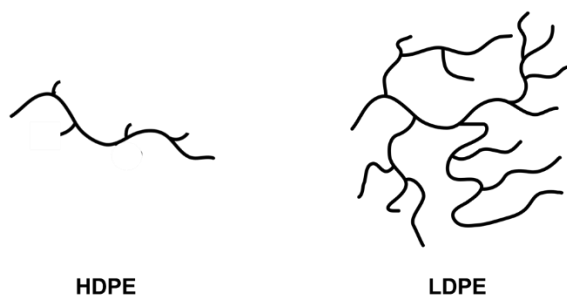


Figure 1.1. Schematics of HDPE (left) and LDPE (right) branching structures.

A variety of polymer architectures can be obtained based on the site position and degree of branching. Theoretically, possible polymer architectures in three-dimensions are infinite, as there are infinite ways to connect polymer chains. However, the scope of possible molecular architectures is confined by many challenges in polymer syntheses in reality. Accordingly, fundamental studies and potential applications of functional polymers are restricted by these limitations. Despite these difficulties, many chemists have devised a myriad of diverse polymer architectures, such as star polymers,¹ ladder polymers,² dendronized polymers,³ polymer brushes,⁴⁻⁵ dendrimers,⁶ cyclized polymers,⁷⁻⁸ and shell-crosslinked knedel-like nanoparticles (SCKs).⁹ By utilizing these complex polymer architectures, new and/or different advanced technology applications, such as drug delivery,¹⁰⁻¹¹ bioimaging,¹² polymer sensors,¹³⁻¹⁴ energy storage,¹⁵ organic film transistors (OFTs),¹⁶ organic light-emitting diodes (OLEDs),¹⁷ organic photovoltaics (OPVs),¹⁸ and photoresists for lithography¹⁹⁻²¹ are achievable.

By applying appropriate architecture designs to functionalized polymers, they can achieve the optimized conditions to exhibit their functionalities, which allows for specific performance enhancement in the final applications. In this regime, the exploration of

relationships between the complexity of polymer architectures and their material properties has become one significant area in polymer chemistry and engineering. With the remarkable improvements in controlled polymerization techniques, now it is possible to synthesize polymers with precise molecular designs. This dissertation puts an emphasis on polymers with bottlebrush structures and will present the new designs, syntheses, and characterizations of bottlebrush polymer systems. Finally, the demonstration of the impact of molecular architectures on device performances in respective applications will be addressed.

1.2 Bottlebrush Polymers from Living Radical Polymerizations

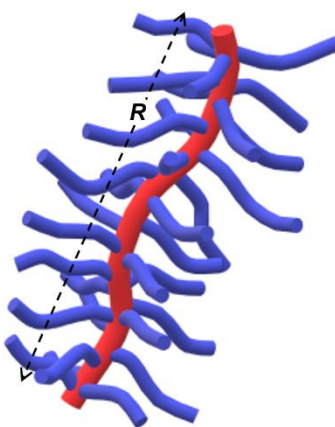


Figure 1.2. Illustration of a bottlebrush molecular architecture. Bottlebrush polymer consisting of side chains (blue) emerging out from the backbone polymer (red) with an end-to-end distance of R .

A bottlebrush polymer (BBP), or molecular bottlebrush, is a macromolecule with a cylindrical bottlebrush structure where the main backbone polymer is densely-grafted with polymeric side-chains, as shown in Figure 1.2. BBPs tend to retain stretched

conformations with lower entanglements, due to the steric hindrance between graft chains emerging out from the backbone polymer.²²⁻²³ Owing to their unique geometry and shape-persistence, BBPs have stood out as an efficacious tool in bottom-up nanomaterial fabrication. More precise control in chemical composition and dimension with a variation of the relative concentric and backbone lengths are accomplished by employing macromonomer frameworks whose compositions are pre-set. This approach of BBP preparation, which involves macromonomer frameworks or building blocks, is a so-called 'grafting-through' method, also known as a macromonomer method. There are three different strategies to prepare BBPs; grafting-from, grafting-to, and grafting-through approaches. Above all, the grafting through approach is one of the simpler ways of preparing a BBP with well-defined graft polymers.

Various polymerization techniques—atom transfer radical polymerization (ATRP), reversible addition-fragmentation chain transfer (RAFT) polymerization, ring-opening metathesis polymerization (ROMP), anionic and cationic polymerizations, and radiation-induced polymerization—can be employed to construct BBPs. Amongst these, controlled radical polymerizations (CRP) or living free radical polymerizations, such as nitroxide-mediated radical polymerization (NMP), ATRP and RAFT polymerization, are most often used for the synthesis of macromonomer frameworks²⁴⁻²⁶ because of their capability to tailor chemical compositions and functionalities with a high degree of control. CRP has significant advantages over ionic and/or coordination polymerizations which are; less demanding reaction conditions, tolerance of trace impurities, variety of monomers, good control over molar mass and its dispersity, and end functionalities.²⁷ A widely-used and

well-known synthetic technique to graft-through pre-synthesized macromonomers to construct a bottlebrush molecular architecture is a living ROMP.²⁸⁻³² With the proper reaction conditions, ROMP can be rendered living and a living ROMP allows the control of molecular mass with a low polydispersity.³³⁻³⁴

1.3 Scope of the Dissertation

In Chapter II, a bottlebrush topological factor has been designed as a fundamental chemistry tactic to address the longstanding challenge of highly anisotropic packing of hole transport moieties into preferential “face-on” orientations for advanced hole transport layer technologies. Applying state-of-the-art polymer synthetic techniques, heterogeneous functional sub-units, including triphenylamine for charge transport and adhesion to the substrate, and perfluoro alkyl-substituted benzyloxy styrene for migration to the air interface, are organized with exquisite control over the composition and placement throughout the macromolecular frameworks. Hole transport films, consisting of synthesized hole transporting bottlebrush (HTB) polymers, are fabricated on various substrates through spin-casting and thermal annealing. Next, the alignments of the backbones and hole transporting units of the HTB polymers upon assembling into monolayered polymer films are confirmed by secondary-ion mass spectrometry (SIMS), variable angle spectroscopic ellipsometry (VASE), and grazing incidence x-ray scattering characterizations. The performances of multilayered OLEDs comprised of hole transport

layers (HTLs) of HTB polymers demonstrate the beneficial impacts of this topological design in an optoelectronics application.

In Chapter III, a new approach to fabricate porous films or membranes with controllable porosities, by applying molecular bottlebrushes as sacrificial templates extracted from the crosslinked polymer matrix to generate pores, is presented. The concept of contrary development processes of positive- and negative-tone photoresists¹⁹⁻²¹ was exploited to selectively remove the extractable domain while maintaining the matrix domain. The membranes can be prepared simply by molding a mixture of photosensitive positive-tone chemically-amplified resist (CAR) functionalized BBPs which also include covalently-bonded photoacid generator moieties, crosslinkable negative-tone CAR polymers, and crosslinkers. Upon ultraviolet (UV) light exposure of the cast mixture, the generated photoacids modulate the solubilities of the positive-tone BBP CAR and negative-tone CAR matrix polymers. Resultingly, the deprotected positive-tone BBPs become soluble in an aqueous base developer solution, then the pores are generated by removing BBPs from the membrane. The selective gas adsorption for carbon dioxide (CO₂) gas, observed from Brunauer-Emmett-Teller (BET) measurement of the porous membranes fabricated by this strategy, rationalizes their utility in advanced applications of CO₂ separation.

The last project in Chapter IV introduces the strategy of retaining the extended shape of bottlebrush polymers throughout introducing more densely grafted side-chain polymers on the norbornene backbone of a BBP. Completion of the designed double-chain BBP synthesis has been confirmed and evaluated. The morphologies of the more

densely grafted BBPs observed by AFM show that flexibility or entanglement of BBP has decreased in line with the increase of grafting density of molecular bottlebrushes. The observed outcomes support the potential of more-densely grafted BBPs as templating agents for the anisotropic growth of nanoparticles in the application of inorganic nanorods synthesis.

CHAPTER II

TOPOLOGICAL DESIGN OF A HOLE TRANSPORTING MOLECULAR
BOTTLEBRUSH SYSTEM FOR HIGHLY ANISOTROPIC ALIGNMENT IN
SOLUTION-PROCESSED THIN FILMS*

2.1 Introduction

It has been well established that the device performance (*e.g.*, efficiency, lifetime, and turn-on voltage) of a multilayered organic light-emitting diode (OLED) is dependent on the molecular composition and orientation within each layer and at each inter-layer interface of the device, as these characteristics determine the charge mobility within the layers and the charge injection barrier levels between layers.³⁵⁻⁴² A high degree of alignment of planar molecules used as the hole injection layers (HILs), hole transport layers (HTLs), and electron transport layers (ETLs) into an anisotropic “face-on” orientation has been shown to lower the hole injection barrier at the anode/HIL interface, to increase the hole mobility in the HTL⁴³⁻⁴⁸ and electron mobility in the ETL.⁴⁹⁻⁵⁴ Therefore, the molecular orientations relative to the substrate and within and between each layer are important for device performance.

* Adapted with permission from “Topological Design of a Hole Transporting Molecular Bottle-brush System for Highly Anisotropic Alignment in Solution-processed Thin Films” by Kang, N.; Cho, S.; Leonhardt, E. E.; Verkhoturov, S. V.; Liu, C.; Woodward, W. H.; Eller, M. J.; Yuan, T.; Fitzgibbons, T. C.; Borguet, Y.; Jahnke, A. A.; Sokolov, A. N.; McIntire, T.; Reinhardt, C. Fang, L.; Schweikert, E. A.; Spencer, L. P.; Yang, C.; Sun, G.; Trefonas, P.; Wooley, K. L., **2020**, *in preparation*.

Typically, orientation control of planar and quasiplanar π -conjugated small molecules is accomplished by vacuum deposition.⁴³⁻⁵⁴ Although vacuum deposition techniques are capable of excellent orientational ordering, they are limited by the molar masses that can be vaporized and the dimensions over which OLED devices can be fabricated. Solution processing⁵⁵⁻⁵⁸ could overcome these limitations, extending to macromolecular charge-transport materials^{17, 59-62} and large-scale dimensions. Unfortunately, except for the conjugated polymers with long-range coplanarity, solution processing is incapable of achieving the exquisite molecular ordering of evaporative methods, rather leading to a poorer alignment of HT and ET core units, and lower device performance.⁶³ The development of solution-processable polymeric hole transport materials that enable “face-on” packing of HT functionalities are highly desirable for technically-simplified and cost-effective production of large-area OLED displays.

We hypothesized that the introduction of a topological factor, together with bottom-up morphology and spatial orientation controls during the assembly process, would facilitate the preferential anisotropic “face-on” packing of HT functionalities within an HTL film. A molecular bottlebrush architecture,⁶⁴⁻⁶⁶ *i.e.*, a rigid backbone tethered with densely-grafted side chains, was selected because of the potential to generate a pronounced cylinder-like molecular shape. The strong size exclusion effect between side chains/grafts was expected to decrease the flexibility of HT grafts and provide effective confinement that would promote the cofacial packing between inter-graft HT moieties. Thin film assembly through spin-casting and annealing-promoted vertical alignment of the molecular brushes on substrates¹⁹⁻²¹ was defined as a tactic by which to place the HT

units into an anisotropic horizontal orientation relative to the substrate (Figure 2.1). To demonstrate this overall strategy, triarylamines (TAAs) were employed as the HT functionalities, as one important class of small molecules for OLED applications that have been explored extensively, yet found to present challenges by the intrinsic propeller-like structure of the TAA moiety disrupting the anisotropic “face-on” packing of TAAs within amorphous HTL films.

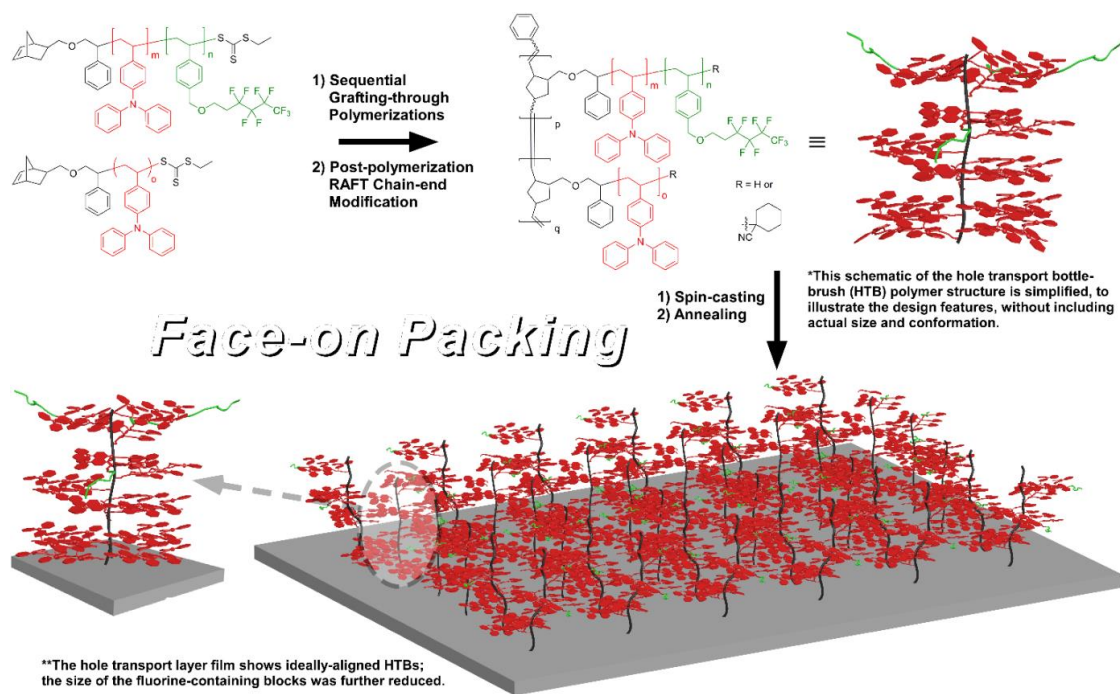


Figure 2.1. Schematic diagram of the overall design.

2.2 Results and Discussion

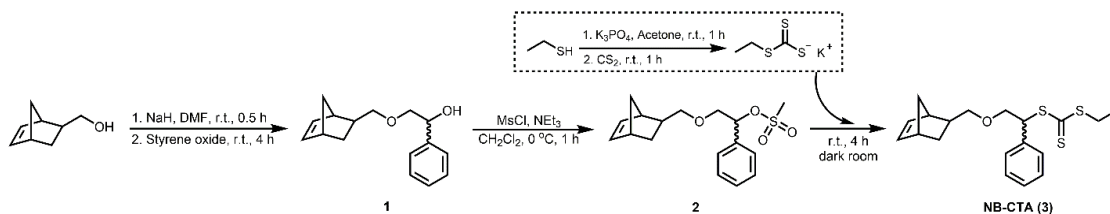
Design and Syntheses of HT Bottlebrush Polymers. The HT bottlebrush (HTB) polymers utilized in this study were composed of two types of grafts, poly(4-vinyl

triphenylamine)-*block*-poly(3,3,4,4,5,5,6,6,6-nonafluorohexyl-*para*-benzyloxy styrene) (PVTPA-*b*-PNFHBS) block copolymer and PVTPA homopolymer, in a block manner along a polynorbornene (PNB) backbone. The pendant TPA groups were designed to function for hole transport and substrate adhesion, while the fluorocarbon moieties in the PNFHBS block segments were incorporated to act as surface energy-reducing functionalities to promote vertical alignment of brushes on the substrate. Different from our previous approaches,¹⁹⁻²¹ the perfluorinated substituents were not directly connected to the TPA moieties. This design principle was applied since density functional theory (DFT) calculations of the highest occupied molecular orbital (HOMO) and the lowest unoccupied molecular orbital (LUMO) energy levels of small molecule analogs, which represent fragments of the HTBs, showed a noticeable decrease with the introduction of F-containing substituted groups on TPAs (Figure 2.19; entries 2–7 *vs.* 1). Sequential “grafting-through” ring-opening metathesis polymerizations (ROMPs)⁶⁴⁻⁶⁶ were utilized for the construction of the HTBs. Upon assembly of the HTBs into HTL films, the PNB backbones of individual brushes were perpendicularly oriented to the substrate, which could ideally provide a collective “face-on” packing of the TPAs within the HTL films.

An *exo*-NB-terminated trithiocarbonate chain transfer agent (NB-CTA), with a stable ether linkage, was synthesized (Scheme 2.1) and used for the preparation of the NB-(PVTPA-*b*-PNFHBS) and NB-PVTPA macromonomers (Scheme 2.2a, **M1-M7**) with predetermined molar masses and the narrow dispersity ($D < 1.1$) through reversible addition-fragmentation chain transfer (RAFT) polymerizations (Tables 2.1 and 2.2).⁶⁷⁻⁶⁹ The well-defined structure of each macromonomer was verified through the combined

data from spectroscopic and chromatographic analyses. Preservation of the characteristic NB and trithiocarbonate CTA functionalities was confirmed by ^1H NMR spectroscopy. Molar mass calculations from ^1H NMR spectroscopy (comparing the peak integrals of NB alkenyl protons and aromatic protons) were consistent with size exclusion chromatography-multiangle light scattering (SEC-MALS) analyses (Tables 2.1 and 2.2).

Scheme 2.1. Synthesis of NB-CTA.



Scheme 2.2. Syntheses of macromonomers (a) and HT bottlebrushes (b).

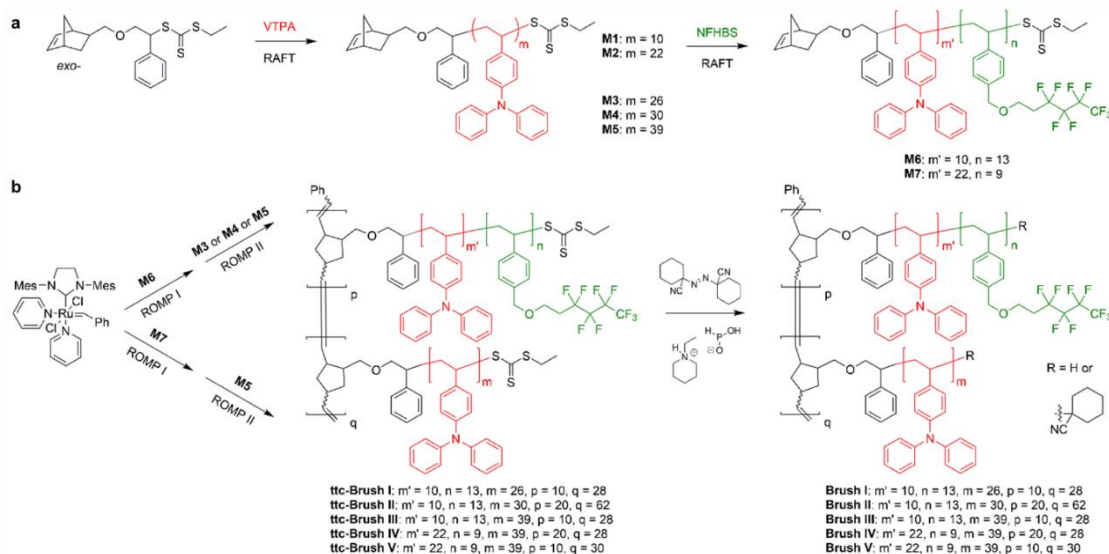


Table 2.1. RAFT polymerization of VTPA.

| | [VTPA] ₀ : [NB-CTA] ₀ : [AIBN] ₀ | T (°C) | time (h) | Conversion ^a | M _{n,NMR} (Da) | M _{n,SEC} ^b (Da) | Đ |
|-----------|---|--------|----------|-------------------------|-------------------------|--------------------------------------|------|
| M1 | 30:1:0.1 | 61 | 21.5 | 33 % | 3070 | 2800 | 1.10 |
| M2 | 35:1:0.1 | 60 | 26 | 63 % | 6330 | 6040 | 1.04 |
| M3 | 50:1:0.1 | 61 | 31 | 52 % | 7410 | 7310 | 1.03 |
| M4 | 60:1:0.1 | 60 | 31 | 50 % | 8760 | 8330 | 1.03 |
| M5 | 60:1:0.1 | 62 | 42.5 | 65 % | 11000 | 10080 | 1.02 |

^aBy ¹H NMR spectroscopy. ^bBy SEC using LS detection (based on injected mass).

Table 2.2. RAFT chain extension of NFHBS.

| | [NFHBS] ₀ : [NB-PVTPA] ₀ : [AIBN] ₀ | T (°C) | t (h) | Conversion ^a | M _{n,NMR} (Da) | M _{n,SEC} ^b (Da) | Đ |
|-----------|--|--------|-------|-------------------------|-------------------------|--------------------------------------|------|
| M6 | 40:1 (M1):0.08 | 60 | 20 | 33 % | 8400 | 8680 | 1.04 |
| M7 | 32:1 (M2):0.08 | 60 | 20 | 28 % | 9320 | 10090 | 1.04 |

^aBy ¹H NMR spectroscopy. ^bBy SEC using LS detection (based on injected mass).

A set of P[NB-*g*-(PVTPA-*b*-PNFHBS)]-*b*-P(NB-*g*-PVTPA) HTBs, with variable dimensions of overall molecular structure (Scheme 2.2b, **ttc-Brush I-V**), was synthesized *via* sequential ROMPs of the corresponding macromonomers, by utilizing Grubbs' G3 catalyst. The progress of each ROMP was monitored by ¹H NMR spectroscopy and SEC (Figure 2.2) analyses of aliquots withdrawn at pre-determined time points (Table 2.3). ¹H NMR spectra (Figure 2.3) showed the disappearance of the NB alkenyl proton resonance at 6.08 ppm. Shifts of SEC peaks to shorter elution times were observed upon growth from macromonomers to bottlebrush polymers. As a note, we noticed the persistence of an SEC signal coinciding with *ca.* 5% of non-reacted macromonomers. This observation, together with a lack of remaining NB alkenyl proton resonance, suggested the presence of polymeric “contaminants” having an absence of terminal NB functionality, inherent to

RAFT polymerizations. The degree of polymerization (DP) of the P[NB-*g*-(PVTTPA-*b*-PNFHBS)] block was calculated based upon the initial feed ratio of [catalyst]:[NB-(PVTTPA-*b*-PNFHBS)] and ~95% conversion during the first ROMP process. The relative DP_n ratios between the P[NB-*g*-(PVTTPA-*b*-PNFHBS)] and P(NB-*g*-PVTTPA) blocks were obtained based on ^1H NMR spectroscopy (Figure 2.29). Finally, the trithiocarbonate functionalities were removed through a radical-induced reduction⁷⁰ to afford **Brush I-V**, confirmed by the disappearance of the ethyl proton resonances ($-\text{SCH}_2\text{CH}_3$ at *ca.* 3.24 and 1.22 ppm, respectively, Figure 2.3). The SEC profiles of the final HTBs revealed slightly-broadened molecular weight distributions, which were attributed to the formation of intrabrush loops between side-chains during the RAFT chain-ends removal process, due to the interchain radical couplings. Semi-preparative CHCl_3 -SEC was then applied to remove the defected brush and unreacted macromonomer “contaminates”, as exemplified by **Brush II** (Figure 2.4a). However, the purified **Brush II** showed a pronounced high molar mass shoulder by THF-SEC (Figure 2.4b).

Table 2.3. Sequential ROMP of NB-PVTTPA-*b*-PNFHBS (ROMP I) and NB-PVTTPA (ROMP II).

| Brush | Macromonomers | [cat.] ₀ : [NB-PVTTPA- <i>b</i> -PNFHBS] ₀ : [NB-PVTTPA] ₀ | t_{ROMPI} (h) | t_{ROMPII} (h) |
|--------------|---------------|--|---------------------------|----------------------------|
| I | M6, M3 | 1: 10: 30 | 1.5 | 5.0 |
| II | M6, M4 | 1: 20: 60 | 1.5 | 4.0 |
| III | M6, M5 | 1: 10: 30 | 1.5 | 5.5 |
| IV | M7, M5 | 1: 20: 30 | 1.0 | 5.0 |
| V | M7, M5 | 1: 10: 30 | 1.0 | 4.0 |

Table 2.4. Molecular mass (using LS detection, based on injected mass) of HT brushes before/after RAFT chain-ends removal.

| Brush | $M_{n,SEC}$ (kDa) | $M_{n,theor.}$ (kDa) | \bar{D} |
|--------------------|-------------------|------------------------------------|-----------|
| ttc-I/I | 33.5/41.3 | 291 ^a /286 ^b | 1.39/1.27 |
| ttc-II/II | 142/151 | 659 ^a /649 ^b | 1.49/1.51 |
| ttc-III/III | 264/371 | 393 ^a /388 ^b | 1.20/1.52 |
| ttc-IV/IV | 167/237 | 491 ^a /484 ^b | 1.32/1.21 |
| ttc-V/V | 299/324 | 402 ^a /397 ^b | 1.06/1.05 |

^aCalculated from the corresponding ROMP I feed ratio and 95% of macromonomer conversion. ^bAssumed all trithiocarbonate RAFT chain ends were reduced to Hs.

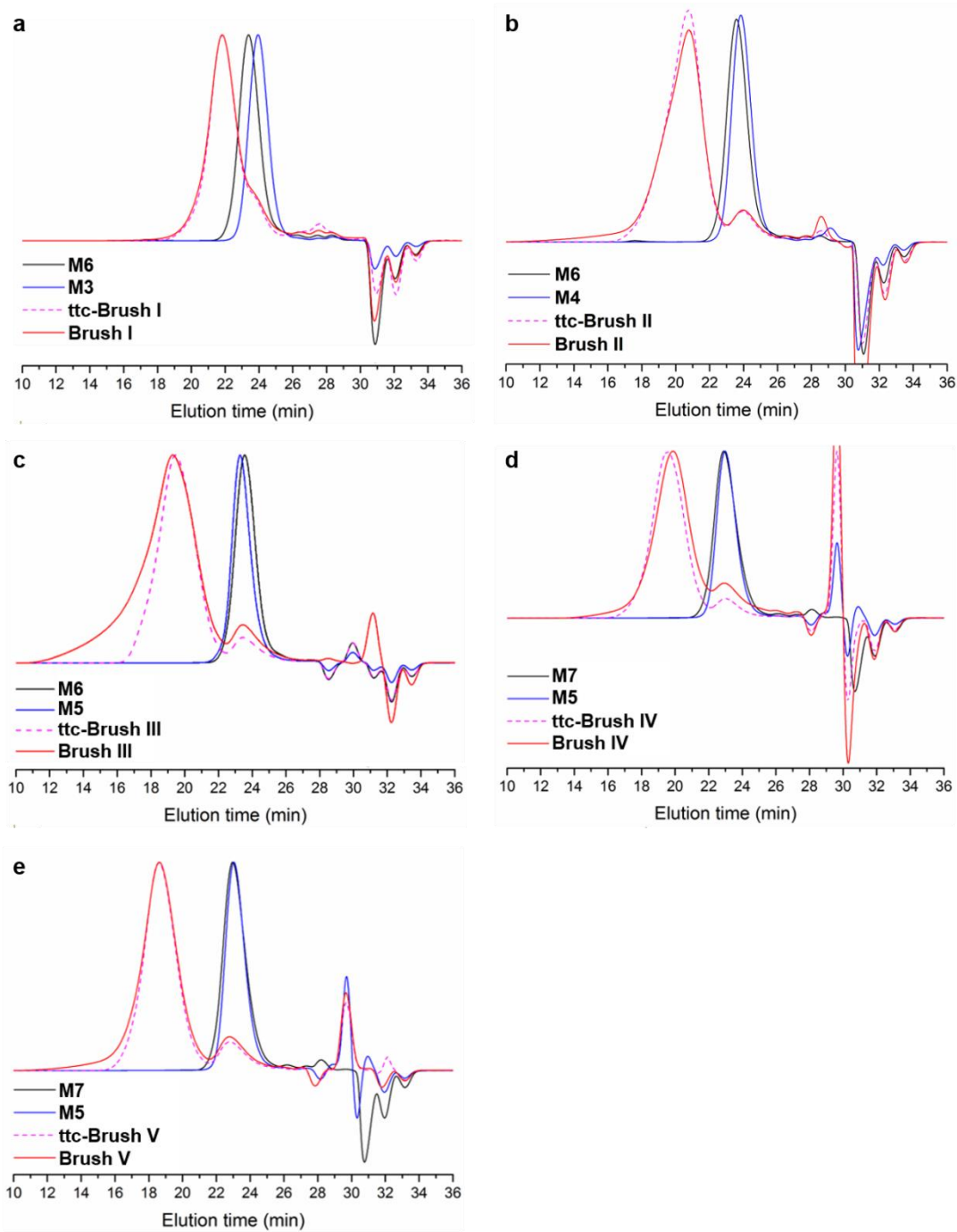


Figure 2.2. THF-SEC profiles of (a) **M6**, **M3**, **ttc-Brush I**, and **Brush I**, (b) **M6**, **M4**, **ttc-Brush II**, and **Brush II**, (c) **M6**, **M5**, **ttc-Brush III**, and **Brush III**, (d) **M7**, **M5**, **ttc-Brush IV**, and **Brush IV**, (e) **M7**, **M5**, **ttc-Brush V**, and **Brush V**, respectively.

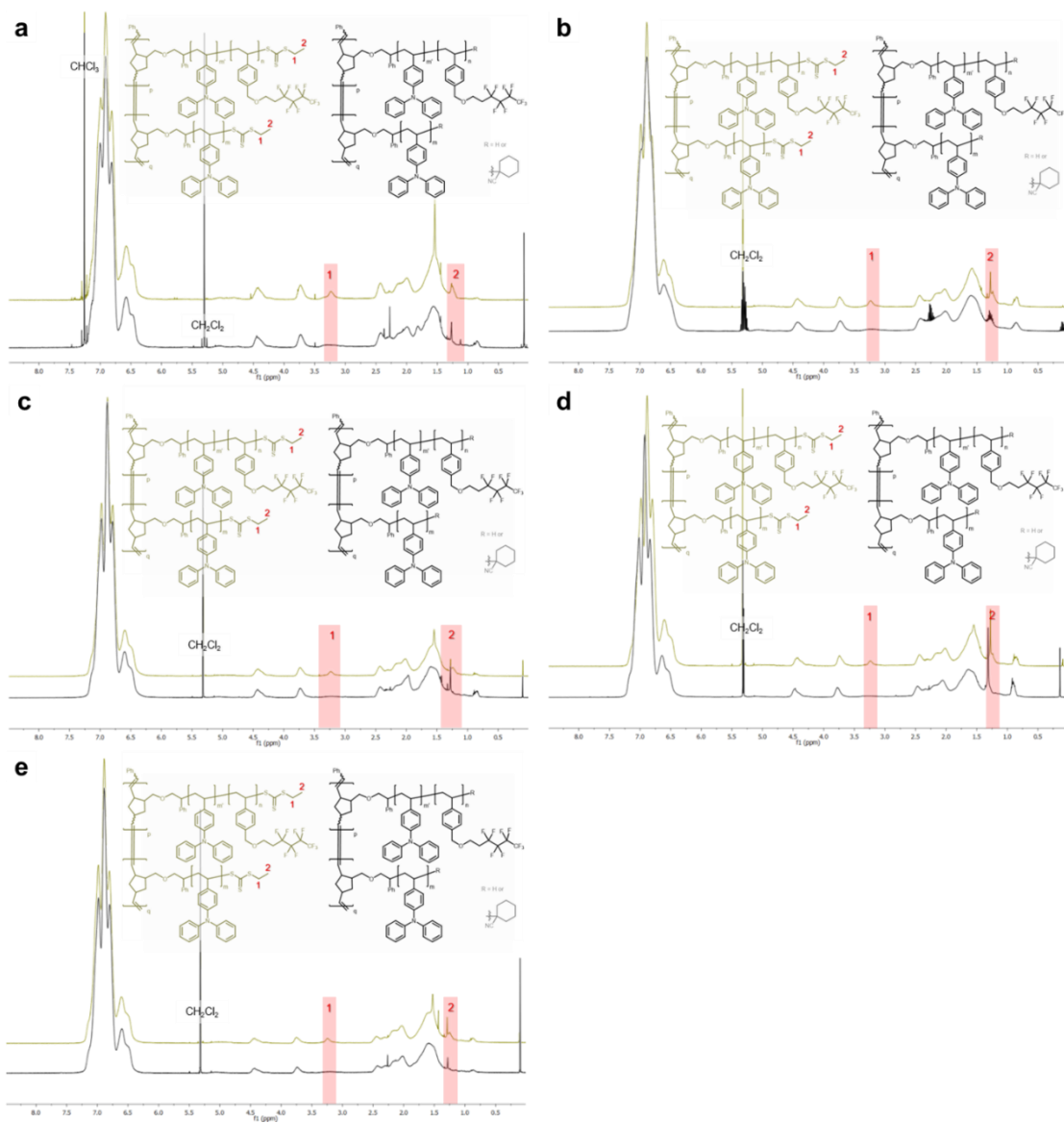


Figure 2.3. ^1H NMR (500 MHz, CD_2Cl_2) spectra of (a) **ttc-Brush I** (olive), and **Brush I** (black), (b) **ttc-Brush II** (olive), and **Brush II** (black), (c) **ttc-Brush III** (olive), and **Brush III** (black), (d) **ttc-Brush IV** (olive), and **Brush IV** (black), (e) **ttc-Brush V** (olive), and **Brush V** (black), respectively.

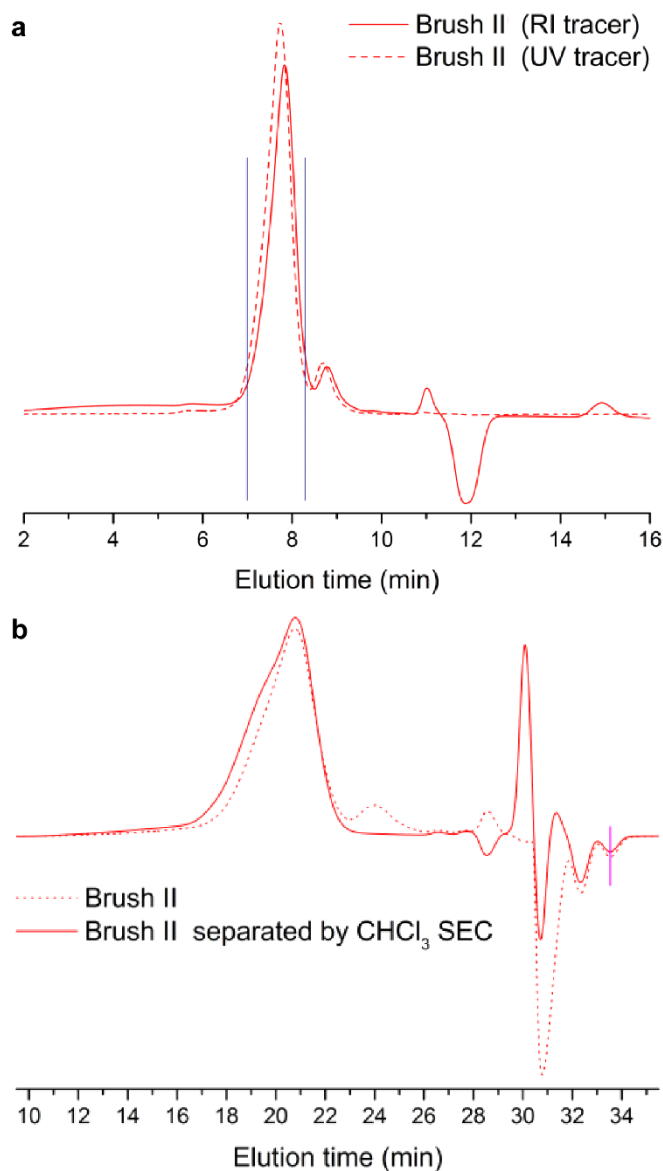


Figure 2.4. (a) SEC profiles of **Brush II**, using CHCl_3 as eluent. The royal lines indicated the “cut-off points” during CHCl_3 -SEC purification. (b) SEC profiles of **Brush II** before (dotted) and after (solid) CHCl_3 -SEC purification, using THF as eluent. The magenta line indicated the aligned solvent peaks.

It is noteworthy that the M_n of purified **ttc-Brush** and **Brush I-V** (Table 2.4) from SEC-MALS measurements were less than the theoretical values, calculated from the corresponding ROMP feed ratio and the macromonomer conversions. The discrepancy in

molar masses was initially attributed to overestimated specific refractive index increment (dn/dc) values from the online SEC measurements. However, the M_n of **Brush I** derived from the dn/dc value determined by batch analysis with the differential refractometer only showed < 10% increase relative to the molar mass obtained from online SEC-MALS measurement. This result intrigued us to speculate that the overestimated dn/dc values might be related to certain atypical photophysical properties of HTBs in solution.

Photophysical Properties of HTBs in Solutions. Figure 2.5a showed the representative UV–vis absorption spectra of HTBs (**Brush I** and **V**, *ca.* 0.29 and 0.35 of TPA concentration, respectively) and the linear NB-PVTPA₃₀ (**M4**, *ca.* 0.34 mM of TPA concentration) in THF. The noticeable variation of absorption intensity between **Brush V** and **M4** with comparable TPA concentrations suggested different stacking mode of TPAs within molecular bottlebrush and linear polymeric frameworks. Despite the absence of UV–vis absorption above 400 nm, near-infrared (NIR) fluorescence emissions peaked at ~725 nm were observed for both brushes (Figure 2.5b) upon excitation at 660 nm, the wavelength of the differential refractometer light source. A similar phenomenon was also perceived for the 0.1 mg/mL THF solution of **ttc-Brush V** (~0.34 mM of TPA concentration, Figure 2.6a). In comparison with the linear counterpart, the molecular bottlebrush topological factor produced over 2-folds enhancements of the NIR fluorescence emission signals, which subsequently caused stronger refractive index responses than linear NB-PVTPA and resulted in the overestimated dn/dc values for bottlebrushes. The NIR fluorogenicity of HTBs also exhibited a solvent polarity dependency. As shown in Figures 2.5c and 2.6b, the intensity of 725 nm emissions in less

polar dichloromethane underwent ~64%, ~50%, and ~57% of decrease for **Brush I, V**, and **ttc-Brush V**, respectively. In chloroform with the least as-surveyed solvent polarity, we did not observe any perceptible NIR fluorescence emissions.

The origin of NIR fluorescence emission was preliminarily investigated. Excited at varied wavelengths within the UV absorption area of **Brush V**, *i.e.*, 230, 250, 270, 290, 310, 330, and 350 nm, respectively, two emission bands at ~340–575 nm and ~680–900 nm were observed (Figure 2.5d). Interestingly, the intensity of each emission exhibited a non-linear relationship with the UV absorption. In fact, **Brush V** showed extremely lower fluorogenity upon excitation at both 290 and 310 nm, which have ~40% higher UV absorptions than 350 nm (Figure 2.6b), an effective excitation wavelength that could produce over 20-folds increase of fluorescent signals. Excitation at 330 nm could achieve the highest intensities for the dual emissions. These results, along with the solvent polarity-responsive nature, indicated a topology-dependent two-photon induced charge transfer fluorescence character for the NIR emission of HTBs excitation at 660 nm. Comprehensive studies on the mechanism and the structure-activity-relationship are currently undergoing.

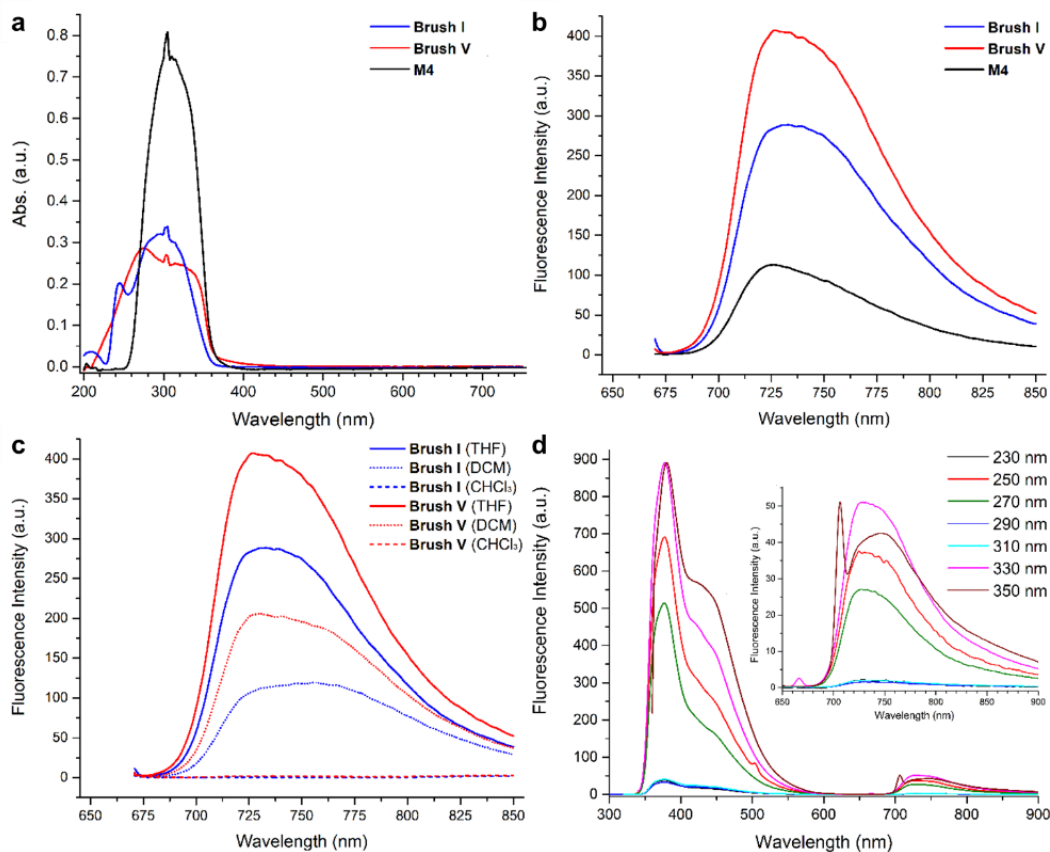


Figure 2.5. Photophysical properties of polymers bearing pendant TPA functionalities. (a) Representative UV-vis spectra of **HTBs** and **PVTPAs** in THF (red, **Brush V**; blue, **Brush I**; black, **M4**). (b) Fluorescence emission spectra excitation at 660 nm of **Brush V** (red), **Brush I** (blue), and **M4** (black) in THF, respectively. (c) Solvent polarity-responsive fluorescence emission spectra of **Brush I** (blue) and **V** (red). (d) Fluorescence emission spectra excitation at varied wavelengths of **Brush V** in THF. The insertion was the fluorescence emission profiles in the NIR range. Sample concentrations: 0.1 mg/mL.

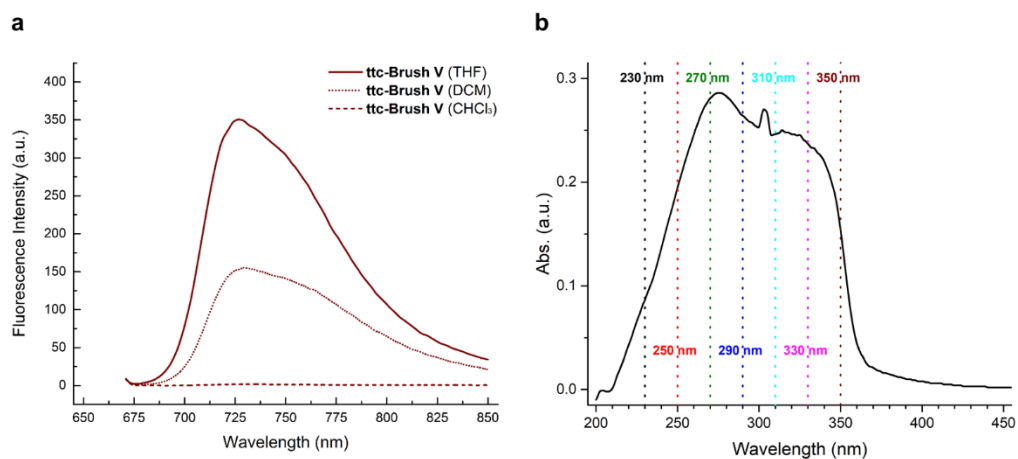


Figure 2.6. (a) Emission spectra of **ttc-Brush V** excitation at 660 nm in THF (solid), CH₂Cl₂ (dot), and CHCl₃ (dash). Sample concentration: 0.1 mg/mL. (b) UV-vis spectrum between 200 and 455 nm of **Brush V** in THF with indications of excitation wavelengths.

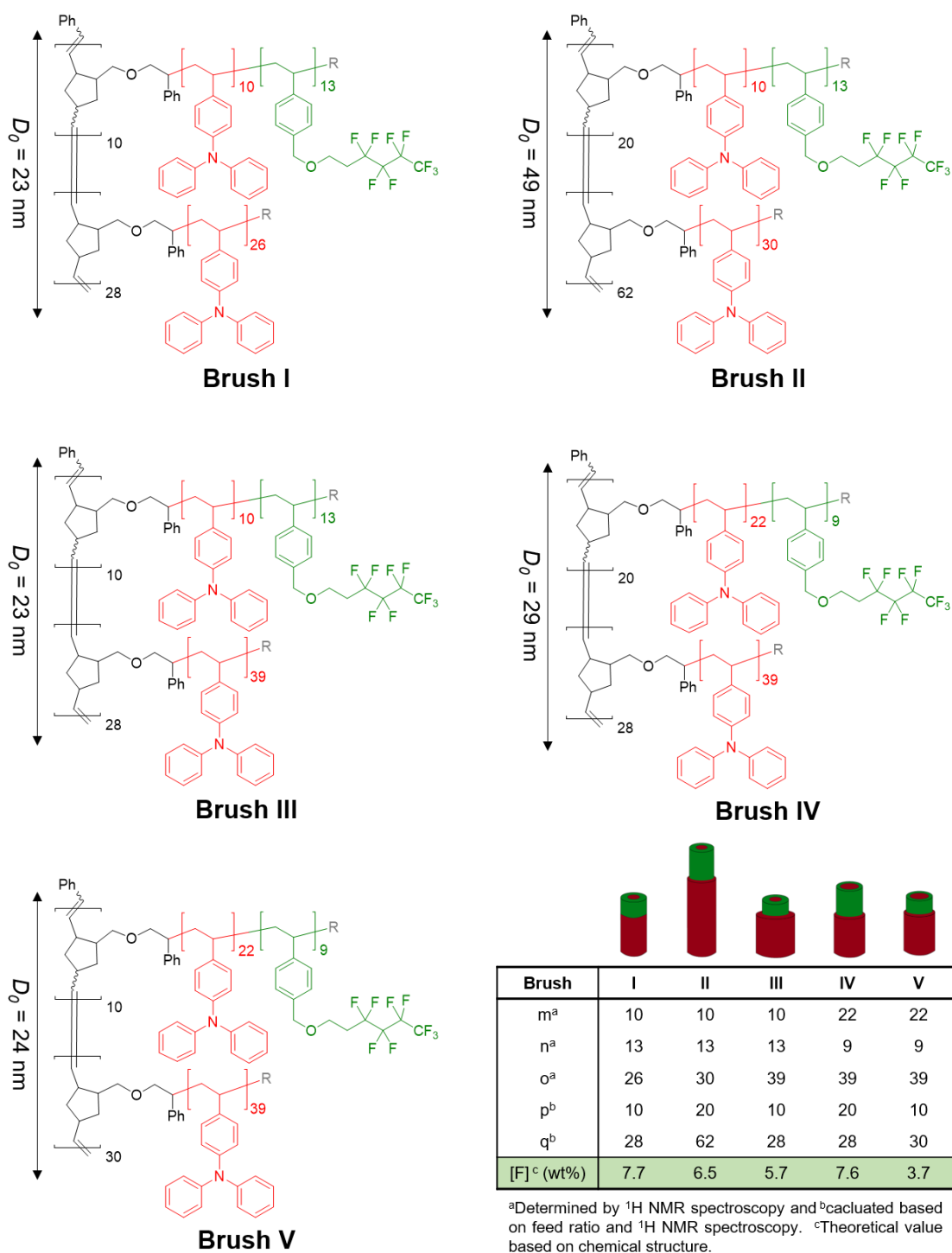


Figure 2.7. Summary of **Brushes I-V** (D_0 : contour length of polynorbornene backbone). The fluorine content was calculated from **ttc-Brushes I-V**.

Characterizations of HTL Thin Films on Si Wafers. HTL thin films on Si wafers, with film thicknesses (FTs) commensurate to the contour length of each HTB PNB backbone (D_0 , Figure 2.7), were prepared by an optimized spin-casting and thermal annealing protocol. As characterized by tapping-mode atomic force microscopy (AFM) (Figures 2.8 and 2.9), the films from **Brush I, III, IV, and V** exhibited homogeneous surface topographies with height root-mean-square roughnesses of < 1 nm. The film surface homogeneity was further confirmed by surface coverage analysis from Au_{400}^{4+} cluster secondary-ion mass spectrometry (SIMS, Figure 2.10 and Table 2.6). For **Brush II** films, obvious defects (depth: ≈ 5 nm; diameter: > 200 nm) were revealed from AFM height imaging, which suggested mixed morphologies of the films.²⁰ Thin films composed of purer but more ill-defined **Brush II**, obtained from CHCl_3 -SEC purification, were also prepared and imaged by AFM. However, significantly-increased defects, in terms of density and feature size, were observed for these films (Figure 2.11).

From the SIMS fluorine depth profiling of **Brush I, III, and V** as-cast films (Figures 2.12a–2.12c), the F species were predominantly located within the top-7 nm region of each sample, supporting the vertical orientation of brush PNB backbones.¹⁹ Upon thermal annealing below the glass transition temperature of HTBs (145 °C, Figure 2.13), the F/C⁻ side peaks located at *ca.* 15 nm-depth of **Brush III** and **V** films decreased, indicating improvement of the brush vertical alignment. For **Brush I** film, the thermal annealing did not result in such enhancement. **Brush III** showed better vertical alignment than **Brush I** and **Brush V**, due to its structural and compositional characteristics, *i.e.*, relatively stronger substrate adhesion from the longer PVTTPA side chains (PVTTPA₃₉ *vs.*

PVTPA₂₆) and enhanced surface energy-driven assistance from the larger fluorinated blocks (PNFHBS₁₃ vs. PNFHBS₉), respectively. The presence of three noticeable F-rich domains along the F depth profile of **Brush II** films (Figure 2.12d) indicated that **Brush II** exhibited poor perpendicular substrate-alignment. Similar unsatisfactory ordering was observed for **Brush IV** films, which showed an additional F-rich domain near the substrate that did not improve through thermal annealing (Figure 2.12e).

Table 2.5. Number of triphenylamine hole transporting functionalities in the single molecule of **LC** and **Brush I-V**.

| TPA (ea.) | LC | Brush I | Brush II | Brush III | Brush IV | Brush V |
|--|-----------|----------------|-----------------|------------------|-----------------|----------------|
| Single polymer^a | 50 | 828 | 2000 | 1192 | 1532 | 1390 |
| 1mL of film solution^{b, c} | 0.0036 | 0.0029 | 0.0091 | 0.0030 | 0.0047 | 0.0034 |

^aTheoretical value based on chemical structure. ^bCalculated based on theoretical molar mass. ^cFilm solution concentrations for each polymer to obtain monolayered films are—**LC**: 1 wt%, **Brush I**: 1 wt%, **Brush II**: 3 wt%, **Brush III**: 1 wt%, **Brush IV**: 1.5 wt%, **Brush V**: 1 wt%.

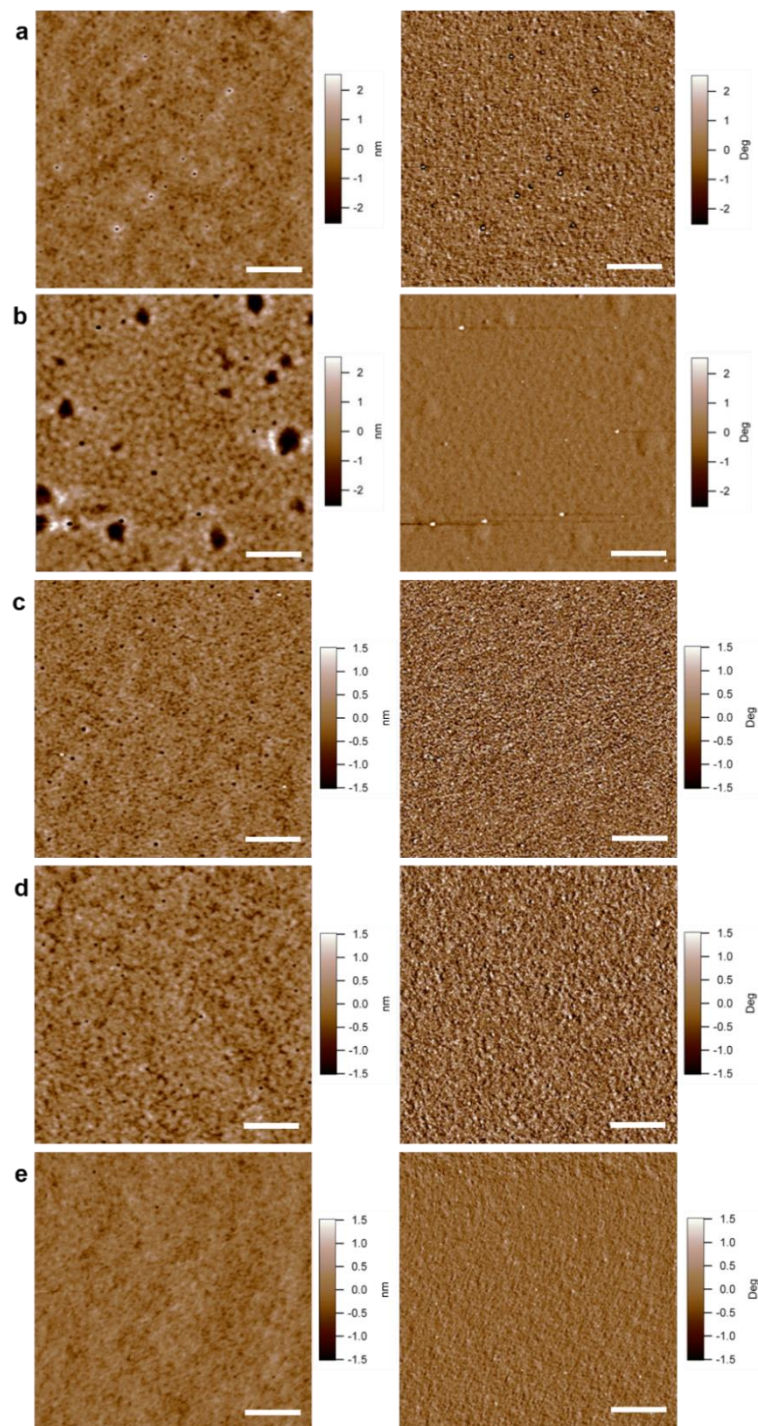


Figure 2.8. Tapping-mode AFM height (left) and phase (right) images of as-cast thin films of (a) **Brush I** (FT = 20 ± 1 nm), (b) **Brush II** (FT = 49 ± 1 nm), (c) **Brush III** (FT = 23 ± 1 nm), (d) **Brush IV** (FT = 29 ± 1 nm), (e) **Brush V** (FT = 20 ± 1 nm). The images were obtained with a 5×5 μm area. Scale-bars: 1 μm.

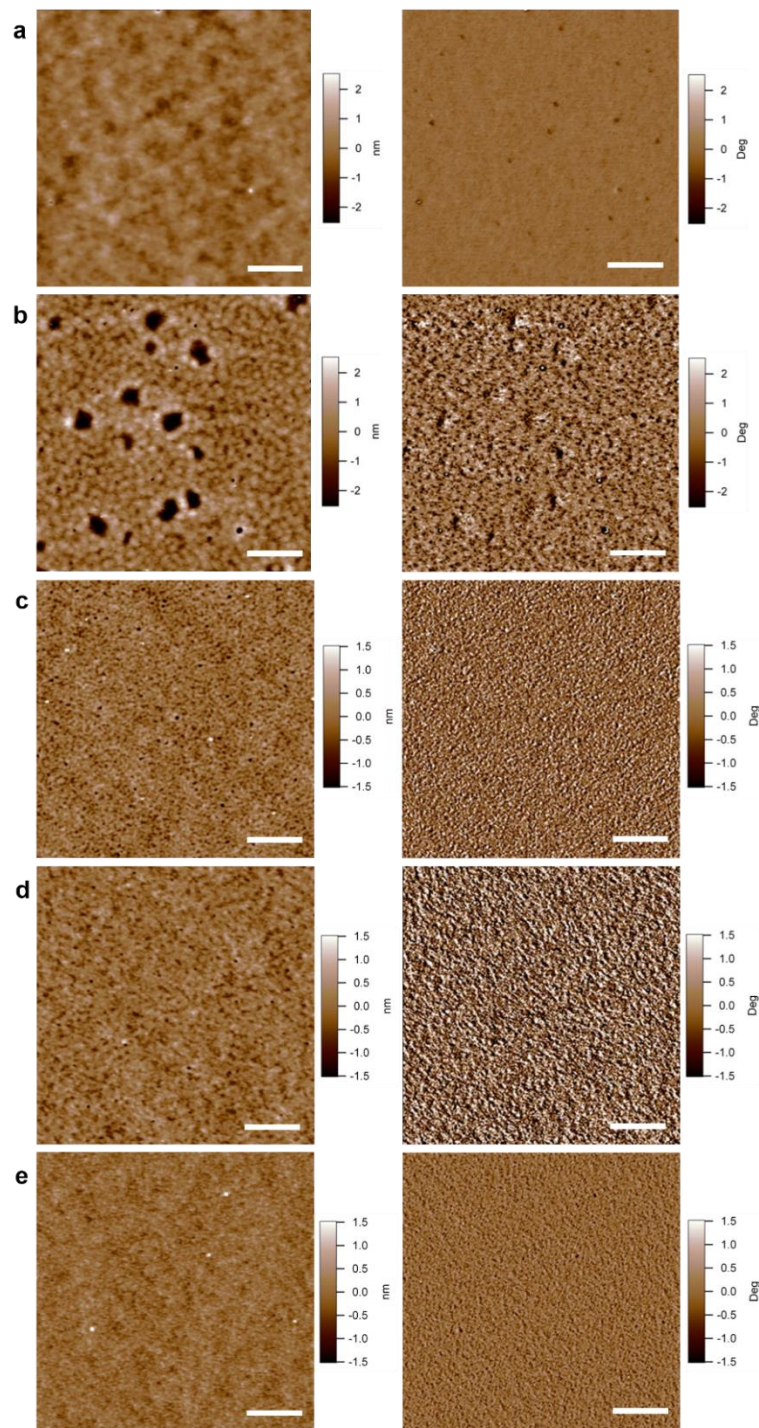


Figure 2.9. Tapping-mode AFM height (left) and phase (right) images of thermally-annealed thin films of (a) **Brush I** (FT = 20 ± 1 nm), (b) **Brush II** (FT = 49 ± 1 nm), (c) **Brush III** (FT = 22 ± 1 nm), (d) **Brush IV** (FT = 26 ± 1 nm), (e) **Brush V** (FT = 19 ± 1 nm). The images were obtained with a $5 \times 5 \mu\text{m}$ area. Scale-bars: 1 μm .

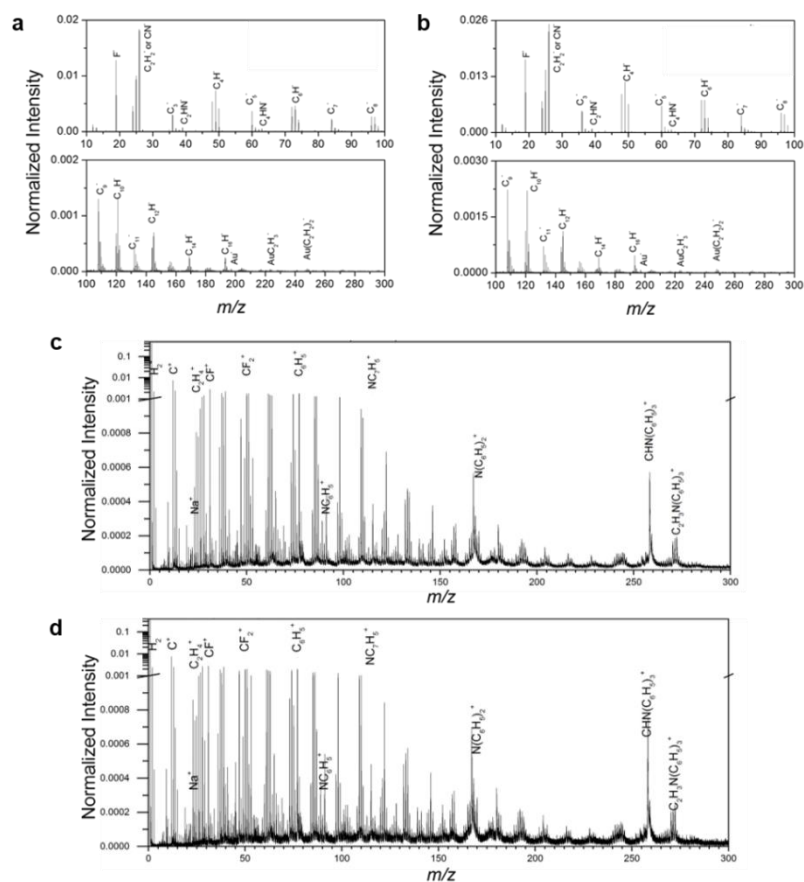


Figure 2.10. Au_{400}^{4+} SIMS spectra of thin films of **Brush III** (negative mode; (a) as-cast, (b) thermally-annealed) and **Brush IV** (positive mode; (c) as-cast, (d) thermally-annealed).[#]

Table 2.6. Brush coverage of **Brush III** and **Brush IV** calculated from Au_{400}^{4+} SIMS surface analysis data.^{##}

| Brush | | Brush Coverage | Q^a (F⁻, C₄NH⁺) |
|--------------|--------------------|-----------------------|---|
| III | As-cast | 93 ± 1.5% | 0.9 |
| | Thermally-annealed | 93 ± 2.4% | 1.0 |
| IV | As-cast | 90 ± 0.5% | 1.1 |
| | Thermally-annealed | 79 ± 0.7% | 1.3 |

^aCorrelation coefficient.

[#] Collected by Dr. Michael J. Eller (Texas A&M University).

^{##} Analyzed by Dr. Michael J. Eller (Texas A&M University).

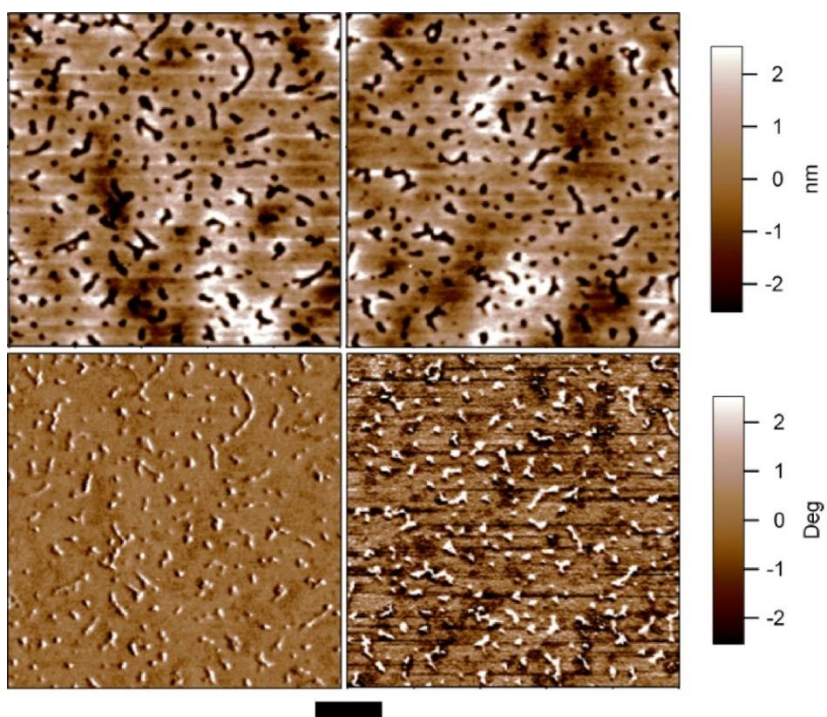


Figure 2.11. Tapping-mode AFM height (top row) and phase (bottom row) images of as-cast (left column, $FT = 55 \pm 2$ nm) and thermally-annealed (right column, $FT = 54 \pm 2$ nm) thin films of CHCl_3 -SEC purified **Brush II**. The images were obtained with a 5×5 μm area. Scale-bar: 1 μm .

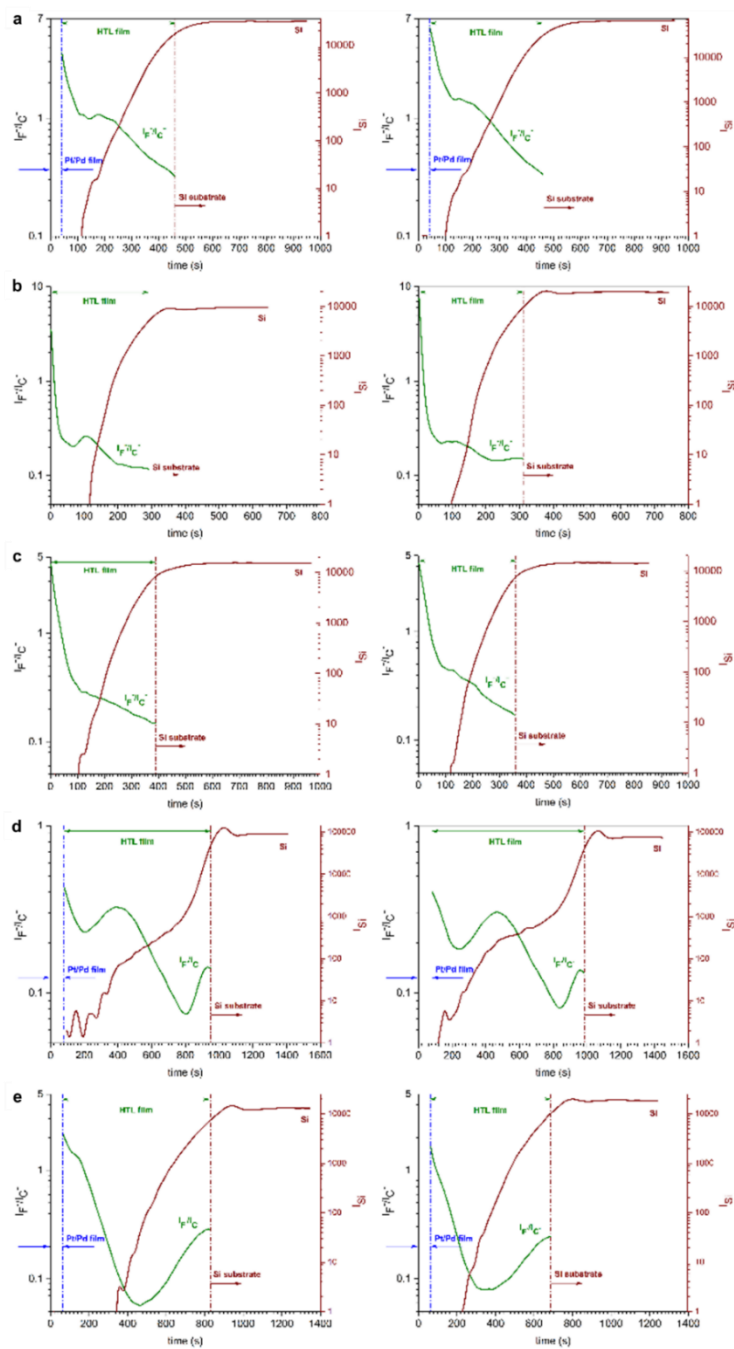


Figure 2.12. SIMS fluorine depth profiles (left, as-cast; right, thermally-annealed) of (a) **Brush I**, (b) **Brush III**, (c) **Brush V**, (d) **Brush II**, and (e) **Brush IV** films on Si wafers, respectively.[#]

[#] Collected by Dr. Stanislav V. Verkhotourov (Texas A&M University).

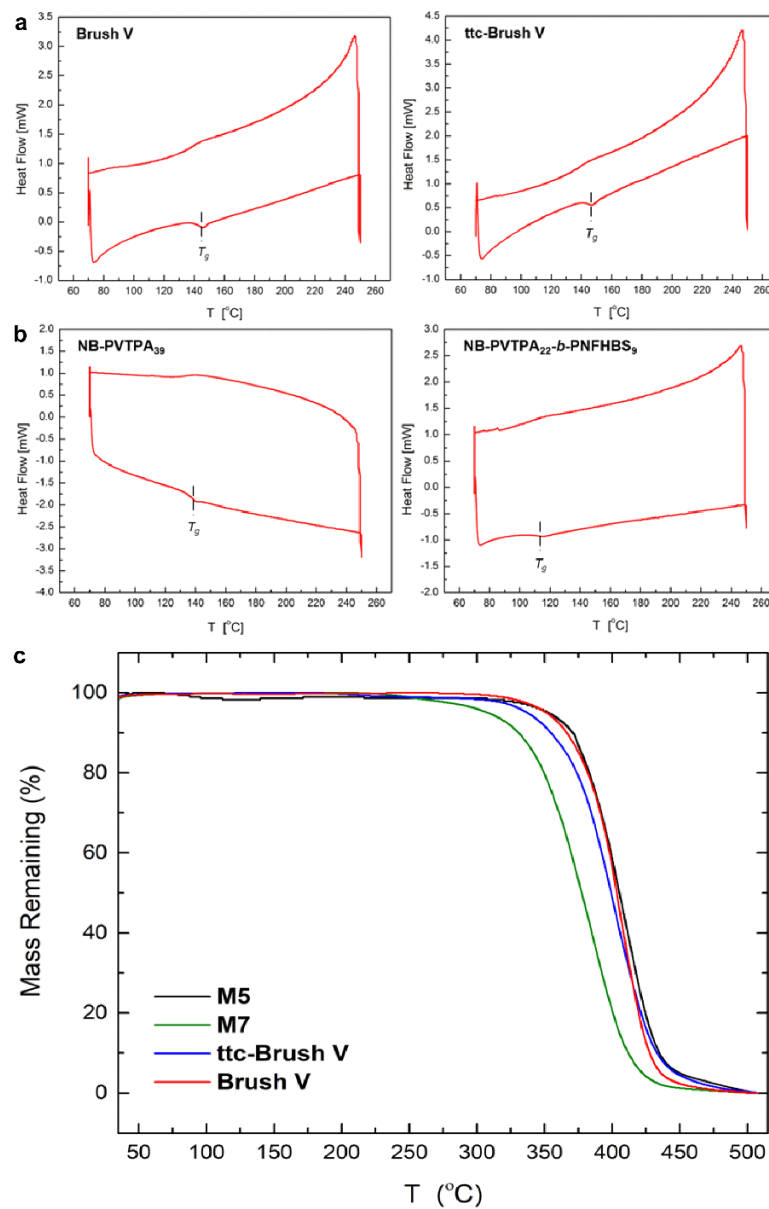


Figure 2.13. Representative thermal characterizations of HTBs and related macromonomer precursors. (a) DSC traces of **Brush V** (left) and **ttc-Brush V** (right), respectively. (b) DSC traces of NB-PVTPA₃₉ (**M5**, left) and NB-PVTPA₂₂-b-PNFHBS₉ (**M7**, right), respectively. DSC traces were obtained under N₂ atmosphere with a heating and cooling rate of 10 °C/min. The glass transition temperatures (T_g s) were labeled on the thermograms. (c) TGA traces of **M5**, **M7**, **ttc-Brush V**, and **Brush V**. TGA traces were obtained under Ar atmosphere with a heating rate of 5 °C/min.

The molecular orientation of TPAs within HTL films was characterized by variable angle spectral ellipsometry (VASE, Figure 2.14).⁷¹ The calculated order parameters (S s) from **Brush I**, **III**, and **V** as-cast films showed preferential “face-on” packing of TPAs with S values of -0.157 ± 0.001 , -0.169 ± 0.006 , and -0.100 ± 0.006 , respectively. After thermal annealing for 3 min, the anisotropy of **Brush III** and **V** films exhibited over 50% improvements ($S = -0.302 \pm 0.001$ and -0.165 ± 0.006 , respectively), while the annealed **Brush I** film did not show conspicuous variation ($S = -0.152 \pm 0.011$). Longer thermal annealing times, *i.e.*, 10 min and 20 min, were also attempted. However, the extended annealing time produced a >20 % decrease in anisotropy. By comparison, the films from **Brush II** and **IV**, homobrush control [P(NB-*g*-PTVPA₂₆)₃₀], and linear control (**LC**, PVTVA₅₀) polymers only showed isotropic packings of TPAs within films ($S_s \approx 0$). It should be noted that these S_{VASE} values only represented the spatial orderliness of TPAs within HTL films on neat Si wafers, as VASE was not suitable for anisotropic characterization of multiple-layered films. While the majority of the OLED devices contain HILs under the HTLs, the alignment of HTBs in HTL films could vary, due to additional interactions between PVTVA grafts and HILs. Therefore, the actual extents of TPA “face-on” packings between **Brush I**, **III**, and **V** in real devices might not be as significant as S_{VASE} values base on neat Si wafers denoted.

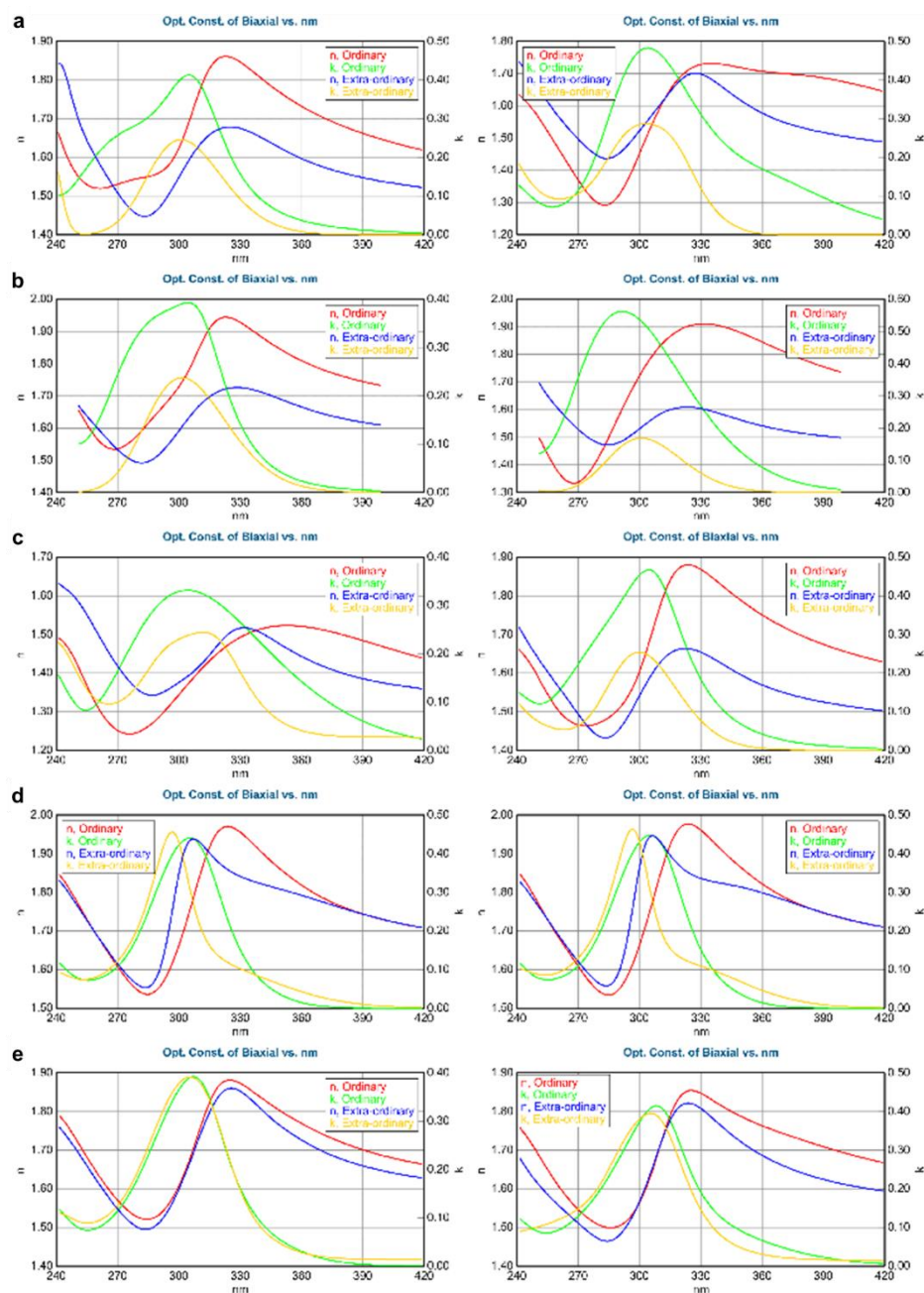


Figure 2.14. Optical constants (n : refractive index; k : extinction coefficient; subscripts o and e refer to the ordinary and extraordinary directions, respectively) vs. wavelength profiles at (0, 0) coordinates of as-cast (left column) and thermally-annealed (right column) (a) **Brush I**, (b) **Brush III**, (c) **Brush V**, (d) **Brush II**, and (e) **Brush IV** films on neat Si wafers, respectively.[#]

[#] Collected by Dr. Chun Liu (DowDupont).

Thermally-annealed **Brush III** thin films on substrates coated with poly(3,4-ethylene dioxythiophene):polystyrene sulfonate (PEDOT:PSS) HILs were then explored (Figure 2.15). Although the films on PEDOT:PSS-coated Si wafer and indium tin oxide (ITO) glass exhibited slightly-increased heterogeneities (Figures 2.15a and 2.15b vs. 2.9c), their Au₄₀₀⁴⁺ cluster SIMS surface analyses revealed comparable brush coverages (> 85%) and correlation coefficients (~ 0.9) as the control film on neat Si wafer. By implementing two-dimensional (2D) grazing-incidence small-angle X-ray scattering (GISAXS),⁶⁷ a series of discrete peaks along the out-of-plane direction were detected for **Brush III** films on the wafer (Figure 2.16a) and on the HIL-coated Si wafer (Figure 2.16b), respectively. The absence of scattering patterns along the in-plane direction, together with the agreement of FT_{GISAXS}, *i.e.*, 21 and 20 nm for films on neat and PEDOT:PSS-coated Si wafers (Figure 2.17a), respectively, provided additional evidence for the vertical orientation of brush PNB backbones regardless of the types of substrates, although the extent of alignment could have minor differences.

The packing information of TPAs within **Brush III** film on HIL was probed by using 2D grazing-incidence wide-angle scattering (GIWAXS),^{40, 47-48} as VASE was not suitable for anisotropic characterization of multiple-layered films. As shown in Figures 2.16c and 2.16d, there were no noticeable scattering peaks observed along the in-plane direction for both films on neat and PEDOT:PSS-coated Si wafers. By comparison, relatively-broader π - π stacking scattering signals along the out-of-plane direction were revealed by GIWAXS. Centered at $q_z \sim 1.845 \text{ \AA}^{-1}$ (π -stacking distance, $d_\pi = 3.405 \text{ \AA}$) and 1.854 \AA^{-1} ($d_\pi = 3.389 \text{ \AA}$) for **Brush III** films on Si wafers with and without HIL coating,

respectively, the TPA stacking exhibited sufficient similarity (Figure 2.17b), which confirmed that the preferential “face-on” alignments could be achieved through orthogonal spin-casting of HTBs. Due to the intrinsic crystallinity of ITO, we could not obtain meaningful results from the GIWAXS characterization of **Brush III** film on HIL-coated ITO glass (data not shown). Taking account of the ~40 nm FT of PEDOT:PSS layer, it is reasonable to speculate that the substrate-induced distinctiveness of HTL films prepared under the same conditions should be neglectable.

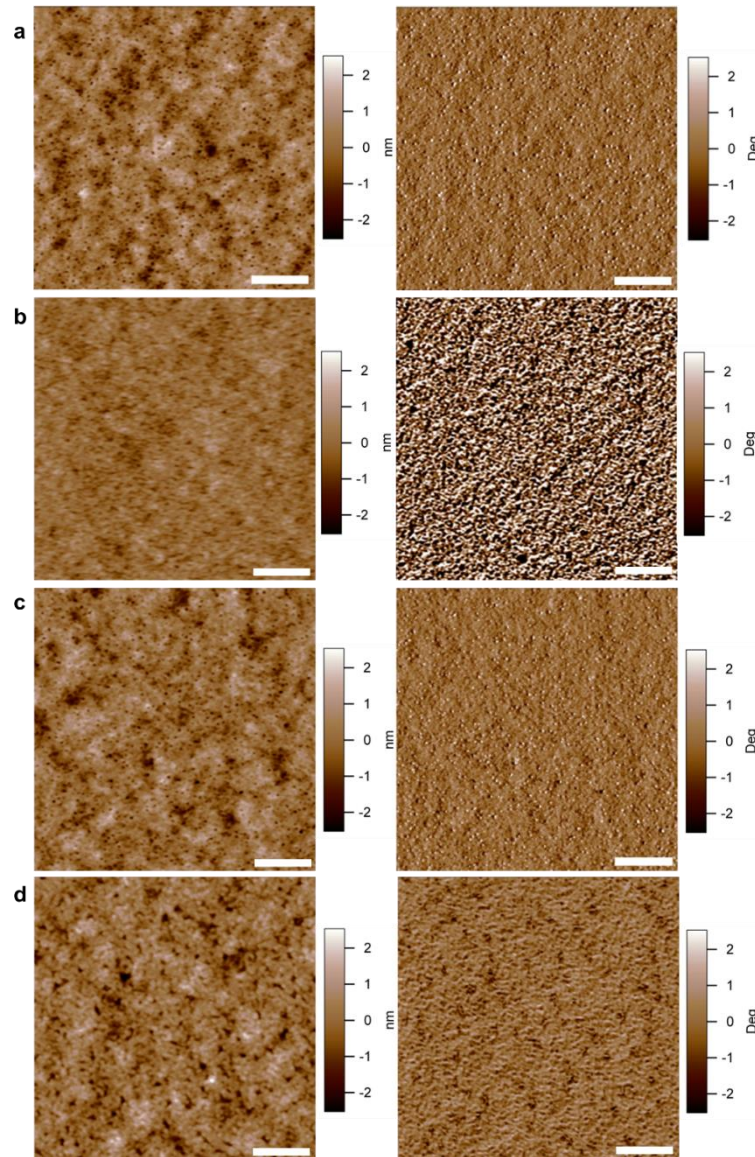


Figure 2.15. Tapping-mode AFM height (top) and phase (bottom) images of thermally-annealed (a) **Brush III** thin films on PEDOT:PSS coated Si wafer (HTL FT = 25 ± 1 nm), (b) **Brush III** thin films on PEDOT:PSS coated ITO glass (HTL FT = 24 ± 1 nm), (c) **Brush I** thin films on PEDOT:PSS coated ITO glass (HTL FT = 24 ± 1 nm), and (d) **Brush V** thin films on PEDOT:PSS coated ITO glass (HTL FT = 25 ± 2 nm), respectively. The images were obtained with a 5×5 μm area. Scale-bars: 1 μm .

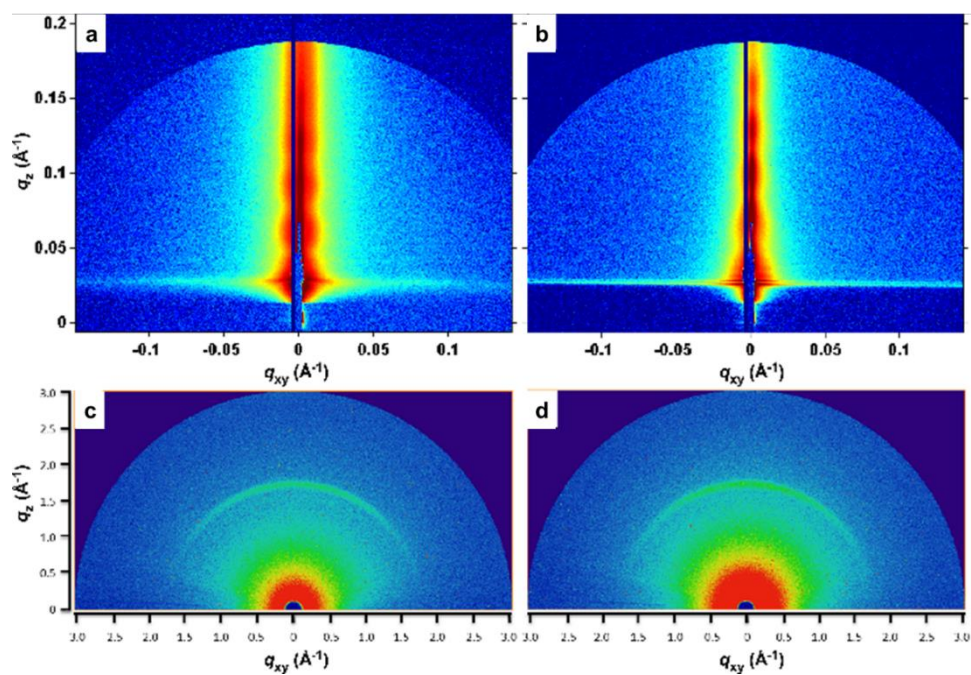


Figure 2.16. GISAXS (top row) and GIWAXS (bottom row) characterizations of thermally-annealed **Brush III** thin films on neat (a and c) and PEDOT:PSS-coated (b and d) Si wafers, respectively. q_{xy} and q_z were defined as coordinates of the reciprocal space.[#]

[#] Collected by Dr. Yen-Hao Lin (Texas A&M University).

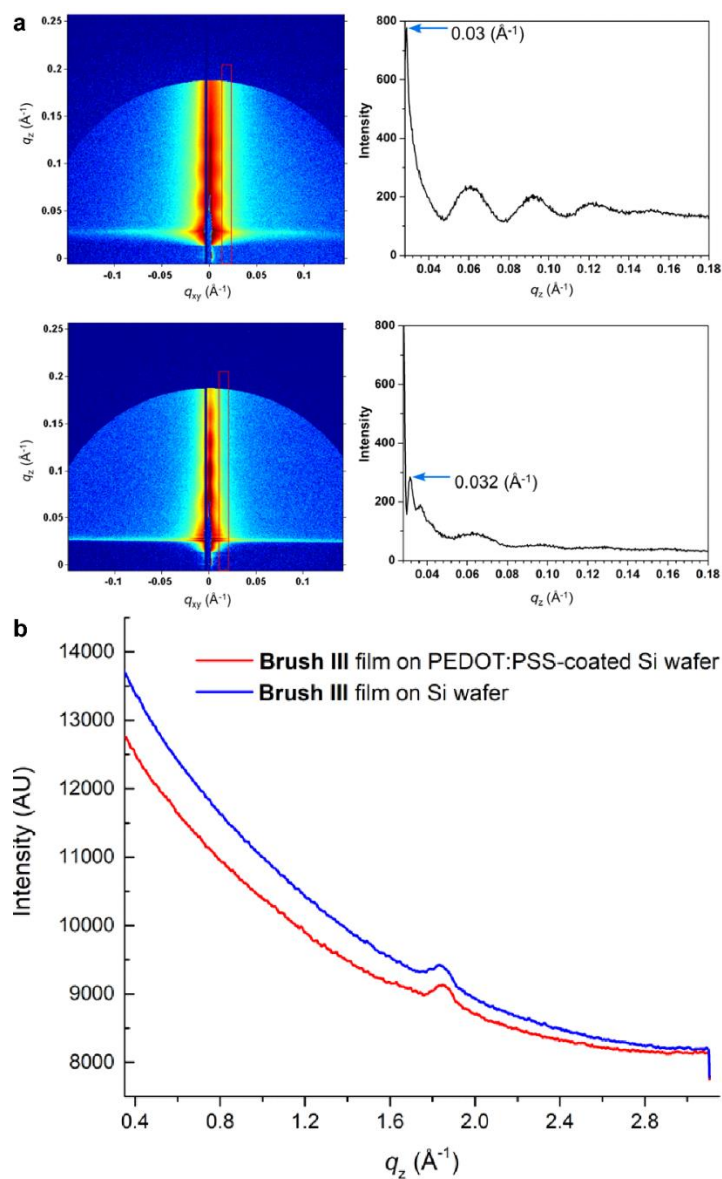


Figure 2.17. (a) GISAXS characterizations of thermally-annealed **Brush III** thin films on neat (top) and PEDOT:PSS-coated (bottom) Si wafers, respectively. The plots (right column) show the in-plane line cuts (red rectangle) through the full patterns (left column). The corresponding FTs at $q_z = 0.03$ and 0.032 \AA^{-1} (indicated by blue arrows) were 21 and 20 nm, respectively. (b) GIWAXS 1D diffraction curves along with the q_z directions for thermally-annealed **Brush III** thin films on neat and PEDOT:PSS coated Si wafer, respectively. q_{xy} and q_z were defined as coordinates of the reciprocal space.[#]

[#] Collected by Dr. Yen-Hao Lin (Texas A&M University).

Electronic Property of Brush III. The energy level of the highest occupied molecular orbital (HOMO) of **Brush III**, -5.20 eV, was derived from measured oxidation potential in CH₂Cl₂ by cyclic voltammetry (Figure 2.18). This value was lower than the theoretical calculations (-4.92 and -4.94 eV, Figure 2.19; first and last entries). However, it was closer to the HOMO energy level of PEDOT:PSS (-5.0 to -5.2 eV) and was located within an optimal HTL HOMO energy range (-5.1 to -5.3 eV),⁷² which is critical for improving red- and green-phosphorescence OLED device performance.⁷³ Due to the failure on obtaining the electron affinity by cyclic voltammetry, we did not comprehensively explore the electronic properties of HTBs.

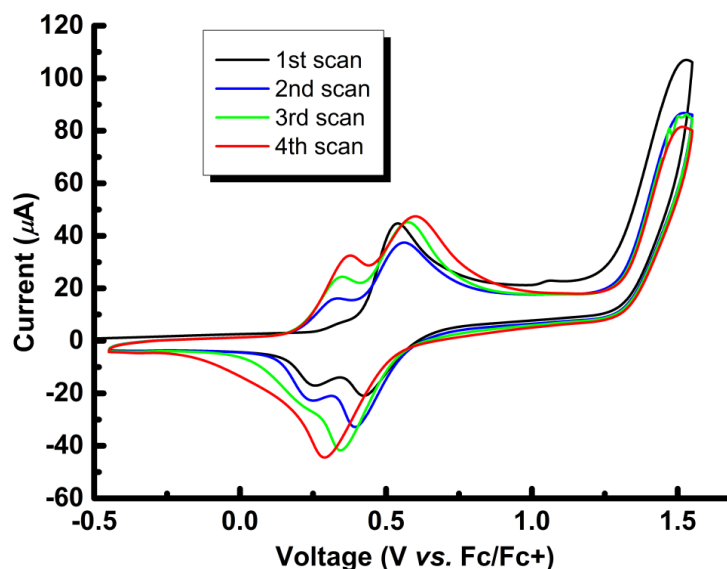


Figure 2.18. Cyclic voltammetry profiles of **Brush III** in CH₂Cl₂.[#]

[#] Collected by Dr. Tianyu Yuan (Texas A&M University).

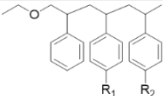
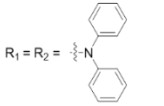
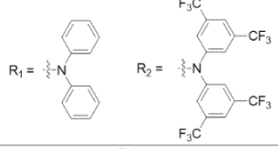
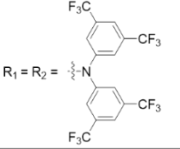
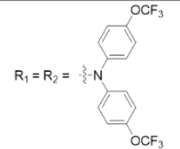
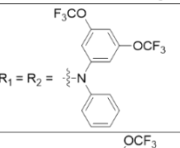
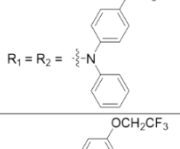
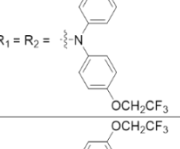
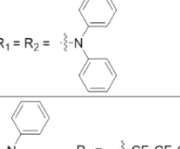
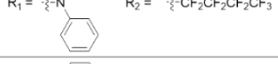
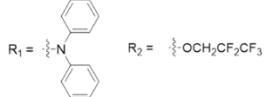
|  | | |
|---|----------|----------|
| R ₁ , R ₂ | HOMO | LUMO |
|  | -4.92 eV | -0.33 eV |
|  | -5.00 eV | -1.70 eV |
|  | -5.92 eV | -1.80 eV |
|  | -5.29 eV | -0.87 eV |
|  | -5.34 eV | -0.76 eV |
|  | -5.10 eV | -0.62 eV |
|  | -4.85 eV | -0.62 eV |
|  | -4.92 eV | -0.52 eV |
|  | -4.98 eV | -1.73 eV |
|  | -4.94 eV | -0.37 eV |

Figure 2.19. Molecular fragment structures for DFT calculations of HOMO and LUMO levels to define a selection of the bottlebrush composition and structural design.

Hole-only Device (HOD) Evaluation of HTB. HODs comprising **Brush III** (HOD-**III**) and **LC** (HOD-**LC**) as HTLs, respectively, were produced with a configuration of ITO/PEDOT:PSS (40 nm)/HTL (~25 nm)/Al (100nm). As shown in Figure 2.20a, the current density of anisotropic HOD-**III** showed typical behavior of injection-limited and Poole-Frenkel space-charge limited regimes⁷⁴ at low and high fields, respectively. By comparison, isotropic HOD-**LC** exhibited a combination of different types of hole mobility including Ohmic, space-charge limited current, and Poole-Frenkel, which enabled higher current density than HOD-**III** at each surveyed voltage/electric field. As a note, although the calculated hole mobility of HOD-**III** at the highest electric field showed comparable number as HOD-**LC** (Figure 2.20b), the intrinsically-thin nature of HTL films made the results less reliable.

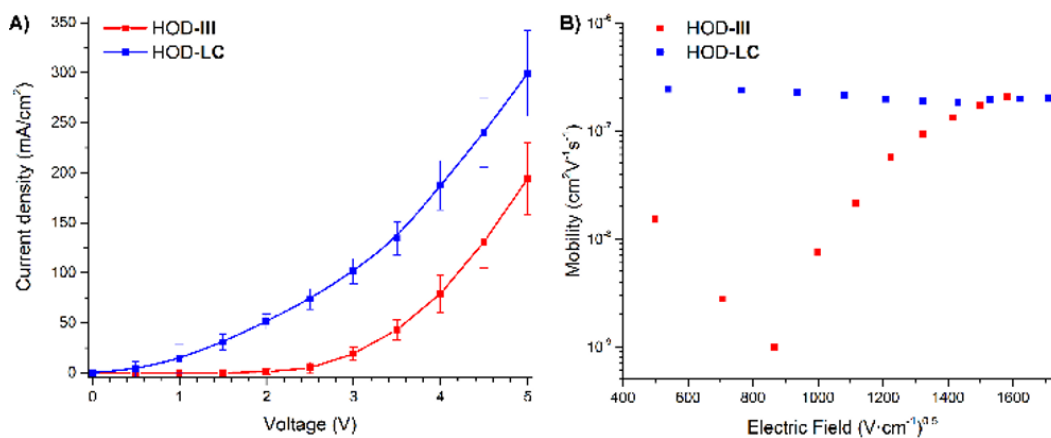


Figure 2.20. Performance evaluations of HODs comprising **Brush III** (HOD-**III**) and **LC** (HOD-**LC**), respectively. (a) Current density vs. voltage plots. (b) Hole mobility vs. square root of electric field plots.[#]

[#] Collected by Dr. W. Hunter Woodward (DowDupont).

OLED Full Device Evaluation of HTBs. The key motivation for this study, *i.e.*, anisotropic packing of TPAs into preferential “face-on” orientation within HTL would be beneficial for improving the device performance, was not strongly supported by the results from HOD testing. Therefore, multiple-layered thermally activated delayed fluorescence (TADF) OLED⁷⁵⁻⁷⁷ full devices comprising HTBs (**Brush I, III, and V**) that showed anisotropic packing of TPAs and isotropic PVTPA₅₀ linear control (**LC**) as HTLs were prepared and utilized to explore the relationship between device performance and the anisotropy of HTL. Another linear polymer control with intrinsically-high hole mobility, poly(9,9-dioctylfluorene-*alt*-*N*-(4-sec-butyl phenyl)-diphenylamine) (TFB), was also introduced and compared. Upon fabricating brushes, or PVTPA₅₀, or TFB on PEDOS:PSS-coated ITO glass through spin-casting and thermally-annealing, 9,10-bis(4-(9*H*-carbazol-9-yl)-2,6-dimethyl phenyl)-9,10-diboraanthracene (CzDBA, a green TADF emitter),⁷⁸ 1,3,5-tri(3-pyridyl)-phen-3-ylbenzene (TmPyPB), 8-hydroxyquinolitolithium (Liq), and Al were sequentially deposited through vacuum depositions to construct emissive layer, ETL, electron injection layer, and cathode, respectively (Figure 2.21). All **I, III, IV, LC, and TFB** devices were build up based upon the following configuration: ITO/PEDOT:PSS (40 nm)/HTL (~25 nm)/CzDBA (40 nm)/TmPyPB (45 nm)/Liq (1 nm)/Al (100 nm). For each device, three randomly-selected pixels were measured (Figures 2.22–2.26).

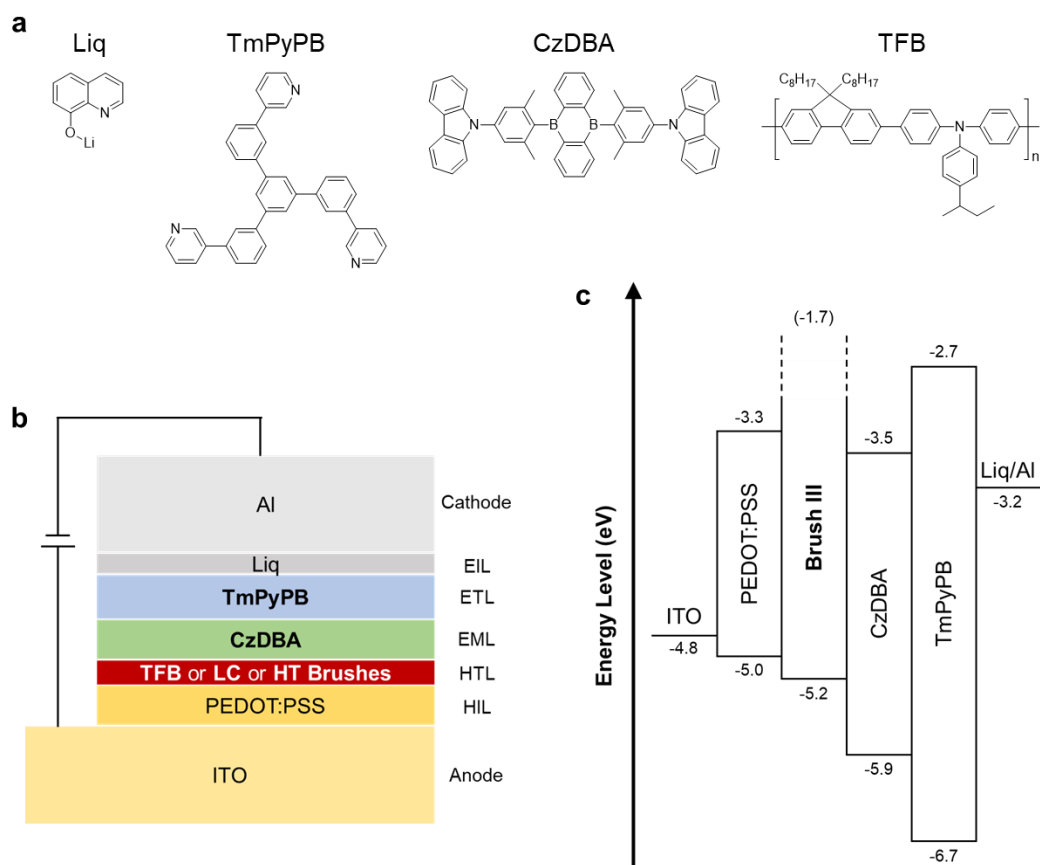


Figure 2.21. (a) Molecular structures of additional components used in the OLED devices. Liq: 8-hydroxyquinolinolato-lithium, CzDBA: 9,10-bis(4-(9H-carbazol-9-yl)-2,6-dimethylphenyl)-9,10-diboraanthracene, TmPyPB: 1,3,5-tri(*m*-pyridin-3-ylphenyl)benzene, TFB: poly(9,9-dioctylfluorene-*alt*-*N*-(4-*sec*-butylphenyl)-diphenylamine). (b) Device configuration and (c) Energy level diagram (The LUMO value, ca. -1.7 eV, of **Brush III** was estimated from the UV-vis spectrum and the cyclic voltammetry characterizations).

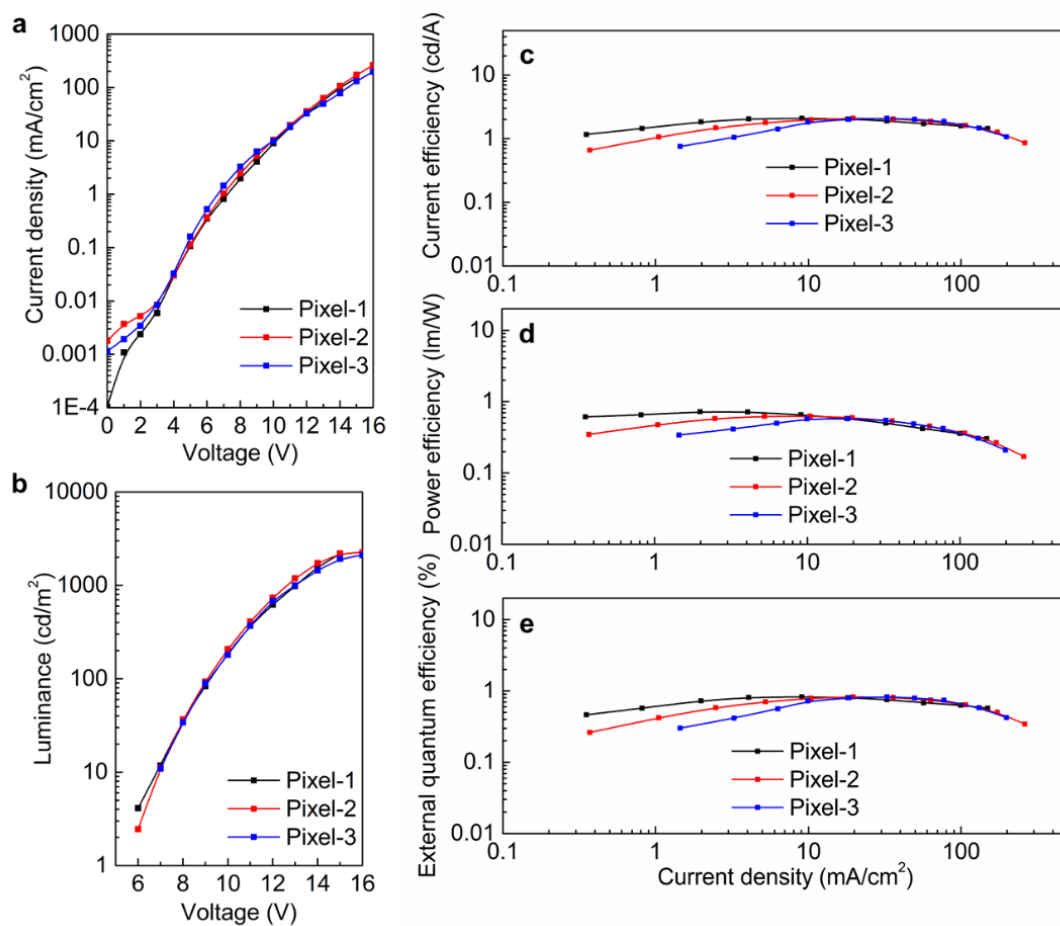


Figure 2.22. EL characterizations of **TFB** device. (a) Current density vs. voltage plots, (b) luminance vs. voltage plots, (c) current density efficiency, (d) power efficiency, (e) external quantum efficiency plots. Multilayered OLED device structure: ITO/PEDOT:PSS (40 nm)/**TFB** (25 nm)/CzDBA (40 nm)/TmPyPB (45 nm)/Liq (1nm)/Al (100 nm).#

Collected by Dr. Guohua Xie (Wuhan University).

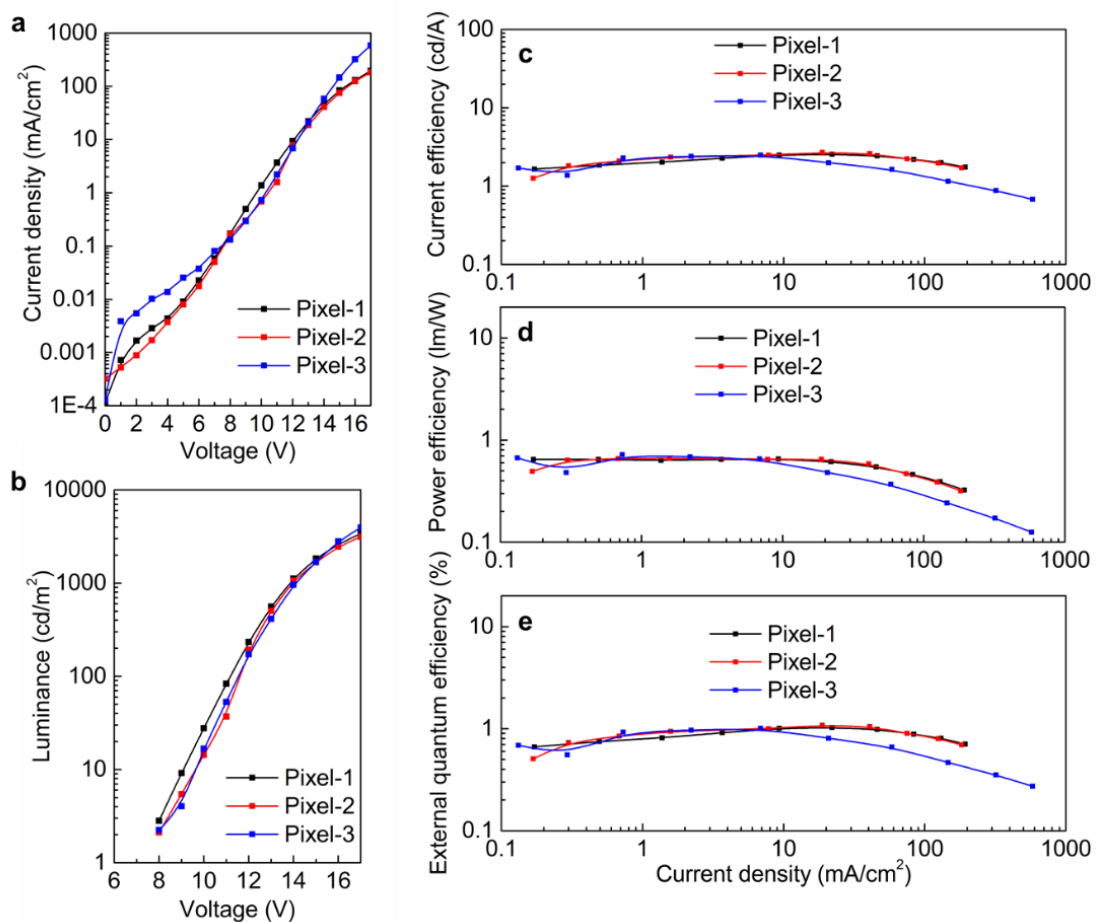


Figure 2.23. EL characterizations of LC device. (a) Current density vs. voltage plots, (b) luminance vs. voltage plots, (c) current density efficiency, (d) power efficiency, (e) external quantum efficiency plots. Multilayered OLED device structure: ITO/PEDOT:PSS (40 nm)/LC (25 nm)/CzDBA (40 nm)/TmPyPB (45 nm)/Liq (1nm)/Al (100 nm).#

Collected by Dr. Guohua Xie (Wuhan University).

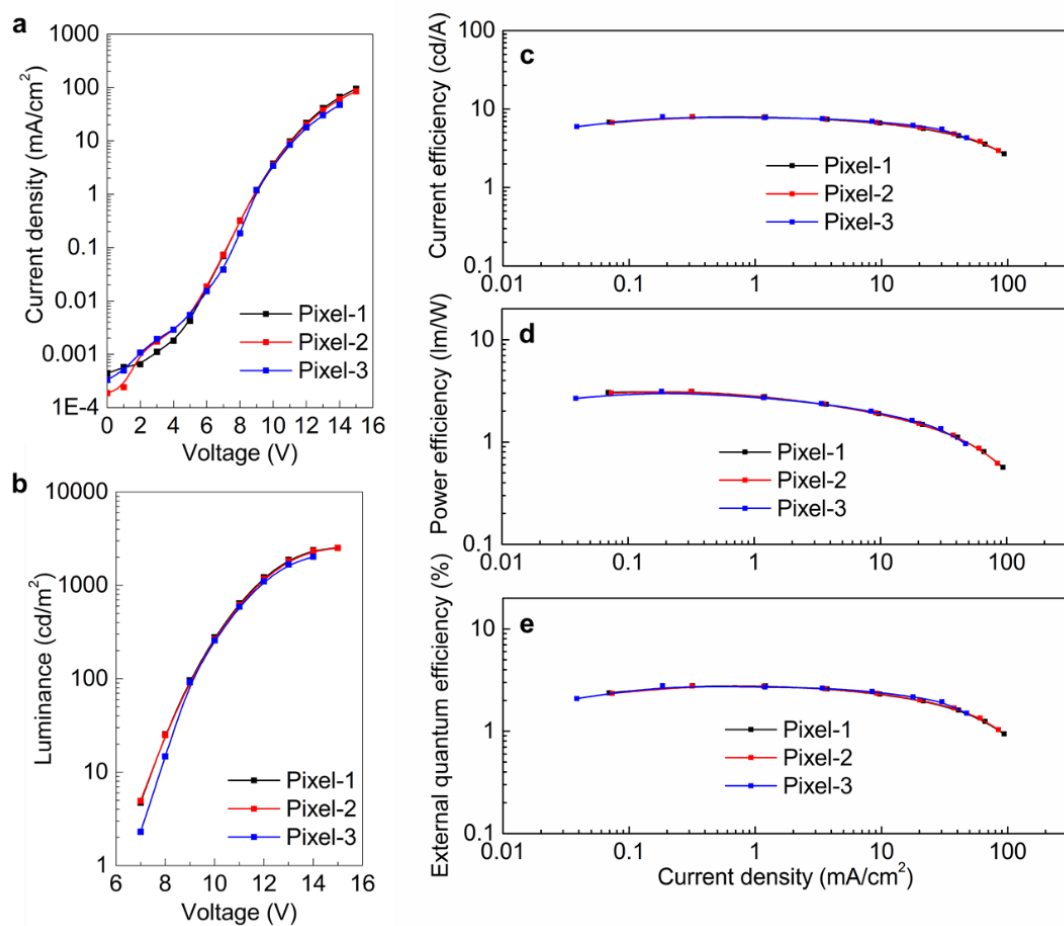


Figure 2.24. EL characterizations of **Brush I** device. (a) Current density vs. voltage plots, (b) luminance vs. voltage plots, (c) current density efficiency, (d) power efficiency, (e) external quantum efficiency plots. Multilayered OLED device structure: ITO/PEDOT:PSS (40 nm)/**Brush I** (25 nm)/CzDBA (40 nm)/TmPyPB (45 nm)/Liq (1nm)/Al (100 nm).#

Collected by Dr. Guohua Xie (Wuhan University).

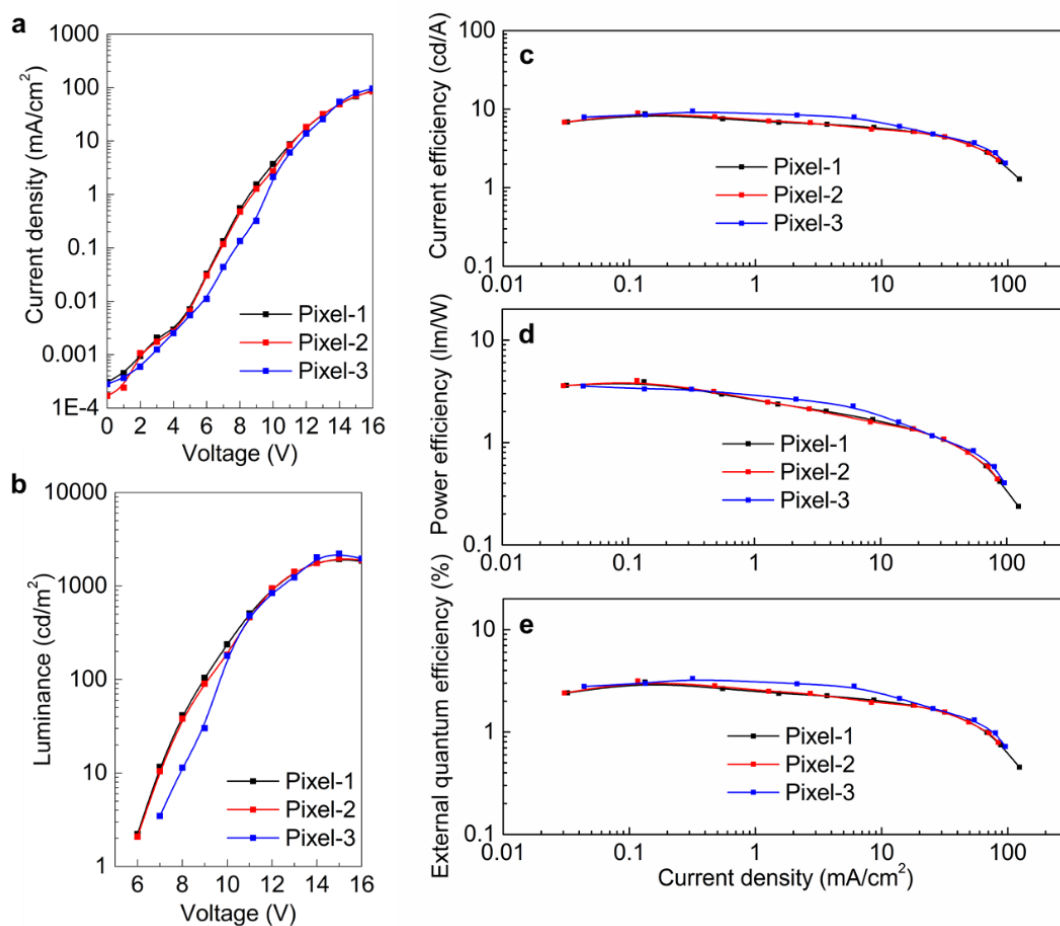


Figure 2.25. EL characterizations of **Brush III** device. (a) Current density vs. voltage plots, (b) luminance vs. voltage plots, (c) current density efficiency, (d) power efficiency, (e) external quantum efficiency plots. Multilayered OLED device structure: ITO/PEDOT:PSS (40 nm)/**Brush III** (25 nm)/CzDBA (40 nm)/TmPyPB (45 nm)/Liq (1nm)/Al (100 nm).#

Collected by Dr. Guohua Xie (Wuhan University).

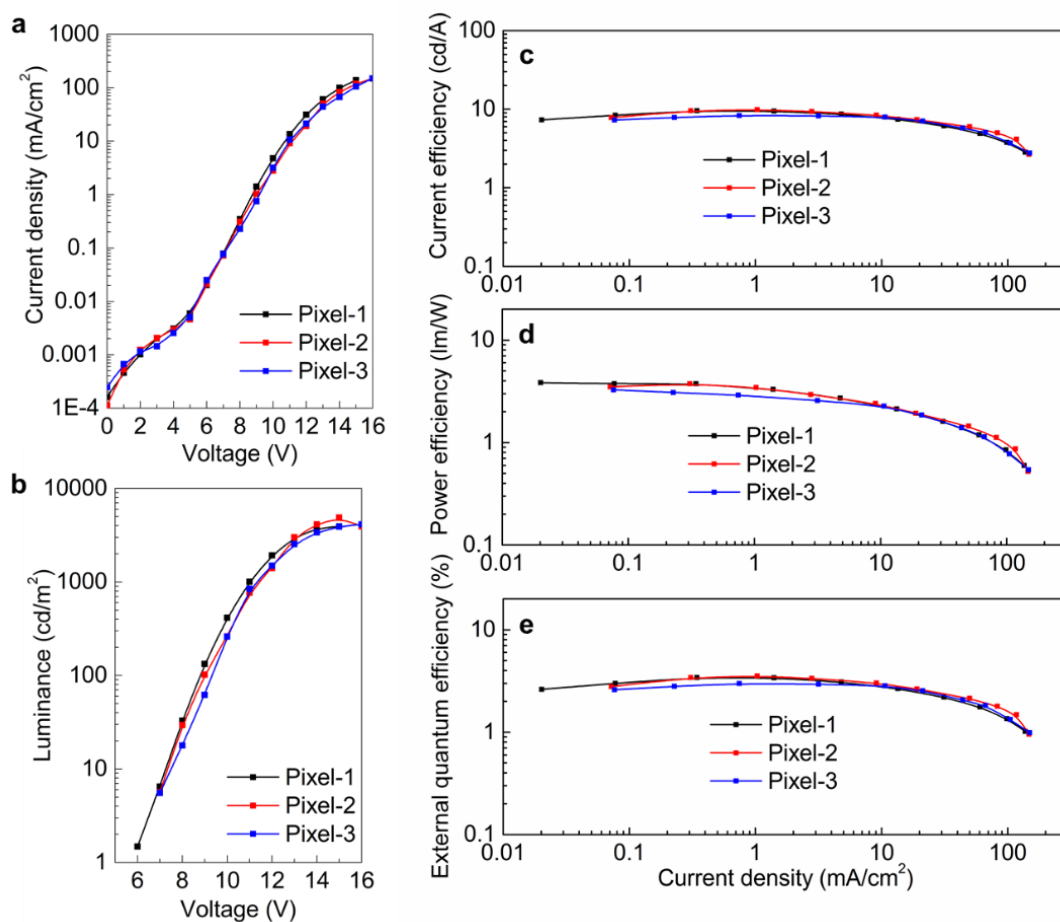


Figure 2.26. EL characterizations of **Brush V** device. (a) Current density vs. voltage plots, (b) luminance vs. voltage plots, (c) current density efficiency, (d) power efficiency, (e) external quantum efficiency plots. Multilayered OLED device structure: ITO/PEDOT:PSS (40 nm)/**Brush V** (25 nm)/CzDBA (40 nm)/TmPyPB (45 nm)/Liq (1nm)/Al (100 nm).#

The electroluminescence spectra of all TADF-OLED devices showed yellow-green emissions with peaks of maximum intensity in the range of 558-574 nm (Figure 2.27a), which ensured direct comparisons between device performances. Our hole mobility testing on **LC** and **Brush III**, as well as literature reports,⁷⁹⁻⁸⁰ indicated that the

Collected by Dr. Guohua Xie (Wuhan University).

polyvinyl polymers bearing pendant TPA functionalities, particularly in HTLs with FTs < 50 nm, could not provide hole mobility over $10^{-5} \text{ cm}^2\text{V}^{-1}\text{s}^{-1}$, which was at least two magnitudes lower than TFB ($2 \times 10^{-3} \text{ cm}^2\text{V}^{-1}\text{s}^{-1}$). Therefore, the current densities of devices **I**, **III**, **V**, and **LC** were consistently lower than device **TFB** within the whole range of bias, regardless of the TPA packing mode variations within HTLs (Figure 2.27b). The turn-on voltages, defined as the bias that enabled the current density of 0.01 mA/cm^2 , of **I**, **III**, **V**, and **LC** were also $\sim 2 \text{ V}$ higher than **TFB**.

However, the luminance of devices did not follow the observed current density trend. Starting from 6 V which produced meaningful device luminance ($\geq 2 \text{ cd/m}^2$), **III** with the highest anisotropic packing of TPAs exhibited comparable luminance values as **TFB** at each of the surveyed driving voltage until 9 V (Figure 2.27c, blue vs. orange profile), despite the obvious difference between intrinsic hole mobilities. Within the bias range from 10 to 14 V, **III** showed better luminance performance than **TFB**. Further increase of driving voltage of **III** over 14 V caused more perceptible luminance decrease than **TFB**, which indicated that TADF-OLED **III** was more “sensitive” to singlet-triplet and triplet-triplet annihilation at high current density.⁸¹ For devices **I** and **V** with relatively-lower extents of anisotropic TPA packings than **III**, their luminance performance at driving voltage ranged from 6 to 10 V (Figure 2.27c, green and red profiles for **I** and **V**, respectively) were subsidiary than **III** and **TFB**. However, upon applying bias exceeding 10 V, **I** and **V** produced enhanced luminance than both **III** and **TFB**. Particularly, device **V** build-up from **Brush V** with the largest amount of TPA charge carriers per polymer achieved the highest maximum luminance of 4880 cd/m^2 (Table 2.7),

which was ~95%, ~150%, ~110% enhancement than the device **I**, **III**, and **TFB**, respectively. By comparison, device **LC** with isotropic HTL continuously showed the lowest luminance at each of the surveyed driving voltage until 15 V (Figure 2.27c, black profile). As a note, linear PVTPA₅₀-based HTL enabled an improved “tolerance” to the undesirable singlet-triplet and triplet-triplet annihilation at high current densities (> 100 mA/cm² in this study), which produced maximum luminance of 3400 cd/m², ~70% of **V**, at 17 V of bias. Herein, anisotropic packing of TPAs within HTLs of green TADF-OLEDs revealed superiority on improving device luminance performance within the operating voltage range from 6 to 15 V. The higher extent of TPA “face-on” packing in device **III** afforded better luminance at relatively-lower driving voltages (6–9 V), while device **V** with moderate HTL anisotropy but bearing more TPA functionalities covered the 10–15 V “window” and provided the largest maximum luminance at 15 V.

As shown in Figure 2.27d, the external quantum efficiencies (EQEs) of devices **I**, **III**, and **V** with anisotropic HTLs exhibited significant enhancements over devices **LC** and **TFB** with isotropic HTLs at current densities less than 10 mA/cm². The maximum EQE of **I**, **III**, and **V** was 2.77%, 3.07%, and 3.53%, respectively, which were at least 1.6-fold higher than **LC** (1.03 %) and 2.3-fold higher than **TFB** (0.83 %), respectively. With the increment of current density to 30 mA/cm², the EQE of **III** (~1.57) underwent a ~50% of decrease from the maximum EQE value, while **I** (EQE ≈ 1.79) and **V** (EQE ≈ 2.39) endured ~35% and ~32% of decrease, respectively. However, even after experiencing such noticeable efficiency roll-off, devices **I**, **III**, and **V** with anisotropic HTLs still maintained over 50% enhanced EQEs than device **LC** with isotropic HTL and device **TFB**

with high HT mobility (EQE \approx 1.00% and 0.82% for **LC** and **TFB**, respectively) at same current density. A similar tendency was observed for the device power efficiency (PE) and current efficiency (CE) evaluations (Figures 2.27e and 2.27f, respectively), in which the maximum PE and CE of **I**, **III**, and **V** comprising anisotropic HTLs constructed from corresponding HTBs revealed over 380% and 210% of improvements, respectively, in comparison with **LC** and **TFB** (Table 2.7). The overall efficiencies of **V** exceeded all other devices in terms of the highest maximum EQE and CE (9.86 cd/A), as well as the secondarily-highest maximum PE (3.75 lw/W). As a note, the maximum luminance and efficiencies of device **V** were not competitive to the literature reported CzDBA-based green TADF-OLED with cascade HTL bearing inherently-higher hole mobility and an advanced host-dopant emissive layer.⁷⁸ These established tactics will be incorporated in our future design and investigation of HTBs for solution processable anisotropic HTLs that can realize the high electric electroluminescent performance of the OLED devices at the more practical applied voltages (< 6V).

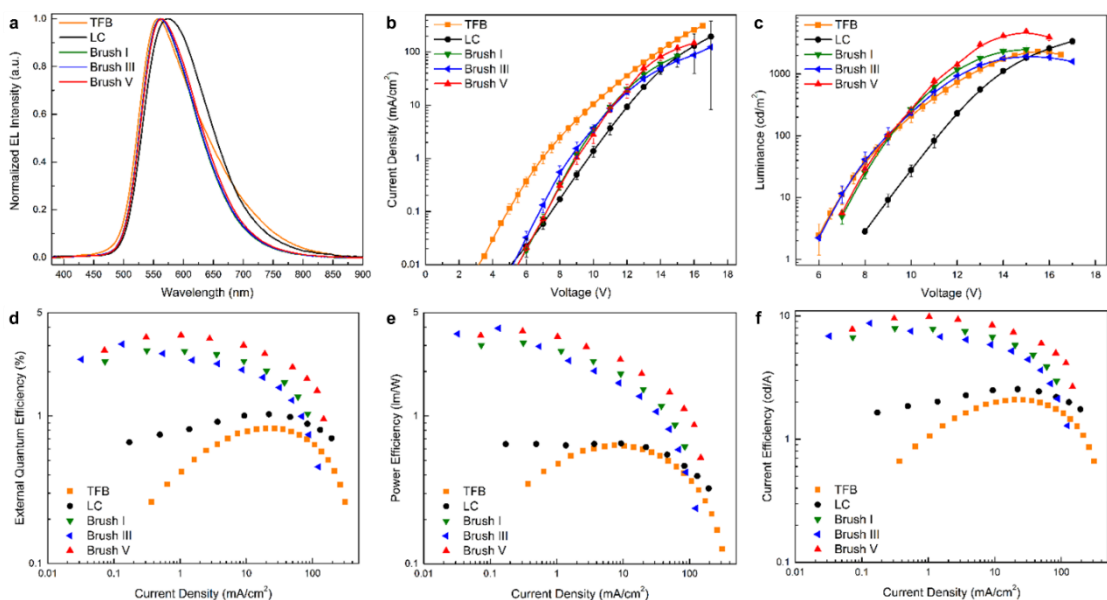


Figure 2.27. Performance evaluations of green OLED full devices comprising **Brush I**, **III**, and **V**, and **LC** and **TFB**, respectively, as HTLs. (a) Normalized electroluminescence spectra of devices. (b–c) Current density (b) and luminance (c) vs. voltage plots, respectively. (d–f) External quantum efficiency (d), power efficiency (e), and current efficiency (f) vs. current density plots, respectively.[#]

Table 2.7. Summary of green TADF-OLED characteristics.

| Device | L_{\max}^a (cd/m ²) | EQE_{\max}^b (%) | PE_{\max}^c (lm/W) | CE_{\max}^d (cd/A) |
|------------|-----------------------------------|---------------------------|-----------------------------|-----------------------------|
| TFB | 2310 ^e | 0.83 | 0.64 | 2.09 |
| LC | 3400 ^f | 1.03 | 0.65 | 2.55 |
| I | 2510 | 2.77 | 3.16 | 7.93 |
| III | 1940 | 3.07 | 3.92 | 8.73 |
| V | 4880 | 3.53 | 3.75 | 9.86 |

^aMaximum luminance at the bias of 15 V. ^bMaximum external quantum efficiency. ^cMaximum power efficiency. ^dMaximum current efficiency. ^eAt bias of 15.5 V. ^fAt bias of 17 V.

[#] Collected by Dr. Guohua Xie (Wuhan University).

2.3 Conclusion

In conclusion, P(NB-*g*-(PVTPA-*b*-PNFHB))-*b*-P(NB-*g*-PVTPA) bottlebrush polymers with precisely-controllable compositions and dimensions were synthesized by ROMP of well-defined macromonomers. The resulting HTBs could be vertically aligned on substrates to afford monolayered HTL thin films. The vertical alignment of the brush backbone assisted the preferential “face-on” molecular orientations of TPA units, demonstrated by the high order parameter from VASE quantifications. Green TADF-OLED device comprising HTBs as anisotropic HTLs indicated significant improvements on both electric and electroluminescent device performance, in comparison with the isotropic counterpart. Moreover, although the intrinsic hole mobilities of HTB-based HTLs were at least three magnitudes lower than the TFB-based control, the higher extent of TPA anisotropic packing could be beneficial to compensate the charge imbalance in OLED device, which resulted in comparable luminance and over 2-folds of efficiencies enhancements, respectively, at relatively-lower driving voltages (< 10 V). Our contemporary approach relying upon the chemistry toolbox revealed promising potentials for resolving the long-lasting obstacle in optoelectronics. It is also expected that this platform could be extended to vertically-alignable multiblock structures⁸² capable of multiple tasks of an ETL, an emissive layer, and an HTL through a single-stage fabrication for the construction of multiple-layered OLED devices.

2.4 Experimental Section

2.4.1 Materials

Grubbs' third-generation catalyst (G3),⁸³ 4-vinyl triphenylamine (VTPA),⁸⁴ and 3,3,4,4,5,5,6,6,6-nonafluorohexyl-*p*-benzyloxy styrene (NFHBS)⁸⁵ were synthesized according to literature reports. Other chemicals and reagents were purchased from Sigma-Aldrich, Acros, or VWR, and were used without further purification, unless otherwise noted. The poly(3,4-ethylene dioxythiophene):polystyrene sulfonate (PEDOT:PSS) solution was provided by the Dow Chemical Company. Prior to use, tetrahydrofuran (THF) and dichloromethane (CH₂Cl₂) were purified by passing through a solvent purification system (JC Meyer Solvent Systems). Column chromatography was performed on a CombiFlash Rf4x (Teledyne ISCO) with RediSep Rf columns (Teledyne ISCO). All materials used for hole-only devices and OLED devices fabrication were received from commercial sources.

2.4.2 Instrumentation and Characterization

Column chromatography was performed on a CombiFlash Rf4x (Teledyne ISCO) with RediSep Rf columns (Teledyne ISCO).

¹H and ¹³C NMR spectra were recorded on a Varian 500 spectrometer, interfaced to a LINUX computer using VNMR-J software, or a Bruker AVANCE NEO 400 spectrometer interfaced to Linux Centos 7 using Topspin 4.5.5 software. Chemical shifts were defined based on the solvent proton resonance.

Fourier-transform infrared (FTIR) spectra were recorded on an IR Prestige 21 system (Shimadzu Corp., Japan) equipped with an Attenuated Total Reflection (ATR) accessory, and analyzed by using IRsolution v.1.40 software.

Atmospheric pressure chemical ionization mass spectrometry (APCI-MS) experiments were performed using a Thermo Scientific LCQ-DECA instrument. The sample was directly infused at a flow rate of 6 $\mu\text{L}/\text{min}$. The spray voltage was set to -4.5 kV, and the sheath gas and auxiliary gas flow rates were set to 50 and 10 arbitrary units, respectively. The capillary transfer temperature was held at 250 $^{\circ}\text{C}$. Xcalibur 2.0 software was used for data acquisition and processing.

The CHN triplicate elemental analysis of NB-CTA (**3**) was performed at Midwest Microlab, LLC (Indianapolis, IN).

The polymer molar mass was calculated by ^1H NMR spectroscopy, and the molar mass and dispersity (D) were determined and confirmed by size exclusion chromatography (SEC). The SEC was conducted on a Waters 1515 HPLC (Waters Chromatography, Inc.) equipped with a Wyatt Optilab T-rEX differential refractometer (660 nm light source, Wyatt Technology Corp.), a Wyatt DAWN HELEOS II multi-angle light scattering (MALS) detector (658 nm light source, Wyatt Technology Corp.), and a three-column-series (Phenogel 5 μm Linear (2), 100 \AA , and 10⁴ \AA , 300 \times 4.6 mm columns; Phenomenex, Inc.). The system was equilibrated at 40 $^{\circ}\text{C}$ in THF, which served as the polymer solvent and eluent with a flow rate of 0.35 mL/min. Polymer solutions were prepared at known concentrations (3-5 mg/mL), and an injection volume of 200 μL was used. Data collection and analysis were performed with ASTRA software (Wyatt

Technology Corp.). The dn/dc values of the analyzed polymers were determined from the differential refractometer response.

The THF-SEC of **M1** and **M6** were conducted on a Waters Chromatography, Inc. (Milford, MA) system equipped with an isocratic pump model 1515, a differential refractometer model 2414, and a three-column series PL gel 5 μ m Mixed C, 500 Å, and 10⁴ Å, 300 \times 7.5 mm columns (Polymer Laboratories, Inc.). The system was equilibrated at 40 °C in THF, which served as a polymer solvent and eluent (flow rate set to 1.00 mL/min).

The system for SEC of **Brush II** (Figure 2.4) was performed in chloroform (CHCl₃) at room temperature using a JAI recycling preparative HPLC (LC-92XXII NEXT SERIES).

The glass transition temperatures (T_g s) were measured by differential scanning calorimetry (DSC) on a Mettler-Toledo DSC3/700/1190 (Mettler-Toledo, Inc.), with a heating rate of 10 °C/min under N₂ atmosphere. Thermogravimetric analysis (TGA) was performed under argon (Ar) atmosphere using a Mettler-Toledo TGA2/1100/464, with a heating rate of 5 °C/min. Both measurements were analyzed by using STAR^e version 15.00a software (Mettler-Toledo, Inc.).

Atomic force microscopy (AFM) imaging was performed on an Asylum MFP-3D system (Oxford Instruments, Plc.) in tapping mode using standard silicon tips (T190-25, VISTAprbes; spring constant: 48 N/m, tip radius: ~10 nm, resonance constant: 190 kHz).

Ultraviolet-visible (UV-vis) absorption spectroscopy was performed on a Shimadzu UV-2550 spectrophotometer at the range from 200 nm to 800 nm with quartz cuvettes.

Steady-state fluorescence spectra were collected using an RF-5301PC spectrofluorometer (Shimadzu Corp.). The excitation wavelength for emission measurements was chosen as 660 nm, which is the same wavelength of the light source of the Wyatt Optilab T-rEX differential refractometer. An emission wavelength of 800 nm was used for excitation measurements. Polymer solutions for fluorescence measurements were prepared at 0.1 mg/mL in THF, CHCl₃, and CH₂Cl₂.

Cyclic voltammetry was performed on a Gamry Instruments Interface 1000 potentiostat with a Ag/AgCl reference electrode, platinum wire counter electrode, and glassy carbon working electrode. The electrochemical properties were investigated in a dichloromethane solution with 0.1 M tetrabutylammonium hexafluorophosphate as the electrolyte.

Secondary ion mass spectrometry (SIMS) measurements were conducted on a custom-built massive cluster secondary ion mass spectrometer.⁸⁶ A gold liquid metal ion source and a Wien filter were used to generate a beam of mass selected Au₄₀₀⁴⁺ projectiles.⁸⁷ The liquid metal ion source and Wien filter were installed on a 100-kV platform. The projectiles pulsed to a rate of approximately 1000 projectiles per second, ensuring each projectile was separated in time and space. Upon impacting the surface, biased to -10 kV, each 520 keV Au₄₀₀⁴⁺ projectile caused the emission of electrons, secondary ions, and neutral atoms/molecules. The electrons were deviated by a weak

magnetic field and collected on a microchannel plate-based detector. These electrons acted as the start of the time-of-flight mass spectrometry (TOF-MS) measurement. The negative secondary ions were accelerated toward the reflectron TOF-MS and collected by an eight-anode microchannel plate-based detector. The suite of start (electrons) and stop signals (secondary ions) were collected by a time-to-digital converter (TDCV4 Institute of nuclear physics, Orsay, France) operating in the event-by-event mode. Mass spectra were collected and recorded before the subsequent projectile impact, termed the event-by-event bombardment/detection mode. Each sample was analyzed in three locations (125 μm radius) with 2×10^6 to 4×10^6 projectiles.

The thin film depth profiles of SIMS were obtained using a CAMECA 4F secondary ion mass spectrometer (CAMECA Instruments, Inc.). Before the measurement, the polymer films from **Brush I**, **II**, and **IV** were coated with a thin layer of Pt/Pd alloy (80 wt%/20 wt%). The analyzed surface was sputtered by the 14.5 keV Cs^+ beam at a current of 10 nA (**Brush I** films with 2.5 nm of Pt/Pd coating), 8 nA (**Brush II** films with 5 nm of Pt/Pd coating), 12 nA (**Brush III** and **Brush V** films without Pt/Pd coating), and 14 nA (**Brush IV** films with 5 nm of Pt/Pd coating), respectively. The diameter of the beam was 2 μm , and the raster was $500 \times 500 \mu\text{m}^2$. The angle of incidence of the beam was 26° , and the sputtering rates were calculated by SRIM 2011.08 software. The fluorine depth profiles were expressed by using the ratio of intensities between F^- and C^- ions. The usage of the ratio and the calculation methods were based upon a previous report.¹⁹

The anisotropy data were obtained by variable angle spectral ellipsometry (VASE), using an M-2000D ellipsometer (J. A. Woollam Co., Inc.). Measurements were

conducted over a 0.5 cm × 0.5 cm or 1 cm × 1 cm film area (3 × 3 points) at multiple angles (45°, 50°, 55°, 60°, 65°, 70°) with a wavelength range of 190–1000 nm. Using Complete EASE™ software, the ellipsometry data were modeled progressively *via* the Cauchy model to B-Spline, and to the Gen-Osc model for both film thickness and optical properties (n_o , n_e : refractive index; k_o , k_e : extinction coefficient; subscript o and e refer to ordinary and extraordinary, respectively). These values were averaged over the analyzed areas. The Order Parameter, S , was calculated using equation (1), where k_o^{max} and k_e^{max} are the maximum over the wavelength range of 240–420 nm (corresponding to the triphenylamine (TPA) absorption peak):

$$S = \frac{k_e^{max} - k_o^{max}}{k_e^{max} - 2k_o^{max}} \quad (1)$$

when $S = 0$, the molecular packing is isotropic; when $S = -0.5$, the molecular packing is anisotropic with TPA moieties aligned parallel to the substrate.

The grazing-incidence small-angle X-ray scattering (GISAXS) experiments were performed at Beamline 8-ID-E of the Advanced Photon Source, Argonne National Laboratory ($\lambda = 1.6868 \text{ \AA}$).⁸⁸ Scattering data were acquired at an incident angle of 0.14°. Using the GIXSGUI package⁸⁹ from Matlab (Mathworks), data were corrected for X-ray polarization, detector sensitivity, and geometrical solid-angle. A line cut along the out-of-plane direction was used to present scattering data as a function of the out-of-plane scattering vector, q_z .

The grazing-incidence wide-angle X-ray scattering (GIWAXS) measurements were performed at the Advanced Photon Source's DuPont-Northwestern-Dow

Collaborative Access Team (DND-CAT) 5-BM-C beamline, part of Argonne National Laboratory. X-rays originated from a bending magnet source and were monochromated (20 keV, $\lambda = 0.62 \text{ \AA}$) using a Si (111) double-crystal monochromator resulting in roughly 10^7 photons/s flux. The beam was cut using slits to 40- μm by 500- μm and additional slits following the ion chamber were used to remove parasitic scattering. The incident angle was scanned about the critical angle for poly(methyl methacrylate) ($\alpha_c = 0.068^\circ$) in 0.005° increments to find a maximum scattering intensity. A MAR165 CCD (2048 x 2048 pixels) area detector was placed ~ 180 mm away from the sample. Data were collected using 600-s exposures. LaB_6 was used to calibrate the 2D area detector: beam center position, sample-to-detector distance, and detector tilting angles. The 1D profile [$I(q)$ vs q] was generated by circularly averaging the diffraction pattern on the 2D images over the 180 degrees of available detector area using Fit2d software.

Density functional theory (DFT) was used to calculate the highest occupied molecular orbital (HOMO) and lowest unoccupied molecular orbital (LUMO) energy levels of isolated molecules in the ground state (Figure 2.19), which represent fragments of the overall bottlebrush polymer design. Within the realm of DFT, the standard hybrid functional (B3LYP)⁹⁰⁻⁹² with the 6-31G* basis set⁹³⁻⁹⁵ was used for all the calculations with the Gaussian09 program.⁹⁶

The hole mobility tests were conducted on a Keithley 6517B electrometer (Tektronix Inc.). The hole mobilities were measured by the space charge limited current (SCLC) method on hole-only devices (HODs), and SCLC mobility (μ) was calculated according to equation (2):

$$\ln\left(\frac{I}{V^2}\right) = 0.89\beta\left(\frac{V}{L}\right)^{1/2} + \ln\left(\frac{9\varepsilon\varepsilon_0\mu S}{8L^3}\right) \quad (2)$$

Where I is the current, V is the potential, β is the field activation factor, L is the film thickness, ε is the relative permittivity, ε_0 is the permittivity of free charge, and S is the area of the device. Three valuable data sets were picked from raw hole mobility test data and plotted using Origin software (OriginLab Corp.).

The electroluminescence (EL) properties of OLED devices were measured in ambient air after encapsulation by a PR735 SpectraScan Spectroradiometer (Photo Research) combined with a Keithley 2400 SourceMeter unit. The instrument was controlled with customized software to simultaneously determine the current-voltage-luminous intensity characteristics and the EL spectra.

2.4.3 Synthesis and Film Preparation

Preparation of *Exo*-5-norbornene-2-methoxymethyl phenyl methanol (NB-StOH (1), Scheme 2.1). To a flame-dried 100 mL round-bottom flask equipped with a magnetic stir bar was added *exo*-5-norbornene-2-methanol⁸³ (1.00 g, 8.05 mmol) and 20 mL of anhydrous *N,N*-dimethylformamide. The solution was cooled to 0 °C before the portion-wise addition of sodium hydride (600 mg, 25.0 mmol). The solution was allowed to warm to room temperature (r.t.) and stirred at r.t. for 30 min. The solution was then cooled to 0 °C before the slow addition of styrene oxide (966 mg, 8.04 mmol). The mixture was stirred at r.t. for 48 h before quenching by the dropwise addition of 20 mL of 1 M hydrochloric acid. The mixture was extracted with diethyl ether (3 × 50 mL) and the

combined organics were washed with saturated aqueous sodium bicarbonate solution and water, dried over magnesium sulfate, and concentrated under reduced pressure. The product **2** was isolated by column chromatography (2:1 pentane/diethyl ether, *v/v*), yielding a colorless liquid (760 mg, 39% yield). ¹H NMR (400 MHz, CDCl₃) δ 7.42–7.30 (5H, m, ArH), 6.15–6.04 (2H, m, CH=CH from NB), 4.95–4.87 (1H, m, CH₂(Ar(CH))OH), 3.66–3.53 (2H, m, CH₂OCH₂CH), 3.48–3.37 (2H, m, CH₂OCH₂CH), 2.82 (1H, m, NB allylic H), 2.75 (1H, m, NB allylic H), 2.20–1.79 (1H, br s, OH), 1.78–1.67 (1H, m, (CH(CH)CH₂)CH₂ from NB), 1.39–1.06 (4H, m, CHCH₂CH bridgehead and CHCH₂CH from NB) ppm. ¹³C NMR (101 MHz, CDCl₃) δ 140.4, 136.7, 128.5, 127.9, 126.3, 76.2, 75.2, 72.8, 45.2, 43.8, 41.7, 38.9, 29.8 ppm. FT-IR (ATR): 3604–3118, 3090–3010, 3005–2820, 1714, 1450, 1273, 1175, 1098, 1061, 1022, 907, 840, 754, 700 cm⁻¹.

Preparation of Exo-5-norbornene-2-methoxymethyl phenylmethanesulfonate (NB-StOMs (2), Scheme 2.1). To a flame-dried 25 mL round-bottom flask equipped with a magnetic stir bar was added **1** (300 mg, 1.23 mmol) and 3 mL of anhydrous CH₂Cl₂. The resulting solution was then cooled to 0 °C before the addition of triethylamine (249 mg, 2.46 mmol), followed by the dropwise addition of methanesulfonyl chloride (MsCl) (169 mg, 1.47 mmol). The solution was allowed to stir at 0 °C for 1 h, upon which 10 mL of saturated aqueous NH₄Cl solution was added. The mixture was extracted with diethyl ether (3 × 20 mL) and the combined organics were washed with water and brine, before drying over magnesium sulfate. The solvent was removed under reduced pressure. Product **2** was obtained as a colorless oil without further purification (396 mg, *ca.* quantitative yield). ¹H NMR (400 MHz, CDCl₃) δ 7.46–7.31 (5H, m, ArH), 6.15–6.02

(2H, m, $\text{CH}=\text{CH}$ from NB), 4.95–4.81 ($\text{CH}_2(\text{Ar}(\text{CH}))\text{O}$), 3.94–3.76 (2H, m, $\text{CH}_2\text{OCH}_2\text{CH}$), 3.75–3.60 (1H, m, NBCH_2O), 3.40–3.28 (1H, m, NBCH_2O), 3.09 (3H, s,), 2.82 (1H, m), 2.75 (1H, m), 1.71–1.64 (1H, m, $(\text{CH}(\text{CH})\text{CH}_2)\text{CH}_2$ from NB), 1.40–1.04 (4H, m, CHCH_2CH bridgehead and CHCH_2CH from NB) ppm. ^{13}C NMR (101 MHz, CDCl_3) δ 136.9, 135.8, 129.0, 127.0, 126.9, 83.3, 75.4, 73.8, 45.2, 43.8, 41.7, 39.0, 38.8, 29.8. FT-IR (ATR): 3070–3005, 3000–2824, 1721, 1452, 1348, 1277, 1169, 1121, 966, 912, 868, 812, 750, 700 cm^{-1} .

Synthesis of Exo-5-norbornene-2-methoxymethyl phenylmethyl Ethyl carbonotrithioate (NB-CTA (3), Scheme 2.1). To a flame-dried 25 mL round-bottom flask equipped with a magnetic stir bar was added K_3PO_4 (261 mg, 1.23 mmol) and 3.5 mL of acetone. To the suspension was added ethanethiol (92.0 mg, 1.50 mmol), and the mixture was allowed to stir at r.t for 1 h before the addition of carbon disulfide (CS_2) (281 mg, 3.69 mmol). The resulting bright yellow suspension was allowed to stir at r.t. for an additional 1 h before the addition of **2** (396 mg, 1.23 mmol). The suspension was stirred for 4 h in the dark at r.t., before dilution with 20 mL of acetone. The solids were filtered over a celite pad and washed with 50 mL of acetone. The filtrate was concentrated under reduced pressure and purified by column chromatography (hexane), yielding **3** as a yellow oil (230 mg, 51% yield). ^1H NMR (400 MHz, CDCl_3) δ 7.41–7.27 (5H, m, ArH), 6.10–6.00 (2H, m, $\text{CH}=\text{CH}$ from NB), 5.56–5.49 (1H, m, $\text{CH}_2(\text{Ar}(\text{CH}))\text{S}$), 3.99–3.84 (2H, m, $\text{NBCH}_2\text{OCH}_2\text{CH}$), 3.58–3.47 (1H, m, NBCH_2O), 3.43–3.29 (1H, m, NBCH_2O , and 2H, m, SCH_2CH_3), 2.77 (1H, m, NB allylic H), 2.64 (1H, m, NB allylic H), 1.64 (1H, br m, $(\text{CH}(\text{CH})\text{CH}_2)\text{CH}_2$ from NB), 1.34 (3H, t, $J = 7.4$ Hz, SCH_2CH_3), 1.30–1.14, 1.06 (4H,

m, CHCH_2CH bridgehead and CHCH_2CH from NB) ppm (Figure 2.28a). ^{13}C NMR (101 MHz, CDCl_3) δ 222.6, 138.1, 136.6, 128.6, 128.5, 127.8, 75.8, 72.5, 54.2, 45.0, 43.6, 41.6, 38.7, 31.3, 29.5, 13.0 ppm (Figure 2.28b). FT-IR (ATR): 3055, 3000–2790, 1597, 1450, 1366, 1335, 1258, 1103, 1072, 1026, 864, 810, 702 cm^{-1} . HRMS (APCI) m/z: $[\text{M} + \text{H}]^+$ Calcd for $\text{C}_{19}\text{H}_{25}\text{OS}_3$ 365.1062; Found 365.1056, $[\text{M} - \text{H}]^-$ Calcd for $\text{C}_{19}\text{H}_{23}\text{OS}_3$ 363.0906; Found 363.0918. CHN triplicate analysis (calcd, found for $\text{C}_{19}\text{H}_{24}\text{OS}_3$): C (62.60, 62.97), H (6.64, 6.63), N (0.00, 0.00).

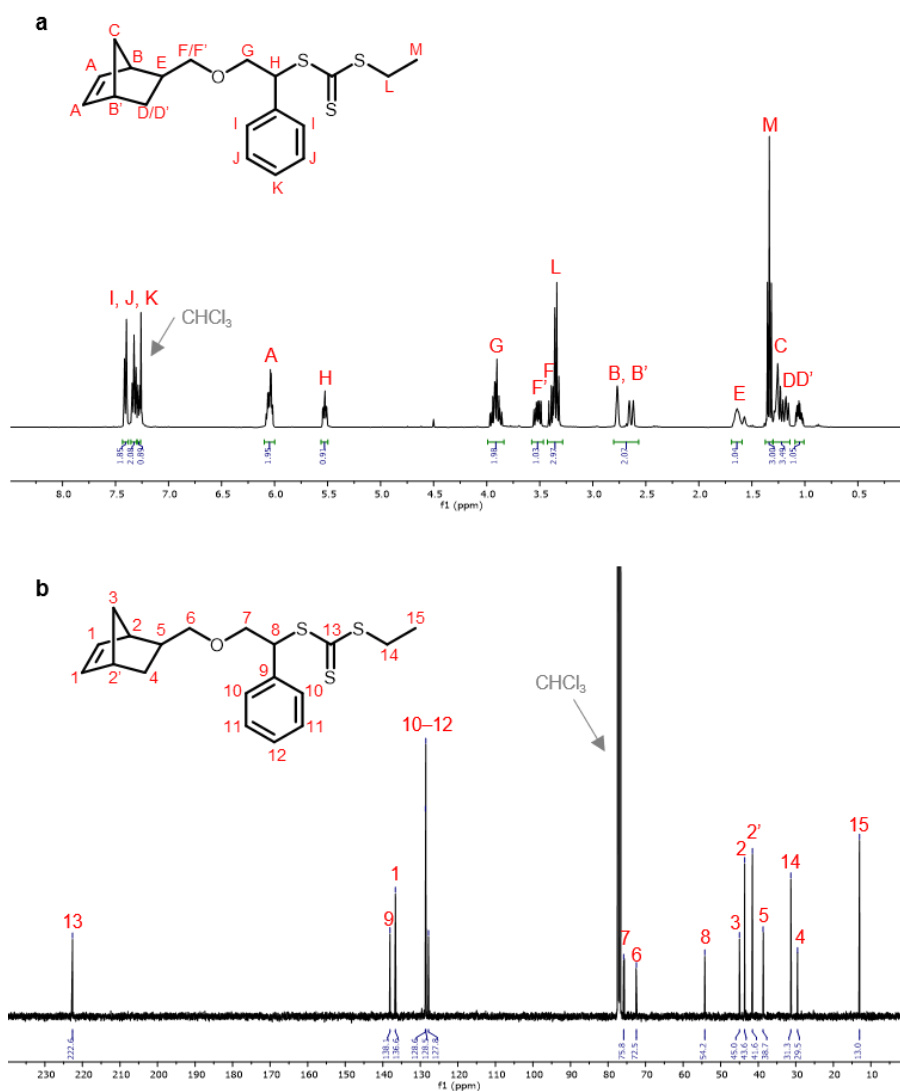


Figure 2.28. NMR spectra for NB-CTA. (a) ^1H NMR (400 MHz, CDCl_3) and (b) ^{13}C NMR (101 MHz, CDCl_3).

General Procedure for Synthesis of *Exo*-norbornene-poly(vinyl triphenylamine) (NB-PVTPA, M1–M5). To a flame-dried Schlenk flask equipped with a magnetic stir bar was added NB-CTA, VTPA, 2,2'-azobis(2-methylpropionitrile) (AIBN), and anhydrous 1,4-dioxane. The solution was deoxygenated through several cycles of freeze-pump-thaw, followed by back-filling with N_2 . After the last cycle, the

reaction mixture was stirred 10 min at r.t. and immersed into a pre-heated oil bath at 60–62 °C to start the polymerization. After predetermined times (Table 2.1), the polymerization was quenched by cooling the reaction flask with liquid N₂. The polymer was collected by precipitation into MeOH twice. The collected product was kept under vacuum overnight to remove residual solvent.

Detailed Procedure for Synthesis of Macromonomer 5 (M5), NB-PVTPA₃₉.

To a flame-dried 25 mL Schlenk flask equipped with a magnetic stir bar was added NB-CTA (54.3 mg, 0.149 mmol), VTPA (2.23 g, 8.23 mmol), AIBN (2.19 mg, 13.5 μmol), and 16.5 mL of 1,4-dioxane. The solution was deoxygenated through four cycles of freeze-pump-thaw, followed by back-filling with N₂. After the last cycle, the reaction mixture was stirred 10 min at r.t. and immersed into a pre-heated oil bath at 62 °C to start the polymerization. After 72 h, the polymerization was quenched by cooling the reaction flask with liquid N₂. The resulting mixture was diluted with 5 mL of THF and precipitated into 135 mL of MeOH. Centrifugation-collected precipitates were dissolved in 30 mL of THF and precipitated into 180 mL of MeOH. The solids were collected through centrifugation and kept under vacuum overnight to remove residual solvents, yielding a yellow powder (1.25 g, 93% yield based upon ~58 % monomer conversion). $M_{n, SEC} = 9,870$ Da (MALS detector), $D = 1.01$. ¹H NMR (500 MHz, CD₂Cl₂) δ 7.33–6.35 (br m, *ArH*s from NB-CTA and VTPA), 6.06–5.90 (br, NB *CH=CH*), 3.51–3.02 (br m, NB-CTA NB*CH*₂*OCH*₂R and *SCH*₂*CH*₃), 2.83–2.63 (br s, NB allylic *H*), 2.60–0.73 (br m, all *CH*₂s and *CH*s from VTPA unit backbone and NB ring, *SCH*₂*CH*₃) ppm (Figure 2.29a). ¹³C NMR (126 MHz, CD₂Cl₂) δ 175.8, 147.8, 145.5, 129.1, 123.8, 122.3, 40.2 ppm. FT-IR (ATR): 3120–2990, 2970–

2830, 1587, 1491, 1450, 1314, 1273, 1236, 1198, 1144, 1074, 1028, 826, 750 cm⁻¹. *T_g*: 140 °C. TGA: 300–376 °C, 11% mass loss, 376–434 °C, 73% mass loss, 19% mass remaining above 500 °C. **M1** (NB-PVTPA₁₀), **M2** (NB-PVTPA₂₂), **M3** (NB-PVTPA₂₆), and **M4** (NB-PVTPA₃₀) were synthesized analogously to **M5**.

General Procedure for Synthesis of *Exo*-norbornene-poly(vinyl triphenylamine)-*b*-poly(3,3,4,4,5,5,6,6,6-nonafluorohexyl-*p*-benzyloxy styrene) (NB-PVTPA-*b*-PNFHBS, M6–M7). To a flame-dried Schlenk flask equipped with a magnetic stir bar was added NB-PVTA, NPHBS, AIBN, and 1,4-dioxane. The solution was deoxygenated through several cycles of freeze-pump-thaw, followed by back-filling with N₂. After the last cycle, the reaction mixture was stirred 10 min at r.t. and immersed into a pre-heated oil bath at 60 °C to start the polymerization. After 20 h, the polymerization was quenched by cooling the reaction flask with liquid N₂. The polymer was collected by precipitation into MeOH twice. The collected product was kept under vacuum overnight to remove residual solvent.

Detailed Procedure for Synthesis of Macromonomer 6 (M6), NB-PVTPA₁₀-*b*-PNFHBS₁₃. To a flame-dried 25 mL Schlenk flask equipped with a magnetic stir bar, NB-PVTPA₁₀ (**M1**; 307 mg, 0.10 mmol), NPHBS (1.52 g, 4.00 mmol), AIBN (1.30 mg, 8.00 μmol), and 3 mL of 1,4-dioxane were added. After stirring at r.t. for 10 min, the resulting solution was deoxygenated through four cycles of freeze-pump-thaw, followed by back-filling with N₂. After the last cycle, the reaction mixture was stirred 10 min at r.t. and immersed into a pre-heated oil bath at 60 °C to start the polymerization. After 20 h, the polymerization was quenched by cooling the reaction flask with liquid N₂. The resulting

solution was diluted with 7 mL of THF and precipitated into 130 mL of MeOH. Centrifugation-collected precipitates were dissolved in 25 mL of THF and precipitated into 180 mL of MeOH. The solids were collected through centrifugation, washed with 100 mL of MeOH, and kept under vacuum overnight to remove residual solvents, yielding a yellow powder (513 mg, 83% yield based upon ~33 % monomer conversion). $M_{n, SEC} = 5,470$ Da (MALS detector), $D = 1.10$. $^1\text{H NMR}$ (500 MHz, CD_2Cl_2) δ 7.31–6.24 (br m, ArHs from VTPA units, NFHBS units and NB-CTA), 6.05–5.92 (br, NB CH=CH), 4.56–4.14 (br m, OCH₂CH from NB-CTA, NFHBS ArCH₂OCH₂CH₂C₄F₉), 3.85–3.54 (br s, NFHBS CH₂OCH₂CH₂C₄F₉), 3.51–3.07 (br m, NB-CTA NBCH₂OCH₂R, SCH₂CH₃), 2.80–2.66 (br s, NB allylic H), 2.60–0.73 (br m, all CH₂s and CHs from VTPA and NFHBS unit backbone, and NB ring, SCH₂CH₃) ppm (Figure 2.29b). $^{13}\text{C NMR}$ (126 MHz, CD_2Cl_2) δ 175.9, 147.8, 145.5, 136.5, 129.1, 127.5, 123.8, 122.3, 72.9, 62.0, 40.3, 31.3 ppm. FT-IR (ATR): 3130–2990, 2970–2820, 1587, 1491, 1314, 1273, 1236, 1200, 1144, 1076, 1028, 892, 826, 750 cm^{-1} . T_g : 115 °C. TGA: 250–342 °C, 10% mass loss, 342–412 °C, 67% mass loss, 23% mass remaining above 500 °C. **M7** (NB-PVTPA₂₂-*b*-PNFHBS₉) ($^1\text{H-NMR}$ analysis is shown in Figure 2.29c) was synthesized analogously to **M6**.

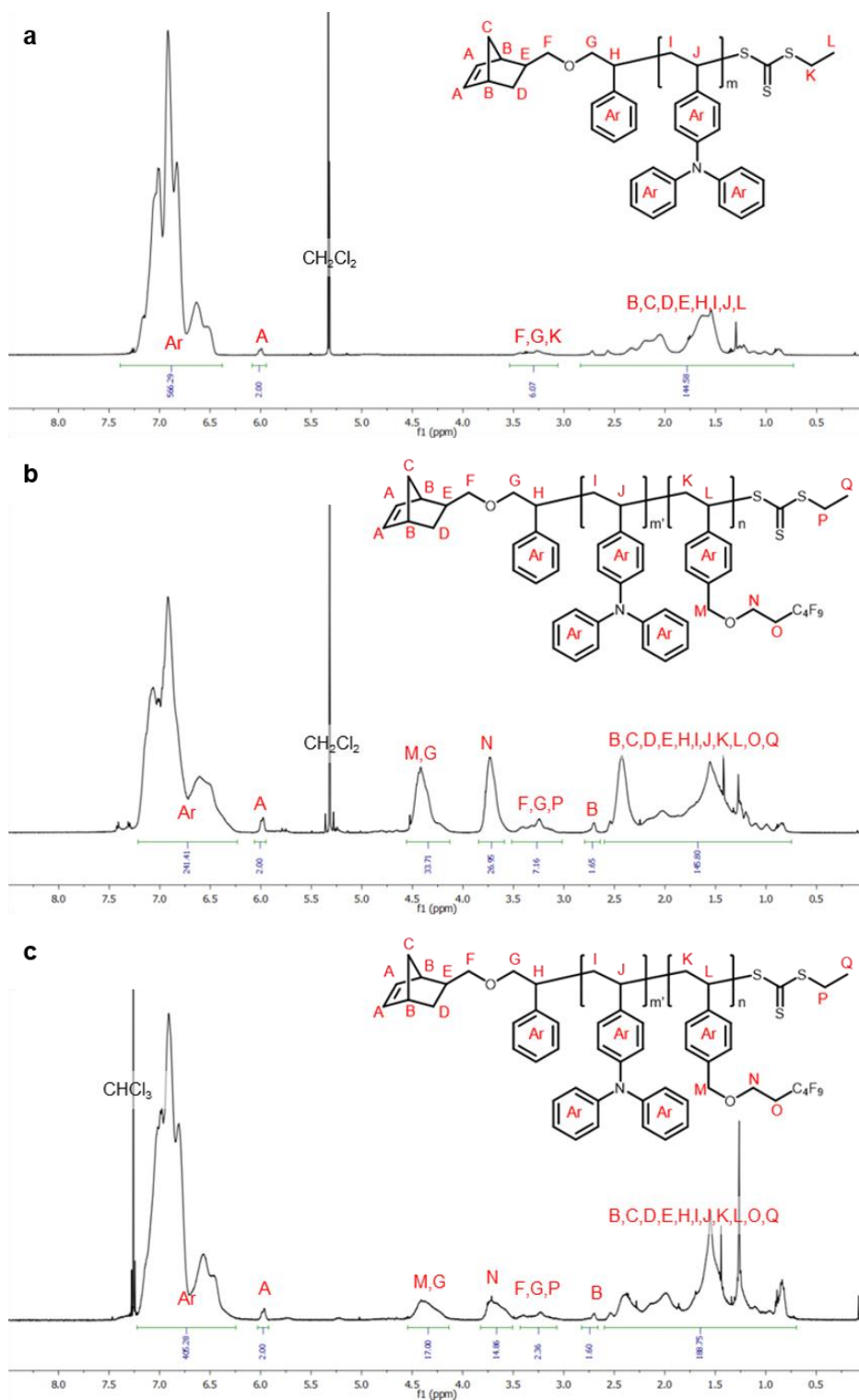


Figure 2.29. ¹H NMR spectra of (a) **M5** (500 MHz, CD₂Cl₂), (b) **M6** (500 MHz, CD₂Cl₂) and (c) **M7** (500 MHz, CDCl₃).

Synthesis of Brush III (1): Sequential Ring-Opening Metathesis Polymerization (ROMP) of M6 and M5 [ttc-Brush III]. To a flame-dried 10 mL Schlenk flask equipped with a magnetic stir bar was added modified G2 catalyst (0.91 mg, 1.3 μmol) and 0.4 mL of THF. The mixture was stirred 1 min at r.t. and deoxygenated through three cycles of freeze-pump-thaw. To a separate flame-dried vial was added a solution of **M6** (106 mg, 12.5 μmol) in 0.6 mL of THF and deoxygenated through three cycles of freeze-pump-thaw. **M6** solution was then added *via* an air-tight syringe, to the **G3** solution in the Schlenk flask. The reaction mixture was allowed to stir at r.t. for 1.5 h. To a separate flame-dried vial equipped with a rubber septum was added a solution of **M5** (411 mg, 37.4 μmol) in 3 mL of THF and deoxygenated through three cycles of freeze-pump-thaw. The solution was then transferred to the Schlenk flask with an air-tight syringe. The resulting reaction mixture was stirred at r.t. for 5.5 h before quenching the polymerization by the addition of 0.4 mL of THF/ethyl vinyl ether (EVE) ($v/v = 3:2$). The solution was stirred at r.t. for an additional 2 h, diluted with 4 mL of THF, and precipitated into 90 mL of MeOH. The centrifugation-collected precipitates were dissolved in 12 mL of THF and precipitated into 125 mL of MeOH. The product (**ttc-Brush III**) was collected through centrifugation, washed with 150 mL of MeOH twice, and kept under vacuum overnight to remove residual solvents, yielding a yellow powder (465 mg, 89% yield based upon >95% conversion for **M6** and ~93% conversion for **M5**). $M_{n, \text{SEC}} = 264$ kDa (MALS detector), $D = 1.20$. $^1\text{H NMR}$ (500 MHz, CD_2Cl_2) δ 7.31–6.20 (br m, ArH), 4.56–4.13 (br s, NFHBS ArCH₂OCH₂CH₂C₄F₉), 3.85–3.52 (br s, NFHBS ArCH₂OCH₂CH₂C₄F₉), 3.47–3.00 (br m, NB-CTA NBCH₂OCH₂R, SCH₂CH₃), 2.56–0.73 (br m, all CH₂s and CHs

from VTPA and NFHBS unit backbone, and NB ring, SCH₂CH₃) ppm. ¹³C NMR (126 MHz, CD₂Cl₂) δ 169.7, 147.8, 145.5, 129.1, 123.8, 122.3, 40.3, 31.3 ppm. FT-IR (ATR): 3120–2990, 2970–2820, 1587, 1487, 1312, 1271, 1177, 1074, 1028, 890, 826, 748 cm⁻¹. T_g: 140 °C. TGA: 300–368 °C, 10% mass loss, 368–430 °C, 66% mass loss, 24% mass remaining above 500 °C.

Synthesis of Brush III (2): RAFT Chain-End Removal. To a flame-dried 10 mL Schlenk flask equipped with a magnetic stir bar was added **ttc-Brush III** (200 mg, 20.6 μmol; calculated by the stoichiometry of RAFT chain-end groups), 1-ethyl piperidine hypophosphite (EPHP) (175 mg, 978 μmol), 1,1'-azobis(cyclohexanecarbonitrile) (ACHN) (2.9 mg, 12 μmol), and 2.45 mL of anhydrous *o*-xylene. After connecting the Schlenk flask with a flame-dried reflux condenser, the mixture was deoxygenated by four cycles of freeze-pump-thaw and back-filled with N₂. After the last cycle, the reaction mixture was stirred 10 min at r.t. and immersed into a pre-heated oil bath at 110 °C to start the reaction. The reaction mixture was allowed to stir at 110 °C for 3 h before quenching by cooling the reaction flask with liquid N₂. The solution was then diluted with 4 mL of toluene, washed with deionized water (5 mL × 3) and brine (5 mL × 2). After precipitation into 90 mL of MeOH, the precipitates were collected through centrifugation, washed with 90 mL of MeOH, and concentrated *in vacuo*, yielding a white powder (122 mg, 61% yield). *M_{n, GPC}* = 371 kDa (MALS detector), *D* = 1.52. ¹H NMR (500 MHz, CD₂Cl₂) δ 7.37–6.21 (br m, ArH), 4.62–4.17 (br m, NFHBS RArCH₂OCH₂CH₂C₄F₉), 3.93–3.58 (br s, NFHBS RArCH₂OCH₂CH₂C₄F₉), 2.66–0.71 (m, all CH₂s and CHs from VTPA and NFHBS unit backbone, and NB ring) ppm. ¹³C NMR (126 MHz, CD₂Cl₂) δ 147.8, 145.6,

140.0, 129.1, 128.5, 123.8, 122.3, 73.0, 62.0, 40.3, 29.7 ppm. FT-IR (ATR): 3130–2980, 2970–2820, 1587, 1489, 1312, 1273, 1130, 1074, 1028, 885, 826, 750 cm^{-1} . T_g : 145 °C. TGA: 300–390 °C, 11% mass loss, 390–444 °C, 77% mass loss, 12% mass remaining above 500 °C. **Brush I, II, IV, and V** were synthesized analogously to **Brush III**.

General Procedure for Preparation of Polymer Thin Films:

Preparation of Polymer Thin Films on Silicon Wafer. The Si wafer was treated by UV- O_3 exposure for 5-10 min. The films were prepared by spin-casting of brush solutions in anisole ((**Brush I**: 1.0 wt%; **Brush II**: 3.0 wt%; **Brush III**: 1.0 wt%, **Brush IV**: 1.5 wt%; **Brush V**: 1.0 wt%; filtered through a 200 nm PTFE syringe filter) at (i) 500 rpm for 5 s; (ii) 3000 rpm for 30 s; and (iii) 3500 rpm for 30 s (2000 $\text{rpm}\cdot\text{s}^{-1}$ acceleration for each step) on a pre-treated Si wafer. The thermally-annealed films were annealed on a 125 °C hot plate under N_2 atmosphere for a predetermined amount of time.

Preparation of Polymer Thin Films on PEDOT:PSS-Coated Si Wafers. A Si wafer (2-inch diameter) was treated by UV- O_3 exposure for 10 min. PEDOT:PSS films were then prepared by spin-casting a PEDOT:PSS solution (filtered through a 450 nm nylon syringe filter) at (i) 250 rpm for 5 s; (ii) 2000 rpm for 30 s; and (iii) 3500 rpm for 30 s (2000 $\text{rpm}\cdot\text{s}^{-1}$ acceleration for each step) on the pre-treated Si wafer, followed by annealing at 140 °C for 1 h under N_2 atmosphere. Brush films were then prepared by spin-casting of 1 wt.% brush solution in anisole (filtered through a 200 nm PTFE syringe filter) at (i) 500 rpm for 5 s; (ii) 3000 rpm for 30 s; and (iii) 3500 rpm for 30 s (200 $\text{rpm}\cdot\text{s}^{-1}$ acceleration for each step) on the PEDOT:PSS-coated Si wafers. Thermally-annealed films were annealed on a 125 °C hot plate for a predetermined amount of time.

Preparation of Polymer Thin Films on PEDOT:PSS-Coated ITO Glass. ITO glass (1 cm × 1 cm) was cleaned by (i) heating in acetone at reflux for 2 min, (ii) rinsing with clean acetone twice, and (iii) sonicating in acetone for 20 min. Steps (ii) and (iii) were repeated with isopropyl alcohol. Clean ITO glass was then treated by UV-O₃ exposure for 20 min, followed by 10 min of incubation. PEDOT:PSS films were prepared by spin-casting a PEDOT:PSS solution (filtered through a 450 nm nylon syringe filter) at (i) 250 rpm for 5 s; (ii) 2000 rpm for 30 s; and (iii) 3500 rpm for 30 s (2000 rpm·s⁻¹ acceleration for each step) on the pre-treated ITO glass, followed by annealing at 160 °C for 30 min under N₂ atmosphere. Brush films were then prepared by spin-casting of 1 wt.% brush solution in anisole (filtered through a 200 nm PTFE syringe filter) at (i) 500 rpm for 5 s; (ii) 3000 rpm for 30 s; and (iii) 3500 rpm for 30 s (200 rpm·s⁻¹ acceleration for each step) on the PEDOT:PSS-coated ITO glass. Thermally-annealed films were annealed on a 125 °C hot plate for a predetermined amount of time.

Preparation of Hole-Only Devices (HODs). The HODs were fabricated with the device structure of indium tin oxide (ITO)/poly(3,4-ethylenedioxy-thiophene): polystyrene sulfonate (PEDOT:PSS) (40 nm)/HTL (25 nm)/Al (100 nm). The ITO and Al were utilized as the anode and the cathode, respectively.

Preparation of OLED Devices. The OLEDs were fabricated with the device structure of ITO/PEDOT:PSS (~40 nm)/HTL (~25 nm)/9,10-bis(4-(9*H*-carbazol-9-yl)-2,6-dimethyl phenyl)-9,10-diboraanthracene (CzDBA) (40 nm)/1,3,5-tri(3-pyridyl)-phen-3-ylbenzene (TmPyPB) (45 nm)/8-hydroxyquinolatolithium (Liq) (1 nm)/Al (100 nm). The ITO and Al were utilized as the anode and the cathode, respectively. The Liq was

selected as an electron injection layer (EIL), whereas PEDOT:PSS served as a hole injection layer (HIL). TmPyPB was employed as an electron transport layer (ETL) and CzDBA was used as the green emitting layer (EML). The poly(9,9-dioctylfluorene-*alt*-*N*-(4-sec-butylphenyl)-diphenylamine) (TFB) or TPA-based materials was utilized as hole transport layers (HTLs). The chemical structures of Liq, CzDBA, TmPyB, and TFB are presented in Figure 2.21a. The pre-patterned ITO glass was consecutively cleaned with ultrasonication in deionized (DI) water, acetone, and ethanol, followed by drying with N₂ and UV-O₃ treatment for 20 min prior to use. The PEDOT:PSS layer was spin-cast on ITO substrates at 4000 rpm and subsequently annealed at 120 °C for 10 min, then PEDOT:PSS coated ITO substrates were transferred to N₂ glovebox. For the TFB device, TFB solution (8 mg/mL in chlorobenzene) was spin-cast at 3000 rpm, then annealed at 120 °C for 10 min. The devices with LC or HT brushes were prepared by spin-casting of 1 wt.% polymer solutions in anisole (filtered through a 200 nm PTFE syringe filter) at (i) 500 rpm for 5 s; (ii) 3000 rpm for 30 s; and (iii) 3500 rpm for 30 s (200 rpm·s⁻¹ acceleration for each step), followed by annealing at 125 °C for a predetermined amount of time. The emitting layer (CzDBA), the electron transporting layer (TmPyPB), the electron injecting layer (Liq), and Al cathode were consecutively evaporated in the vacuum chamber with predetermined thicknesses. Then, the device was sealed with curable UV resin in N₂ glovebox.

CHAPTER III
PHOTOTRIGGERED PORE GENERATION IN POLYMER FILM WITH THE
CONTROL OF POROSITY*

3.1 Introduction

Global warming and climate change these days are related to carbon dioxide (CO₂) emission that exceeds the acceptable levels, which has been recognized as a persistent environmental issue. Conventional methods, such as cryogenic separation, temperature swing adsorption, and pressure swing adsorption, have been used for CO₂ capture. However, the relatively-high power consumptions and operating costs of these approaches limited their practical application scopes.⁹⁷⁻¹⁰⁰ Therefore, the development of new materials for CO₂ capture technologies is urgently needed for further reducing air pollution with superior efficiency. Porous materials represent a promising platform toward defusing problems of current gas separation techniques and combating global warming and air pollution.¹⁰¹⁻¹⁰⁶

Gas adsorption with porous membranes denotes a competitive approach for separating CO₂ and other air pollutants from industrial emissions, due to its cost-efficiency, scalability, and feasibility of use.¹⁰⁷⁻¹¹¹ Amongst, polymer membranes with pores have shown numerous advantages enabled from the distinct properties of polymers,

*Adapted with permission from “Photo-Triggered Pore Generation by Extracting Bottlebrush Polymers with the Control of Porosity in Polymer Films” by Kang, N.; Pang, J.; Leonhardt, E. E.; Li, M.; Zhou, H.-C.; Sun, G.; Trefonas, P.; Wooley, K. L., **2020**, *in preparation*.

such as low cost, chemical stability, and low density.¹¹²⁻¹¹⁶ In this regime, the development of polymeric porous membranes has been focused on the controllability of material porosities. Specifically, the controllable pore size, density, and morphology that allow for selective gas permeation and tunable gas adsorption capacity of porous membrane are highly desirable and beneficial for gas separation technology.¹¹⁷⁻¹¹⁹ Although various techniques to prepare polymeric porous membranes have been developed, there are many issues yet to be resolved for the fabrication of polymer materials with well-controlled porosities.

We designed a new tactic, *i.e.*, selectively extracting polymers with well-defined compositions, sizes, and topologies from the polymeric matrix, to generate pores and control the porosity of porous polymer films or membranes. Applying BBPs as sacrificial templates to produce pores, it is anticipated that the pore dimensions and morphologies could be controlled by the predetermined architectures of the extractable bottlebrushes, while the extents of porosity could be adjusted by changing the volume fraction of extractable domain contents over the matrix elements. The overall system included both positive-tone and negative-tone chemically amplified resists (CARs) that depends upon well-established photoacid chemistry. For the positive-tone CAR, photoacid-labile components turn into soluble in a developer solution and are “washed away” by developing upon light exposure. On the other hand, a negative-tone CAR contains functional groups that undergo photoacid-catalyzed crosslinking reactions, which produces an ultimately-increased resistance to an aqueous base developer. Triggered by

UV or e-beam irradiation exposure and completed by developing, the pore formations occur concurrently with the crosslinking of matrix domains.

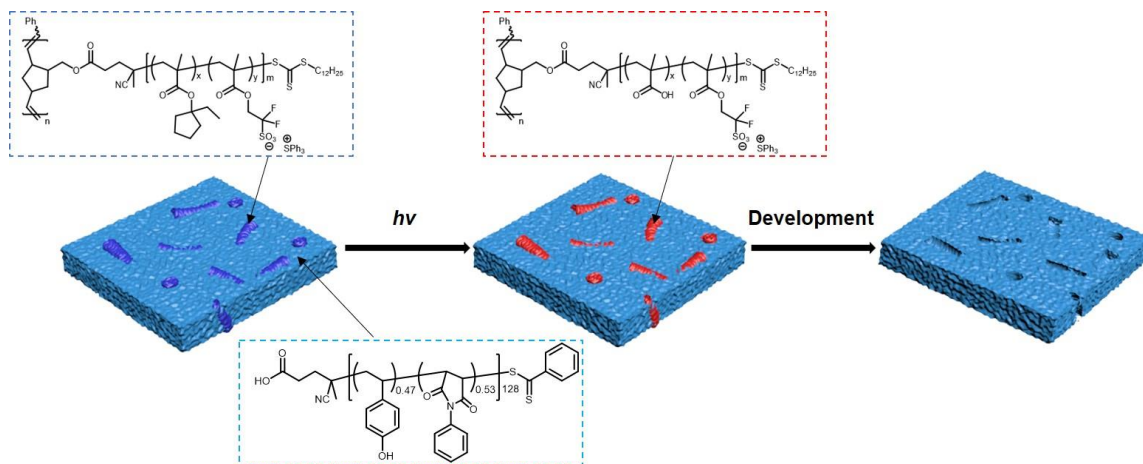


Figure 3.1. Illustrative diagram of the porous membrane preparation. Positive-tone photoresist moiety of BBPs (dark blue) is deprotected (red) upon exposure to light and extracted after the lithographic development process, while negative-tone matrix polymers (light blue) are crosslinked.

As depicted in Figure 3.1, the hydrophobic ethylcyclopentyl ester functionalities in the porogenic positive-tone BBPs were transferred into the aqueous base, the developer, soluble carboxylic acids through acidolysis reactions, which enabled their removal from the system to construct the pores. Simultaneously, acid-catalyzed electrophilic aromatic substitutions occurred on the *ortho*-positions of the phenols in the negative-tone matrix polymers to afford crosslinking towards mechanical and chemical resistances. Different from our previous lithographic studies,²⁴⁻²⁶ the photoacid generators (PAGs) were covalently incorporated into the BBPs to ensure the sufficient deblocking of ethylcyclopentyl esters, due to the concern of acid competition between the

aforementioned two reactions. Moreover, undesirable aggregations of PAGs could be minimized through the random/statistical microstructure along with the grafts of BBPs. By modulating the chemical composition, concentric and lengthwise dimensions, and stoichiometry of porogenic BBPs in the cast mixtures, as well as exposure dosages, the porosity of the resulting membrane could be precisely tuned.

3.2 Results and Discussion

Design and Syntheses of Extractable BBPs and a Matrix Polymer. The design of polymer components used to form the porous membrane was referred to our previous works on the e-beam lithographic photoresist polymers.¹⁹⁻²¹ An extractable BBP (**E-BBP**), polynorbornene-*g*-poly((1-ethylcyclopentyl methacrylate)-*co*-(triphenyl sulfonium 1,1-difluoro-2-(methacryloxy)ethane sulfonate)) (P[NB-*g*-P(ECPMA-*co*-(TPS-DFEMA))]), was designed and synthesized to comprise side-chains bearing the lithography-addressable ECPMA and the photoacid-sourceable TPS-DFEMA functional moieties in a random/statistical manner, which ensures enhanced accessibility of photoacids to ECPMA units by reducing the acid diffusion length. The macromonomer (**MM**), *exo*-5-norbornene-3-poly((1-ethylcyclopentyl methacrylate)-*co*-(triphenyl sulfonium 1,1-difluoro-2-(methacryloxy)ethane sulfonate)) (NB-P(ECPMA-*co*-(TPS-DFEMA))), was synthesized *via* RAFT copolymerizations of two functional acrylate monomers, ECPMA and TPS-DFEMA (Scheme 3.1a), at predetermined feed ratios to control the chemical compositions (Table 3.1). A set of macromonomers with different

compositions, **MM1**, **MM2**, and **MM3**, was obtained and used for grafting-through ROMP (Scheme 3.1b) to prepare the corresponding **E-BBP1**, **E-BBP2**, and **E-BBP3** (experimental details are notated in Section 3.4.3).

Scheme 3.1. Syntheses of macromonomers, **E-MMs** (a) and extractable bottlebrush polymers, **E-BBPs** (b).

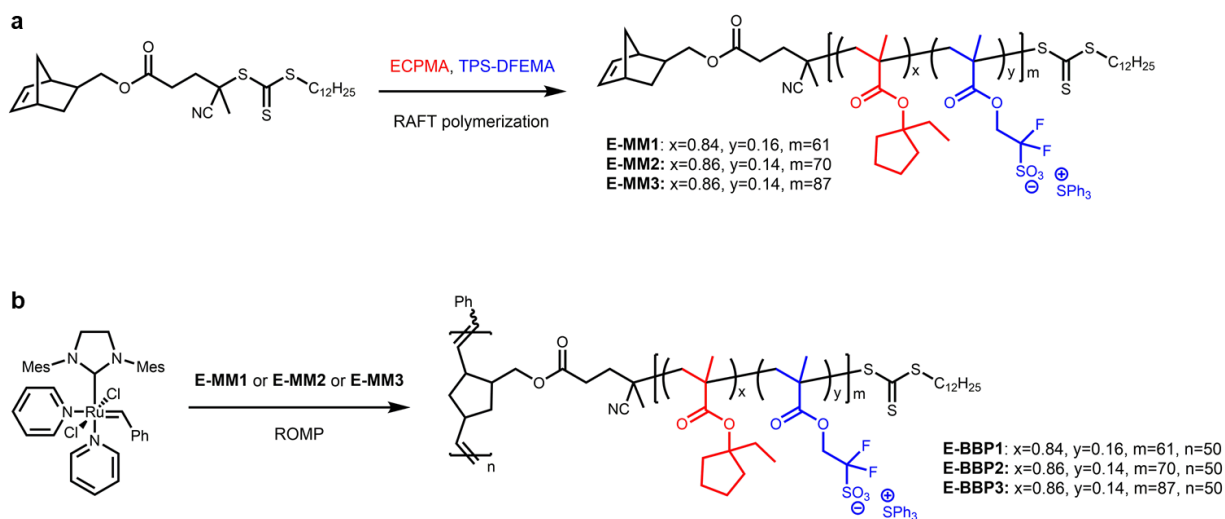


Table 3.1. RAFT copolymerizations of ECPMA and TPS-DFEMA.

| | [NB-CTA] ₀ : [ECPMA] ₀ : [TPS-DFEMA] ₀ : [AIBN] ₀ | T (°C) | Time (h) | Yield ^a (%) | $M_{n,NMR}$ (kDa) | $M_{n,SEC}$ ^b (kDa) | \bar{D} |
|--------------|--|-----------|-------------|---------------------------|----------------------|-----------------------------------|-----------|
| E-MM1 | 1:45:5:0.15 | 70 | 19 | 15 | 15.2 | 21.0 | 1.04 |
| E-MM2 | 1:48:5:0.3 | 70 | 36 | 23 | 16.3 | 21.4 | 1.06 |
| E-MM3 | 1:46:5:0.3 | 70 | 36 | 33 | 20.1 | 24.0 | 1.05 |

^aMass yield (actual yield of the product over the theoretical yield). ^bBy SEC using LS detection (based on injected mass).

The molar mass of **MMs** from ¹H NMR spectroscopy (Table 3.1, calculated by comparing the integrals between NB alkenyl protons, peak A at *ca.* 6.08 ppm, and the characteristic methylene protons of DFEMA, peak T at *ca.* 4.60 ppm, Figure 3.2, as well

as all aliphatic protons) were consistent with size exclusion chromatography-multiangle light scattering (SEC-MALS) analyses. However, precise molar mass characterizations of bottlebrush polymers, **E-BBPs**, were not available from both NMR and SEC, due to the relatively lower ROMP efficiencies. The SEC traces of **E-BBP1** (Figure 3.3b, red) show a dual-modal distribution with approximately 50:50 integrated area ratios from the peak of **MM1** (23 min) and the peak of bottlebrush (18 min). The ROMP conversion of **MM1** was calculated as *ca.* 20 %, based on the molar ratio between **E-BBPs** and residual **MMs** which was derived from the integrated area ratio (weight ratio) from SEC traces. The ROMP conversions of **MM2** (~ 78 %) and **MM3** (~ 60 %) (calculated from ¹H NMR analyses, Figure 3.10) were improved by decreasing the proportion of ionic TPS-DFEMAs in each macromonomer, but the amount of residual macromonomers was still a force to be reckoned with.

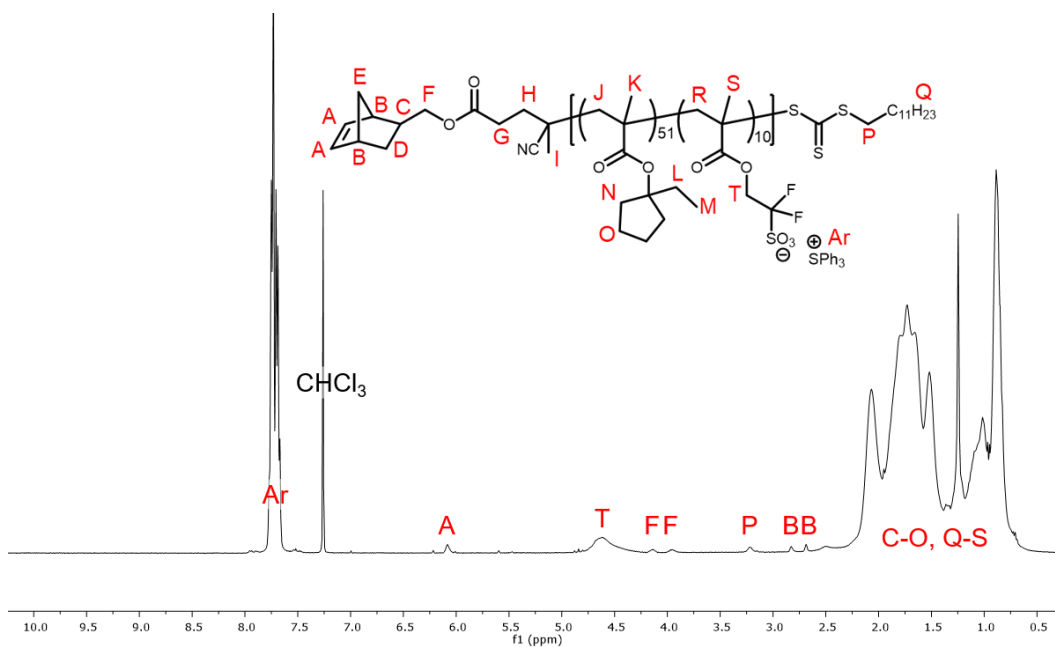


Figure 3.2. ¹H NMR (400 MHz, CDCl₃) spectra of **E-MM1**.

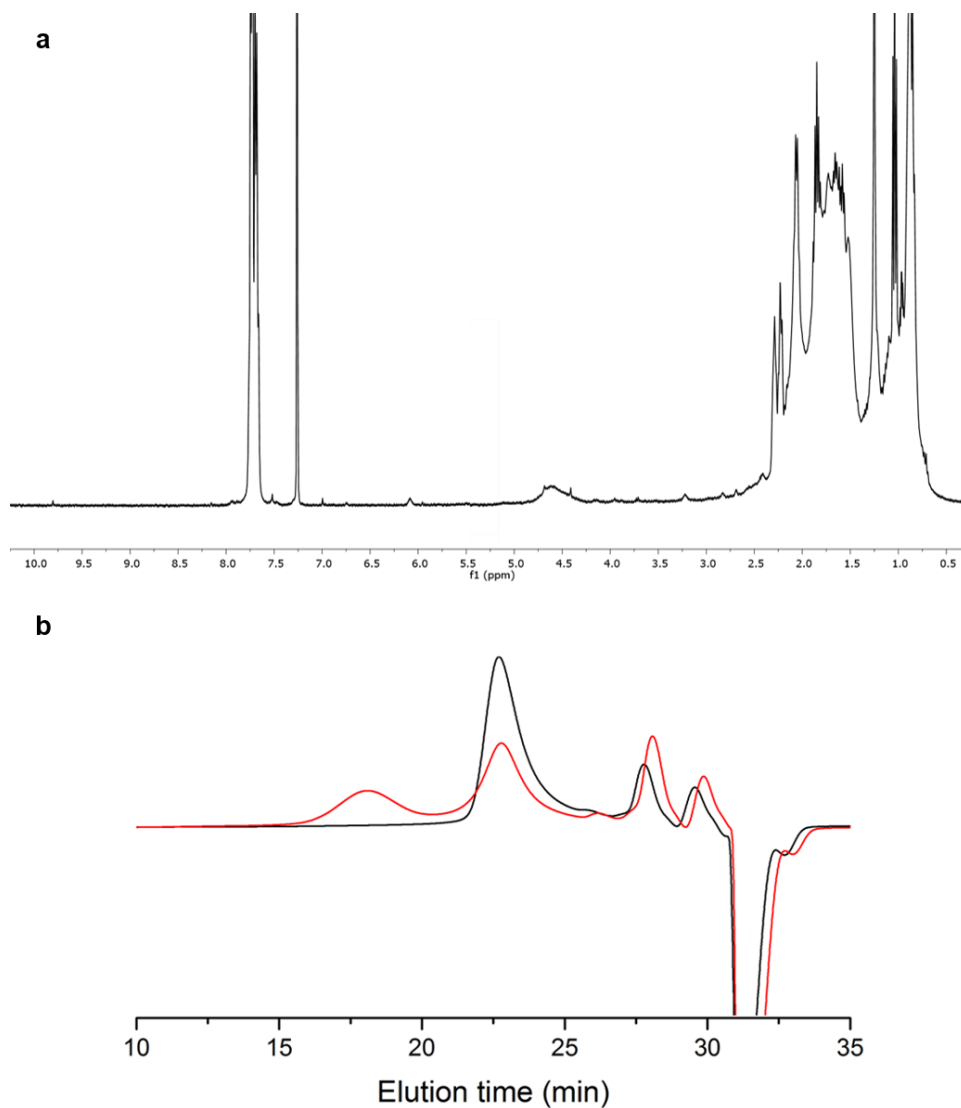


Figure 3.3. (a) ¹H NMR (400 MHz, CDCl₃) of **E-BBP1**. (b) SEC traces of **E-MM1** (black) and **E-BBP1** (red).

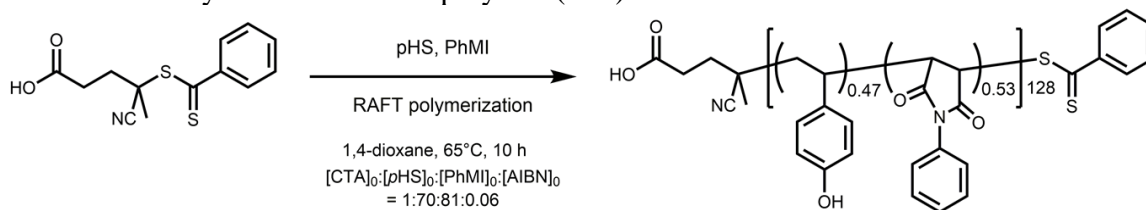
We speculated that the inefficient ROMP is caused by the sufficient solubility of E-MM macromonomer in the ROMP solvent, which is one of the crucial efficiency-factors in ROMP.¹²⁰⁻¹²¹ The ionic groups in TPS-DFEMA units decrease the solubility of macromonomers in dichloromethane (DCM), and subsequently reduce the reaction processability. Other factors, such as undesirable ligand exchange during the ROMP

propagation process, might also affect the overall conversion of macromonomers. It is noteworthy that, despite the deficient ROMP, the mixture of E-BBP and MM could still be used as the porogenic component of the membrane as both polymers have positive-tone photoresist units and photoacid generating functionalities.

Thermal degradation properties of **MM2**, **MM3**, and **E-BBP1** were measured by TGA (Figure 3.9 and 3.11) to determine the baking conditions for the enhancement of acid diffusions during deblocking and crosslinking processes. These polymers, composing functionalities of acid-labile ester and photoacid generator, were degraded stepwise with major weight losses at multiple points as the temperature increased. The very initial weight losses of both **MMs** and **E-BBP** were resulted from the dissociation of RAFT chain-ends and then the degradations of polymers occur stepwise as a result of different thermal degradations of ECPMA and TPS-DFEMA units with distinct compositions (See Section 3.4.3 for TGA data). The TGA characterizations revealed that the extractable polymers can stand up to 150 °C with negligible extents of composition variation.

A linear copolymer, poly(*para*-hydroxy styrene)₆₀-*co*-(*N*-phenyl maleimide)₆₈) (P(*p*HS₆₀-*co*-PhMI₆₈)), was used as the matrix polymer (**MP**), which can undergo the photoacid-catalyzed crosslinking reactions with crosslinker, *N,N,N',N',N'',N''*-hexakis(methoxymethyl)-1,3,5-triazine-2,4,6-triamine (HMMM). The **MP** was prepared through the RAFT copolymerization (Scheme 3.2) under demonstrated reaction conditions.²⁴ The chemical composition of **MP** was confirmed by ¹H NMR analysis (Figure 3.12), which also provided a molar mass (19.3 kDa) that showed sufficient agreement with the MALS-SEC characterization (24.9 kDa).

Scheme 3.2. Synthesis of matrix polymer (**MP**).



Characterizations of Spin-cast Polymer Thin Films before and after EBL

Experiments. Prior to the UV lithography experiments of casted bulk membranes, EBL of polymer thin film comprising **E-BBP**, **MP**, and HMMM crosslinker was conducted to confirm whether the overall design could be realized. As shown in Figure 3.4a, the AFM image of the as-cast polymer film (film thickness: 47 ± 1 nm) showed sufficient surface homogeneity without noticeable phase segregations between **E-BBP** and **MP**. Upon e-beam exposing, post-baking, and aqueous TMAH developing (see section 3.4.3 for details), diverse hollow features were observed from the AFM images of resulting patterns at both $200 \mu\text{C}/\text{cm}^2$ (Figure 3.4b) and $400 \mu\text{C}/\text{cm}^2$ (Figure 3.4c) exposure dosages. The shapes of observed features were varied because the extractable **E-BBPs** were mounted throughout the as-cast thin films with random orientations. As a note, although the design was conceptually proved by the EBL process, the results from AFM imaging indicated that this approach was more suitable for precise tuning the surface roughness of thin films with thickness less than 100 nm (Figure 3.5, film thicknesses: 8 ± 2 nm for $100 \mu\text{C}/\text{cm}^2$, 15 ± 2 nm for $200 \mu\text{C}/\text{cm}^2$, and 15 ± 2 nm for $400 \mu\text{C}/\text{cm}^2$).

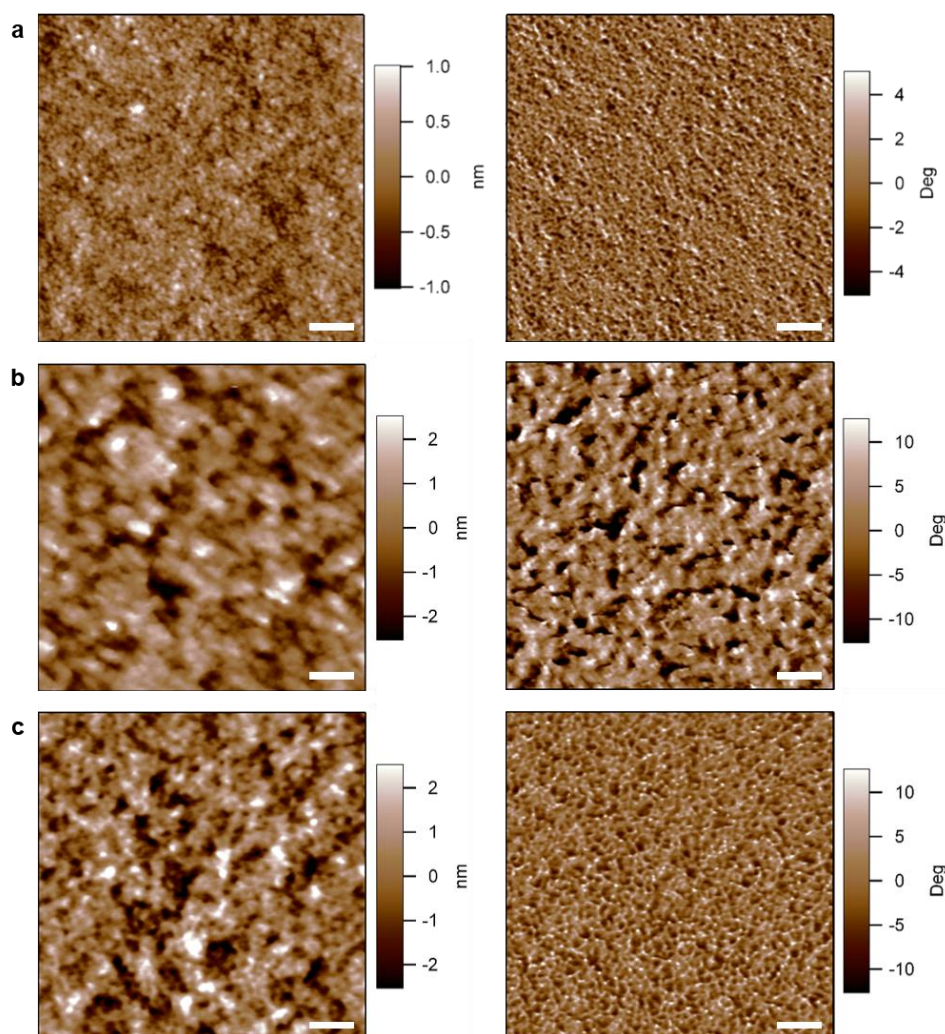


Figure 3.4. Tapping-mode AFM height (left) and phase (right) images. (a) as-cast polymer thin film, (b-c) **EBL-TFs** generated at exposure dosages of (b) 200 and (c) 400 $\mu\text{C}/\text{cm}^2$. Scale bars: 200 nm.

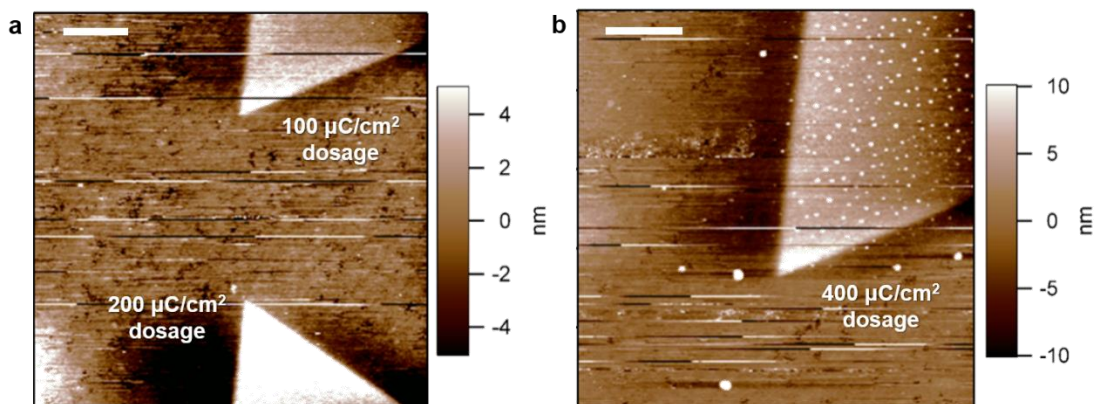


Figure 3.5. Tapping-mode AFM height images of **EBL-TFs** generated triangle patterns at exposure dosages of (a) $100 \mu\text{C}/\text{cm}^2$ (upper, $\text{FT} = 8 \pm 2 \text{ nm}$) and $200 \mu\text{C}/\text{cm}^2$ (lower, $\text{FT} = 15 \pm 2 \text{ nm}$), and (c) $400 \mu\text{C}/\text{cm}^2$ ($\text{FT} = 15 \pm 2 \text{ nm}$). Scale bars: $10 \mu\text{m}$.

Surface Morphology Characterizations of Porous Polymer Membranes. The porous polymer membrane was prepared by simultaneously UV-induced deblocking of **E-BBPs** and crosslinking of **MPs** in the presence of cyclohexanone solvent (see Section 3.4.3 for detail). The surface morphologies of the resulted polymer membranes (**UV-PMs**) before and after developing processes were characterized by scanning electron microscopy (SEM) (Figure 3.6). SEM images revealed that the porous morphologies were only observed after developing the UV-exposed membrane with 0.25M TMAH developer solution (**UV-PM-b**, Figures 3.6c and 3.6d), whereas no pores were observed from the counterpart membrane without the development process (**UV-PM-a**, Figures 3.6a and 3.6b). This implicated that the deblocked **E-BBPs** were dissolved into a TMAH solution and removed from the crosslinked **MP** domain during the development process. To further investigate the role of extractable polymers, a control membrane sample (**CM**) was prepared by using a solution mixture of **MP**, HMMM, and PAG monomer (TPS-

DFEMA). As shown in Figures 3.6e and 3.6f, the surface of **CM** did not exhibit hollow or porous features.

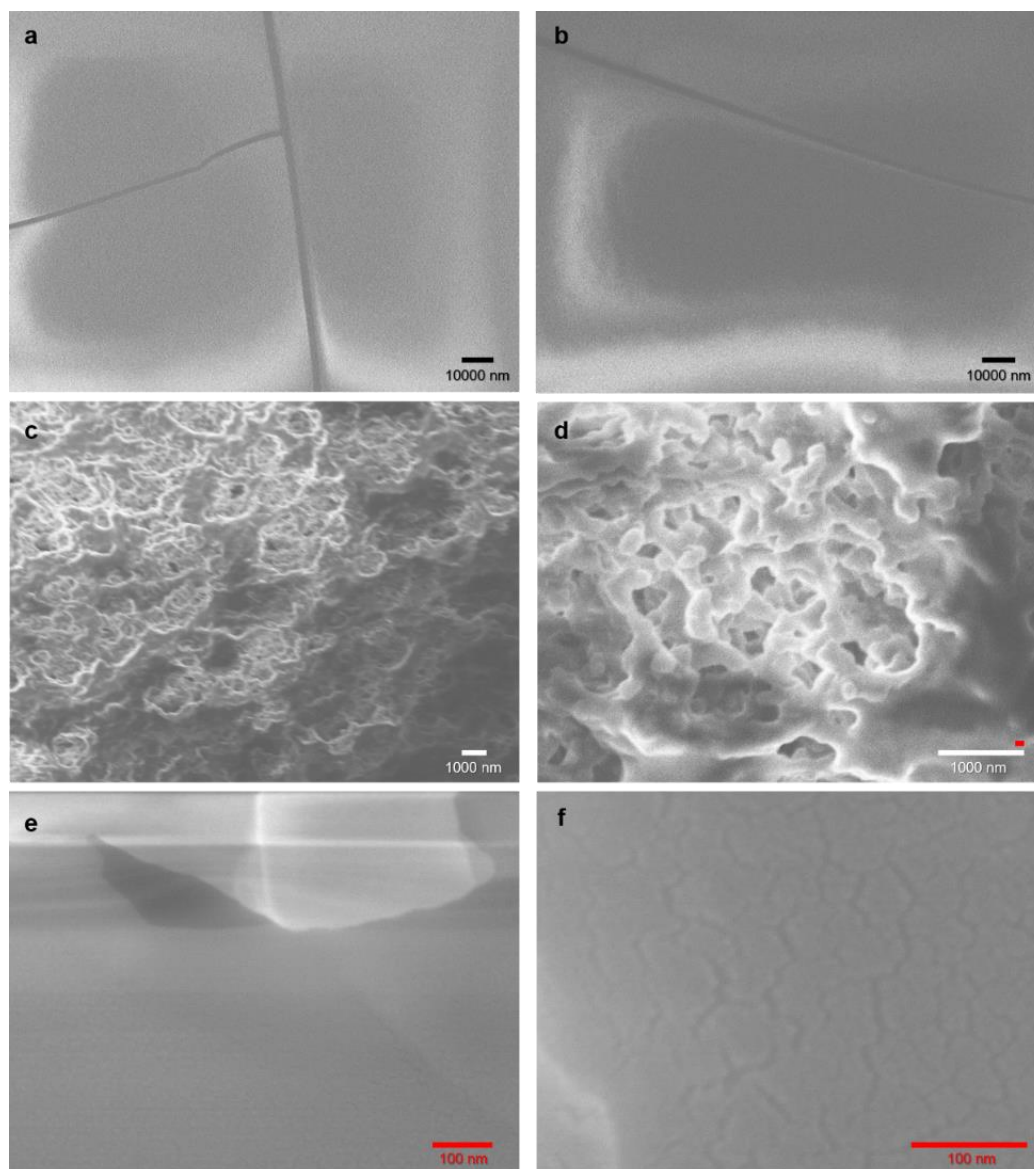


Figure 3.6. SEM images of (a-d) **UV-PM-a**, (c-d) **UV-PM-b**, and (e-f) **CM**. Membranes of (a-b) and (e) had no protective coatings, while membranes of (c-d) and (f) were coated with 3nm Pt/Pd coatings prior to SEM imaging. Scale bars: 10000 nm (a-b, black), 1000 nm (b-c, white), 100 nm (c-f, red).

The pore sizes of **UV-PM-b**, analyzed from SEM images, were in the range from *ca.* 20 nm to few micrometers (Figures 3.6c and 3.6d), which suggested that the **E-BBPs** were not solely distributed within the membrane as unimolecular nanoobjects. The inconsistency between resulted pore sizes with the molecular dimensions of porogenic **E-BBP1** and/or **MM1** implies that the porosity of polymeric porous membrane could be governed by multiple factors. At the current stage, it is difficult to precisely control the dimension and size-distribution of membrane pores by simply varying the BBP architectures. However, the diversity of pore sizes in the porous membrane has been demonstrated on enhancing the gas separation applications of the membrane through contributing more free volumes to facilitate gas diffusion and providing synergetic effects of micro-, meso-, and macro-sized pores.¹²²⁻¹²⁴

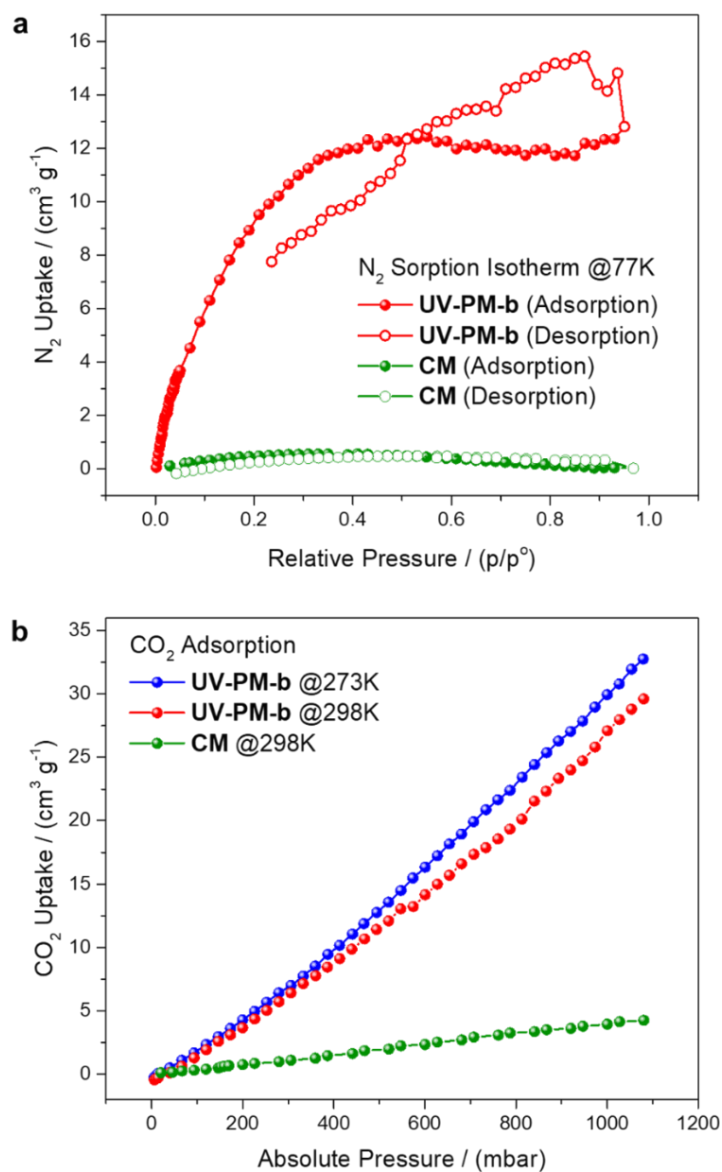


Figure 3.7. (a) N₂ sorption isotherms of **UV-PM-b** (red) and **CM** (olive) at 77K. The filled symbols represent adsorption and the empty symbols represent desorption data. (b) CO₂ adsorptions of **UV-PM-b** at 273K (blue) and 298K (red) and of **CM** at 298K (olive).[#]

[#] Collected by Dr. Jiandong Pang (Texas A&M University).

N₂ Sorption isotherm and CO₂ adsorption properties of Porous Polymer Membranes. To characterize the porosity of **UV-PM-b**, the N₂ sorption isotherms (Figure 3.7a) and CO₂ adsorptions (Figure 3.7b) were measured. In addition, gas sorption measurements of **CM** were conducted for comparison as **CM** was composed of the same membrane components (crosslinked **MPs**) as **UV-PM-b** while displaying nonporous morphology (Figure 3.6e and 3.6f). As shown in Figure 3.7a, the absence of porosity in **CM** only enabled a maximum N₂ gas adsorption capability of ~0.6 cm³/g at 0.3 atm. On the contrary, an over 18-fold increase of N₂ gas adsorption at the same pressure was revealed by **UV-PM-b** upon the introduction of meso-sized pores (Figure 3.7a, red vs. olive). At 77 K, **UV-PM-b** exhibited a maximum N₂ gas adsorption capacity of 12.8 cm³/g at 0.4 atm, which maintained relatively consistent up to 0.6 atm and fluctuated with further increasing of N₂ pressure to 1 atm. We speculated that the diverse dimensions of pores and layered structure in **UV-PM-b** could enable a combination of Type I and Type II isotherms for the overall N₂ adsorption. Interestingly, the N₂ sorption isotherm cycle of **UV-PM-b** at 77 K was not reversible, which suggested that a pore conformational variation might occur after physisorption and chemisorption of N₂.¹²⁵⁻¹²⁸

At 1080 mbar (~1.065 atm), the **UV-PM-b** exhibited CO₂ absorption capacities of 32.8 cm³/g and 29.6 cm³/g at 273 K (Figure 3.7b, blue) and 298 K (red), respectively. The CO₂ uptake of **UV-PM-b** was *ca.* 40% higher than a recently-reported nanoporous polymer network based upon ladder-like polymer of intrinsic microporosity (PIM) bearing phenol functionalities, despite the 10-fold lower N₂ absorption capacity.¹²⁹ We attributed the enhanced CO₂ absorption to two major factors, *i.e.*, the introduction of basic melamine

moieties and the generated meso- and macro-sized pores. By comparison, the **CM** only exhibited 4.25 cm³/g of CO₂ absorption at 298K and 1080 mbar (Figure 3.7b, olive). The *ca.* 80% of the capacity decrease in **CM** confirmed the crucial role of porosity in **UV-PM-b** to facilitate higher CO₂ uptake. Taking account of the inherently-lower microporosity of **UV-PM-b**, we anticipate this system holds potentials toward CO₂-selective separation applications.

Table 3.2. The comparison of porous materials for the CO₂ uptakes from the literature.^{103, 129-140}

| Sample | Type | CO ₂ uptake (mmol/g) | | reference |
|-----------------------------------|--|---------------------------------|--------------|-----------------------------------|
| | | 1 bar, 273 K | 1 bar, 298 K | |
| UV-PM-b | Porous polymer network (PPN) | 1.46 | 1.19 | This dissertation |
| NUT-1 | PPN | 1.87 | 1.43 | Sun et al. ¹³⁰ |
| PPN-6-CH₂Cl | PPN | 2.59 | 1.28 | Lu et al. ¹³¹ |
| mPTPM-2 | PPN | 2.41 | 1.25 | Hu et al. ¹³² |
| DCX-BCMBP copolymer | Hypercrosslinked polymer (HCP) | - | 1.70 | Martín et al. ¹³³ |
| PIM-1-C3-TA | Polymer of intrinsic microporosity (PIM) | - | 2.05 | Sekizkardes et al. ¹³⁴ |
| MC-OCP-NPN-1 | PIM | 1.67 | 0.84 | Zhu et al. ¹²⁹ |
| P77 | PIM | 1.80 | - | Klein et al. ¹³⁵ |
| Azo-COP-2 | Covalent organic polymer (COP) | 2.55 | 1.53 | Patel et al. ¹³⁶ |
| COP-1 | COP | - | 1.36 | Xiang et al. ¹³⁷ |
| CMP-1 | COP | 2.05 | 1.18 | Dawson et al. ¹⁰³ |
| PCN-68 | Metal-organic framework (MOF) | - | 1.10 | Yuan et al. ¹³⁸ |
| ZIF-78 | MOF | 3.24 | 1.94 | Banerjee et al. ¹³⁹ |
| NH₂-MIL-53 (Al) | MOF | - | 1.14 | Couck et al. ¹⁴⁰ |

3.3 Conclusion

We have designed and prepared a porous polymer membrane system with CO₂-selective absorption capability. Generated by extracting the positive-tone porogenic polymer components and crosslinking the negative-tone matrix polymers through a “one-pot” photolithography process, porous membrane, **UV-PM**, with dimensional diversity of pores exhibited selective gas sorption properties for N₂/CH₄ and CO₂ gases. The obtained results established a rational foundation toward advanced CO₂ capture and separation technologies. Moreover, the robust design principle and the diversity of applicable chemistry create a promising and facile toolbox to produce porous materials.

3.4 Experimental Section

3.4.1 Materials

The Grubbs third-generation catalyst (G3),⁸³ 4-hydroxy styrene (*p*HS),¹⁴¹ *exo*-norbornene RAFT chain transfer agent (NB-CTA),¹⁴²⁻¹⁴³ were synthesized as previously reported. The 1-ethylcyclopentyl methacrylate (ECPMA) and triphenyl sulfonium difluoro-2-(methacryloxy) ethane sulfonate (TPS-DFEMA) were provided by the Dow Chemical Company. The *N,N,N',N',N'',N''*-hexa(methoxymethyl)-1,3,5-triazine-2,4,6-triamine (HMMM) was purchased from TCI and used without further purification. Other chemicals and reagents were purchased from Sigma-Aldrich, Acros, or VWR, and were used without further purification, unless otherwise noted. Prior to use, the ECPMA was

purified by passing through a neutral alumina column to remove the inhibitor. The tetrahydrofuran (THF) and dichloromethane (CH_2Cl_2) were purified by passing through a solvent purification system (JC Meyer Solvent Systems).

3.4.2 Instrumentation and Characterization

Column chromatography was performed on a CombiFlash Rf4x (Teledyne ISCO) with RediSep Rf columns (Teledyne ISCO).

^1H and ^{13}C NMR spectra were recorded on a Varian 500 spectrometer, interfaced to a LINUX computer using VNMR-J software, or a Bruker AVANCE NEO 400 spectrometer interfaced to Linux Centos 7 using Topspin 4.5.5 software. Chemical shifts were defined based on the solvent proton resonance.

The polymer molar mass was calculated by ^1H NMR spectroscopy, and the molar mass and dispersity (D) were determined and confirmed by size exclusion chromatography (SEC). The SEC was conducted on a Waters 1515 HPLC (Waters Chromatography, Inc.) equipped with a Wyatt Optilab T-rEX differential refractometer (660 nm light source, Wyatt Technology Corp.), a Wyatt DAWN HELEOS II multi-angle light scattering (MALS) detector (658 nm light source, Wyatt Technology Corp.), and a three-column-series (Phenogel 5 μm Linear (2), 100 \AA , and 10⁴ \AA , 300 \times 4.6 mm columns; Phenomenex, Inc.). The system was equilibrated at 40 $^\circ\text{C}$ in THF, which served as the polymer solvent and eluent with a flow rate of 0.35 mL/min. Polymer solutions were prepared at known concentrations (3-5 mg/mL), and an injection volume of 200 μL was used. Data collection and analysis were performed with ASTRA software (Wyatt

Technology Corp.). The dn/dc values of the analyzed polymers were determined from the differential refractometer response.

Thermogravimetric analysis (TGA) was performed under argon (Ar) atmosphere using a Mettler-Toledo TGA2/1100/464, with a heating rate of 5 °C/min. Both measurements were analyzed by using STAR^e version 15.00a software (Mettler-Toledo, Inc.).

The EBL was carried out by using a JEOL JSM-6460 scanning electron microscope equipped with the DEBEN laser stage. The system was operated at 30 kV accelerating voltage and 10 pA beam current with series of exposure dosages with the range from 100 $\mu\text{C}/\text{cm}^2$ (6 mJ/cm^2) to 600 $\mu\text{C}/\text{cm}^2$ (18 mJ/cm^2). An equilateral triangle pattern with a side length of 50 μm was used and it provided a sufficiently large 2-dimensional area for the observation of generated surface features *via* the lithographic process of polymer resists.

Atomic force microscopy (AFM) imaging was performed on an Asylum MFP-3D system (Oxford Instruments, Plc.) in tapping mode using standard silicon tips (T190-25, VISTAprobes; spring constant: 48 N/m, tip radius: ~10 nm, resonance constant: 190 kHz).

Scanning electron microscopy (SEM) images were collected on a JEOL JSM-7500F FE-SEM equipped with a high brightness conical FE gun and a low aberration conical objective lens. Protective coatings for specific samples were produced by 208HR High Resolution Sputter Coater (Ted Pella, Inc.) equipped with a platinum/palladium target.

All N₂ adsorption measurements were performed on a Micromeritics BET 2420 instrument at 77K. Variable Temperature CO₂ adsorption isotherms were performed on a Micromeritics BET 2020 instrument using an ice water bath (for 0 °C) or a Micromeritics Iso Controller (25 °C and 40 °C). Heat of Adsorption values were collected using the Clausius-Capeyron equation and CO₂ adsorption data collected at 0 °C, 25 °C, and 40 °C.¹⁴⁴

3.4.3 Details of Syntheses and Film Preparations

Synthesis of E-MM1 (NB-P(ECPMA₅₁-co-(TPS-DFEMA)₁₀)). To a flame-dried Schlenk flask equipped with a magnetic stir bar, was added NB-CTA (114 mg, 0.224 mmol), ECPMA (1.83 g, 10.1 mmol), TPS-DFEMA (553 mg, 1.12 mmol), AIBN (4.77 mg, 30.4 μmol), and 4.5 mL of 2-butanone. The reaction mixture was deoxygenated through four cycles of freeze-pump-thaw, followed by back-filling with N₂ after the last cycle. The resulting mixture was stirred in the dark at 70 °C to start the polymerization. After 19 h, the polymerization was quenched by freezing the reaction mixture with liquid N₂. The resulting mixture was diluted with 5 mL of CH₂Cl₂ (DCM) and precipitated into 140 mL of cold methanol. Collected precipitates were dissolved in THF and precipitated into 150 mL of cold 20% methanol (MeOH)/Et₂O mixture twice. The collected polymer was kept under vacuum overnight to remove residual solvent, yielding a yellow solid product (375 mg, 15% mass yield). $M_{n, SEC} = 21.0$ kDa (MALS detector), $D = 1.04$. ¹H NMR (400 MHz, CDCl₃) δ 7.89–7.66 (m, ArHs from S⁺Ph₃), 6.15–6.04 (br, CH=CH from NB), 4.88–4.32 (br, OCH₂C(F₂SO₃) from TPS-DFEMA units), 4.20–4.09 (m, NBCH₂O),

4.01–3.91 (m, NBCH₂O), 3.25–3.14 (m, CH₂C₁₁H₂₃ from CTA chain-ends), 2.85–2.78 (m, NB allylic *H*), 2.72–2.66 (m, NB allylic *H*), 2.61–0.57 (m, all the other CHs, CH₂s and CH₃s from NB-CTA, ECPMA units and RAFT chain-ends) ppm (Figure 3.2). ¹³C NMR (101 MHz, CDCl₃) δ 134.9, 131.8, 131.4, 124.7, 36.0, 35.3, 29.1, 25.5, 24.8. **E-MM2** (NB-P(ECPMA_{60-co}-(TPS-DFEMA)₁₀) and **E-MM3** (NB-P(ECPMA_{75-co}-(TPS-DFEMA)₁₂) were obtained by following the same procedure of the synthesis of **E-MM1**, with corresponding reaction conditions shown in Table 3.1 (**E-MM2**: 600 mg, 23 % mass yield, **E-MM3**: 2320 mg, 33% mass yield). The chemical compositions of **E-MM2** and **E-MM3** were analyzed by ¹H-NMR characterizations (Figure 3.8) and their thermal degradation properties were characterized by TGA (Figure 3.9).

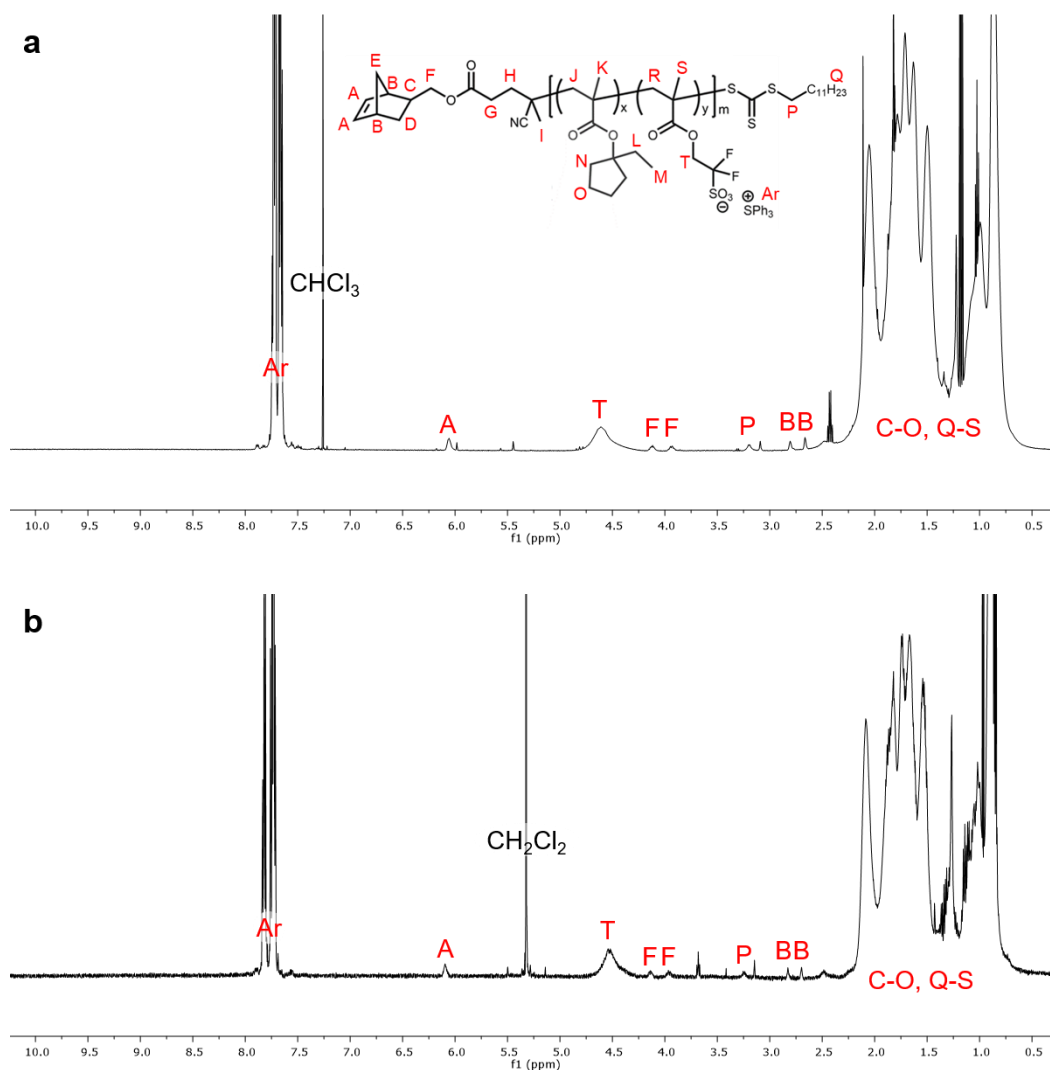


Figure 3.8. ^1H NMR spectra of (a) **E-MM2** (500 MHz, CDCl_3) and (b) **E-MM3** (500 MHz, CD_2Cl_2).

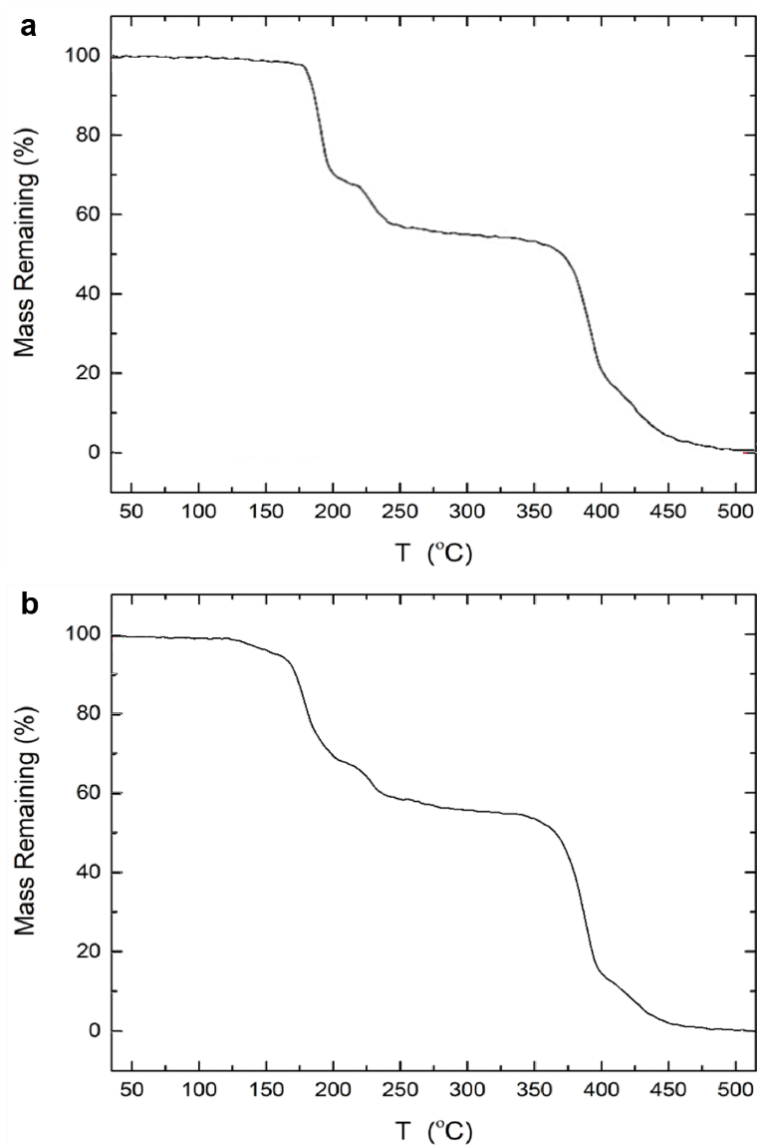


Figure 3.9. TGA traces of (a) **E-MM2**, and (b) **E-MM3**. TGA traces were obtained under Ar atmosphere with a heating rate of 5 °C/min.

Synthesis of E-BBP1 (P[NB-*g*-P(ECPMA₅₁-*co*-(TPS-DFEMA)₁₀)]₅₀). To a flame-dried 10 mL Schlenk flask equipped with a magnetic stir bar, was added 0.5 mL of G3 catalyst stock solution (0.38 mg/mL, 0.52 μmol/mL) and the solution was deoxygenated through three cycles of freeze-pump-thaw. To a separate flame-dried vial,

was added a solution of **E-MM1** (199 mg, 13.1 μmol) in 1.5 mL of DCM and deoxygenated through three cycles of freeze-pump-thaw. Deoxygenated **E-MM1** solution was then added *via* an air-tight syringe to the **G3** solution in the Schlenk flask. The resulting reaction mixture was stirred at r.t. for 1.5 h before quenching the polymerization by the addition of 0.9 mL of ethyl vinyl ether (EVE). The solution was stirred at r.t. for an additional 2 h, and precipitated into 90 mL of 20% MeOH/Et₂O mixture. Precipitates were collected through centrifugation and kept under vacuum overnight to remove residual solvents, yielding a yellow solid product (110 mg, 55% mass yield). $M_{n, \text{SEC}} = 1780$ kDa (MALS detector), $D = 1.68$ (dual-modal distribution with $\sim 50\%$ macromonomer conversion) (Figure 3.3b). ¹H NMR (400 MHz, CDCl₃) δ 7.88–7.57 (m, ArHs from S⁺Ph₃), 6.13–6.04 (br, CH=CH from NB of residual macromonomers), 4.87–4.29 (br, OCH₂C(F₂SO₃) from TPS-DFEMA units), 3.25–3.18 (br m, NBCH₂O and SCH₂C₁₁H₂₃), 2.92–0.52 (m, all the other CHs, CH₂s and CH₃s from ECPMA units, macromonomer backbone, RAFT chain-ends, and NB-ring) ppm (Figure 3.3a). ¹³C NMR (101 MHz, CDCl₃) δ 134.9, 131.4, 124.7, 122.1, 35.3, 34.9, 32.6, 28.3, 24.4, 23.6, 12.6 ppm. TGA: 125–176 °C, 31% mass loss, 176–218 °C, 10% mass loss, 218–324 °C, 6% mass loss, 324–373 °C, 29% mass loss, 373–450 °C, 12% mass loss, 12% mass remaining above 450 °C (Figure 3.11). **E-BBP2** (P[NB-*g*-P(ECPMA_{60-co}-(TPS-DFEMA)₁₀)]₅₀) and **E-BBP3** (P[NB-*g*-P(ECPMA_{75-co}-(TPS-DFEMA)₁₂)]₅₀) were synthesized, following the same procedure of the synthesis of **E-BBP1**, with corresponding reaction conditions shown in Table 3.3 (**E-BBP2**: 216 mg, 68% mass yield, **E-BBP3**: 433 mg, 83% mass yield). The chemical compositions of **E-BBP2** and **E-BBP3** were confirmed by ¹H NMR

characterizations (Figure 3.10) and ROMP conversions were calculated referring to the integral of a $CH=CH$ peak from NB of **E-MM** at *ca.* 6.08 ppm (Figure 3.10 and Table 3.3).

Table 3.3. ROMP of NB-P(ECPMA-*co*-(TPS-DFEMA)).

| | [G3 cat.]:[E-MM] ₀ | [E-MM] ₀ ($\mu\text{mol/mL}$) | T ($^{\circ}\text{C}$) | Time (h) | Yield ^a (%) | ROMP conversion |
|---------------|-------------------------------|---|-----------------------------|-------------|---------------------------|--------------------|
| E-BBP1 | 1:50 | 6.55 | r.t. | 1.5 | 55 | 20 % ^b |
| E-BBP2 | 1:36 | 5.98 | r.t. | 1.5 | 68 | 78 % ^c |
| E-BBP3 | 1:50 | 8.10 | r.t. | 1.5 | 83 | 60 % ^c |

^aMass yield (actual yield of the product over the theoretical yield). Calculated ^bby SEC peak integrations and ^cby ¹H NMR.

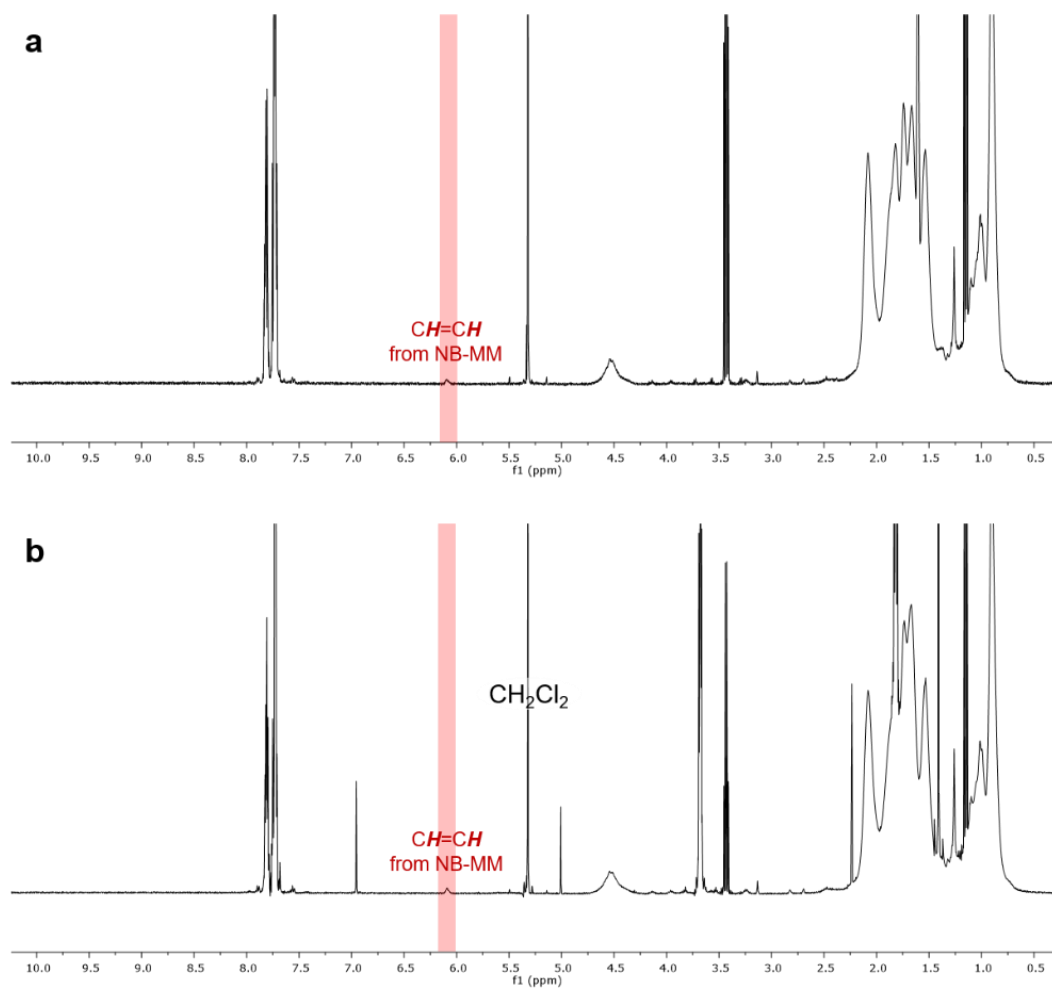


Figure 3.10. ¹H NMR spectra of (a) **E-BBP2** (500 MHz, CDCl₃) and (b) **E-BBP3** (500 MHz, CD₂Cl₂).

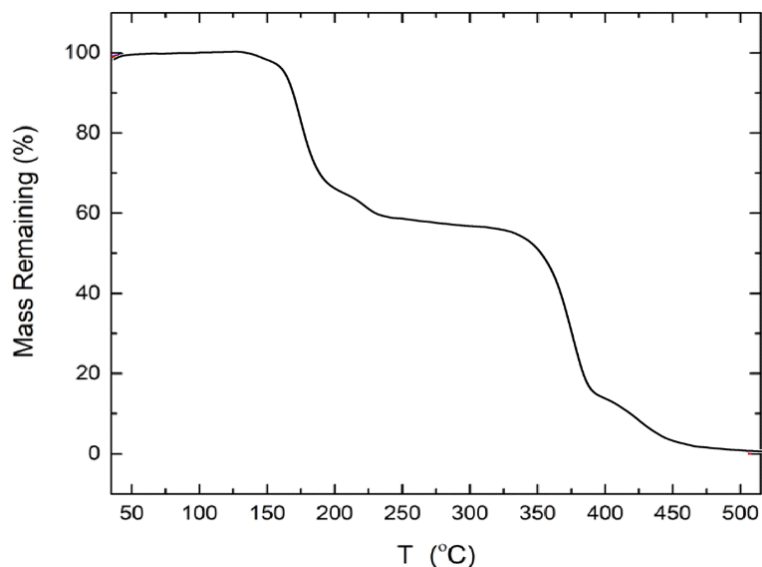


Figure 3.11. TGA trace of **E-BBP1**. TGA traces were obtained under Ar atmosphere with a heating rate of 5 °C/min.

Preparation of MP (P(*p*HS₆₀-*co*-PhMI₆₈)). To a 25-mL flame-dried Schlenk flask equipped with a magnetic stir bar, was added 4-cyano-4-(thiophenylthio)pentanoic acid (118 mg, 0.422 mmol), *p*HS (3.55 g, 29.5 mmol), *N*-phenyl maleimide (PhMI) (5.67 g, 32.7 mmol), AIBN (3.80 mg, 23.0 μmol), and 10 mL of anhydrous 1,4-dioxane. The reaction mixture was deoxygenated through three cycles of freeze-pump-thaw, followed by back-filling with N₂ after the last cycle. The resulting solution was stirred at 65 °C for 10 h. Then the polymerization was quenched by freezing the reaction mixture with liquid N₂. The pink viscous polymer solution was diluted with 10 mL of THF and collected by precipitation into diethyl ether (Et₂O) twice. Precipitates were washed by Et₂O and dissolved in acetone. The polymer was then collected by precipitation into 500 mL of hexane and kept under vacuum overnight to remove residual solvent, yielding a light pink solid product (5.12 g, 65% yield based on *ca.* 85~86% conversion for both monomers).

$M_{n, SEC} = 24.9$ kDa (MALS detector), $D = 1.01$. ^1H NMR (400 MHz, $\text{DMSO-}d_6$) δ 9.70–9.18 (br, phenol **H**s), 7.74–5.88 (m, Ar **H**s, backbone chain end **CH**), 3.95–0.72 (m, all CH_2 s and **CH**s from *p*HS unit backbone and MI units) ppm (Figure 3.12). ^{13}C NMR (101 MHz, $\text{DMSO-}d_6$) δ 152.5, 130.0, 129.1, 127.3, 127.2, 126.1, 124.5, 123.5, 123.3, 116.1, 113.6, 68.0, 62.0, 51.4, 48.5, 47.2, 46.2, 46.0, 43.1, 41.2, 41.0, 31.4, 30.6, 27.9, 27.6 ppm.

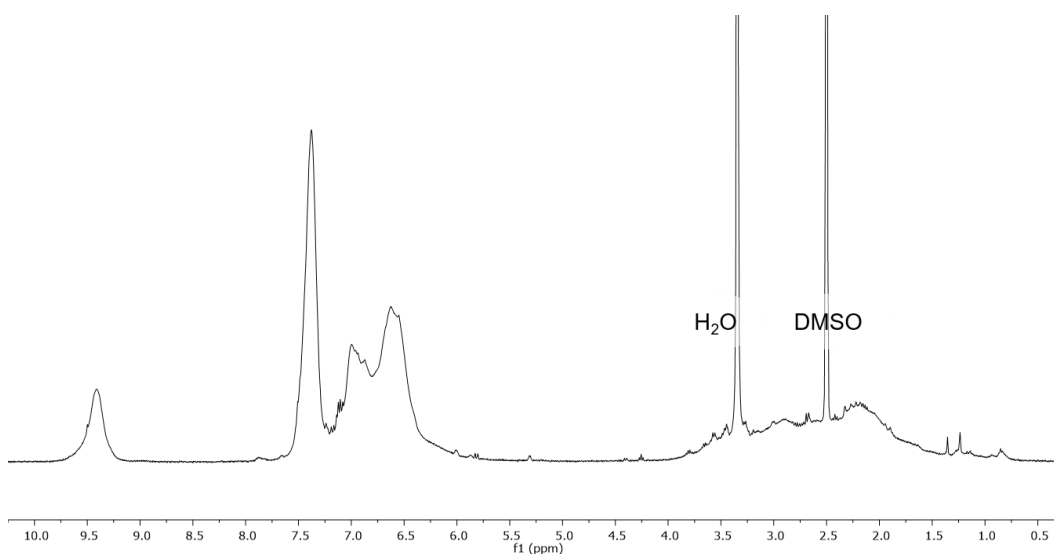


Figure 3.12. ^1H NMR (400 MHz, $\text{DMSO-}d_6$) of **MP**.

Preparation of the Polymer Thin Film for the EBL Test. The Si wafer was treated by UV- O_3 exposure for 5 min. The casting mixture in cyclohexanone was prepared by mixing solutions of E-BBP1, MP, and HMMM (E-BBP1: 0.3 wt%, MP: 1.5 wt%, HMMM: 0.3 wt%). The films were prepared by spin-casting of a prepared 2.1 wt% cast mixture (filtered through a 200 nm PTFE syringe filter) at (i) 500 rpm for 5 s; and (ii) 3000 rpm for 30 s ($200 \text{ rpm}\cdot\text{s}^{-1}$ acceleration for each step) on a pre-treated Si wafer.

EBL Procedure of Polymer Thin Film on Si Wafer. After electron beam “writing” with a predesigned pattern, the exposed wafer was post-baked on a 90 °C hotplate for 1 min and dipped into 0.25 M tetramethylammonium hydroxide (TMAH) aqueous developer solution for 1 min. The wafer was rinsed with DI water and dried by N₂ blowing.

General Procedure for the Preparation of Porous Polymer Membranes. The 7.0 wt% cast mixtures in cyclohexanone were prepared with respective compositions for (A) the porous membrane, **UV-PM**, (**E-BBP1**: 1.0 wt%, **MP**: 5.0 wt%, **HMMM**: 1.0 wt%) and for (B) the reference sample, **CM**, (**MP**: 5.5 wt%, **HMMM**: 1.0 wt%, small-molecule photoacid generator (PAG) (**TPS-DFEMA**): 0.5 wt%). The cast solutions were transferred to the silicon molds and cured by the exposure under 254 nm UV light for 10 h. The exposed membranes were post-baked on a 90 °C hotplate for 4 min and immersed into 0.25 M tetramethylammonium hydroxide (TMAH) aqueous developer solution for 3 min. The membranes were rinsed with DI water and dried by N₂ blowing.

CHAPTER IV
SYNTHESIS OF AMPHIPHILIC MOLECULAR BOTTLEBRUSHES WITH HIGHER
GRAFTING DENSITY OF SIDE-CHAIN POLYMERS

4.1 Introduction

Asymmetric inorganic nanoparticles (NPs) or nanorods (NRs) have great potential as the functional materials in a variety of technological applications, such as the next generation of solar cells, diodes, sensors, and probes in biomedical devices. The physical properties of asymmetric NPs are highly dependent on their nanoscale sizes and shapes.¹⁴⁵⁻
¹⁵³ Hence, a nanoscale control of NP's dimensions and morphologies is important and necessary to provide adequate material properties for each application field. Although numerous approaches to fabricate inorganic NRs or rod-like nanocrystals have been developed, many challenges are remaining to more precisely control their sizes and/or shapes at the nanoscale level.

A polymer is a prominent material for the nanoscale-control of size and shape, attributed to a bottom-up approach of polymer synthesis using selective monomers or macromonomers with predetermined compositions. Building up polymer architectures using macromonomer building blocks provides a wide selection of functionalities and final molecular architectures with the precision of adjustments at the atomic level. In this regime, polymer template-assisted NP syntheses have been explored, by many scientists and engineers recently, as the way to control the dimensions of inorganic nanocrystals.¹⁵⁴⁻

¹⁵⁸ One of the complex polymer architectures, a bottlebrush structure, yields inherent cylindrical nanoarchitectures and possesses the potential to be utilized as a templating agent for the asymmetric NP growth.

Core-shell brush polymers had been studied as highly feasible templates to attain 1D anisotropic inorganic NRs with desired aspect ratios owing to their cylindrical shape.¹⁵⁵⁻¹⁵⁶ In reference ¹⁵⁶, it has been demonstrated that the backbone stiffness of a brush-structured cellulose polymer ensured the formation of Au and Au/Fe₃O₄ nanocrystals with rigid rod-like morphologies. Thus, the bottlebrush polymers with highly rigid backbones are greatly anticipated to be utilized to assist the growth of asymmetric NP with a well-defined nanostructure, as the backbone rigidity is expected to reduce the entanglement of BBP during solution-state inorganic NR synthesis. Particularly, the amphiphilic copolymer, polystyrene-*block*-poly(acrylic acid) (PS-*b*-PAA), represents one of the polymer templates that has been developed as a templating material due to the inherent properties of acrylic acid units that induce nucleation of inorganic nuclei to grow in the polymer-assisted formation of inorganic nanocrystals field.¹⁵⁹⁻¹⁶² However, there are only very few examples of bottlebrush polymers exploited in templating applications up to today.

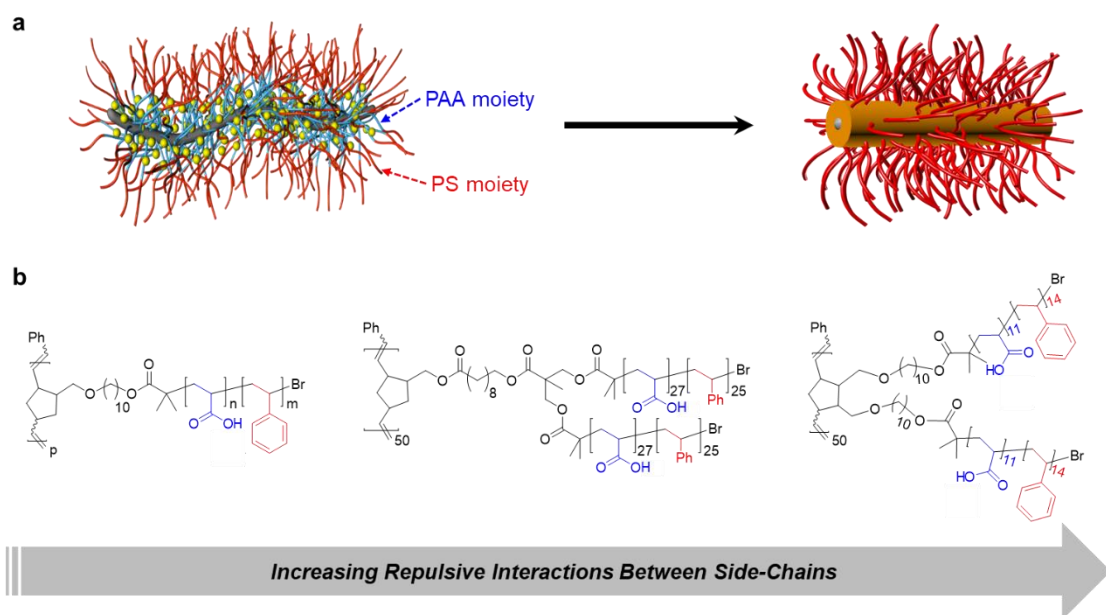


Figure 4.1. (a) Illustration of an amphiphilic PAA-*b*-PS bottlebrush polymer before the growth of inorganic nanorod (left) and after the completion of nanorod formation (right). (b) Chemical compositions of the overall design to increase the grafting density or side-chain density of BBP.

The extended conformation of BBP is produced by having enough repulsive intramolecular forces between graft chains. We conceived the BBP with a norbornene backbone, which is known for its inherent rigidity, would be a very promising material to assist the anisotropic growth of inorganic NPs. Besides, the repulsive intrachain forces are expected to increase further when more polymers emerge out from each backbone unit. In this regard, we developed BBPs with a higher density of side-chain polymers (or graft polymers) by employing double and dual grafted norbornene-functionalized amphiphilic macromonomer frameworks (Figure 4.1). We hypothesized that dual- and double-grafted BBPs will retain their extended shapes in the solution-state due to increased repulsive intrachain interactions.

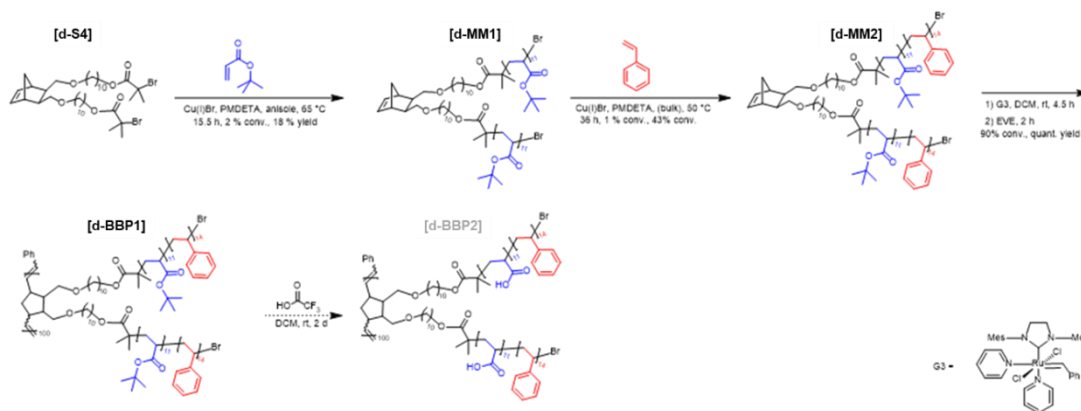
4.2 Results and Discussion

Preparation of Amphiphilic Bottlebrush Polymers with Higher Grafting Densities. Inverse amphiphilic BBPs were designed to have norbornene backbones where the interior contains the poly(acrylic acid) (PAA) segment and the polystyrene (PS) blocks are located on the outer part of side-chains. Since the solubility of PAA in most organic solvents is limited, *tert*-butyl acrylate (*t*BA) was used for the BBP preparation, as tertiary butyl groups can be removed by the following deprotection step and converted *Pt*BA to PAA. *Tert*-butyl acrylate and styrene are both commercially available monomers with relatively inexpensive costs, and they are miscible when used together so that evades any undesired micro- and nano-scale phase segregation during the polymer syntheses. Graft block copolymers with densely grafted side-chains, polynorbornene-*graft*-dual-(poly(*tert*-butyl acrylate)-*block*-polystyrene)) (PNB-*g*-d-(*Pt*BA-*b*-PS), **d-BBP1**) and polynorbornene-*graft*-(double-(poly(*tert*-butyl acrylate)-*block*-polystyrene)) (PNB-*g*-(db-(*Pt*BA-*b*-PS)), **db-BBP1**), were obtained through ROMP of macromonomers, **d-MM2** (NB-d-(*Pt*BA-*b*-PS)) and **db-MM2** (NB-db-(*Pt*BA-*b*-PS)) (Scheme 4.1 and Scheme 4.2). Then, the amphiphilic BBPs with poly(acrylic acid)-*block*-polystyrene (PAA-*b*-PS) side-chains, were obtained through deprotecting tertiary butyl groups from *t*BA units.

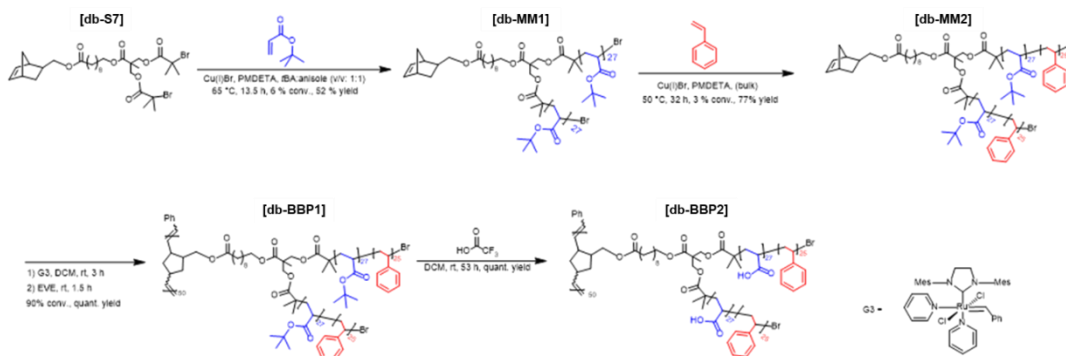
Macromonomers, **d-MM2** and **db-MM2**, were synthesized by the chain-extension of **d-MM1** and **db-MM1**, respectively. The **d-MM1** and **db-MM2** were prepared *via* ATRP using the dual chain norbornene initiators **db-S7** (Scheme 4.4) and the double-chain norbornene initiators **d-S4** (Scheme 4.3), respectively. Both ATRP initiators were

mounted with multiple bromine (Br) initiation sites per one norbornene functional group to afford two chains of poly(*tert*-butyl acrylate) (PtBA) growing from one norbornene unit. Then NB-d-PtBA (**d-MM1**) and NB-db-PtBA (**db-MM1**) were then extended with polystyrene (PS), resulting in the production of **d-MM2** and **db-MM2**. Prepared norbornene functionalized dual-chain block copolymers (**d-MM2**) and double-chain block copolymers (**db-MM2**) were used for constructing denser grafted BBPs, **d-BBP1** and **db-BBP2**, by ROMP. To secure the efficacy of ROMP of **d-MM2** and **db-MM2**, each ATRP initiator was designed to contain enough spacings between norbornene unit and polymerizable moiety. The ¹H NMR spectroscopy was utilized to monitor the conversion of monomers for ATRP polymerization, as well as to analyze the chemical compositions of the final products of each step (Figure 4.6, 4.9, and 4.10). Molar masses of prepared polymers were confirmed by SEC characterizations.

Scheme 4.1. Synthesis of **d-BBP** through ATRP and ROMP.



Scheme 4.2. Synthesis of **db-BBP** through ATRP and ROMP.



We encountered the synthetic challenge in the preparation of the dual chain BBPs, due to the low ROMP conversion of **d-MM2** observed from SEC (Figure 4.2, The SEC trace of **d-BBP1** exhibited a dual-modal distribution peaked at *ca.* 20 min (polymerized **d-MM2** or **d-BBP1**) and *ca.* 23 min (non-polymerized residual **d-MM2**)) and the extremely low percent yield of the sum of residual macromonomers and BBPs (~10%), that is calculated without considering the ROMP conversion. We speculated the low conversion was caused by the limited accessibility to the ROMP propagation site, caused by 2- and 3- positioned side-chain polymers. Since the characterizations on chemical composition and molar mass of **d-BBP1** were hardly attained, the deprotection step of **d-BBP1** was aborted. We speculate that the low efficiency of ROMP for **d-MM2** was induced by the overwhelmingly high steric hindrances between the two neighboring graft chains positioned at the 2- and 3-carbons of the norbornene groups.

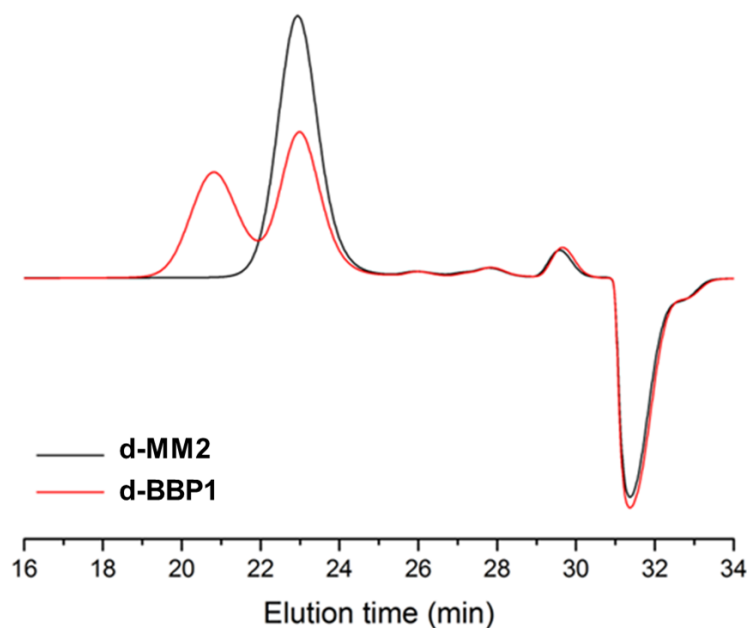


Figure 4.2. SEC traces of **d-MM2** (black) and **d-BBP1** (red).

Characterizations of Molecular Architecture of db-BBP2 on HOPG.

Morphologies of double chain brush (**db-BBP2**), scattered on the substrate, were characterized by AFM imaging. The dilute brush solution in methanol/chloroform mixture was spin-cast onto the highly oriented pyrolytic graphite (HOPG) to spread individual BBPs throughout the substrate (detailed in Section 4.4.2). The AFM images of **db-BBP2** (Figure 4.3) displayed the rod-like architectures and the low entanglements of BBPs, whereas it is reported that BBPs with single grafts or less rigid backbone compounds showed the entanglements to a greater extent.¹⁶³⁻¹⁶⁶

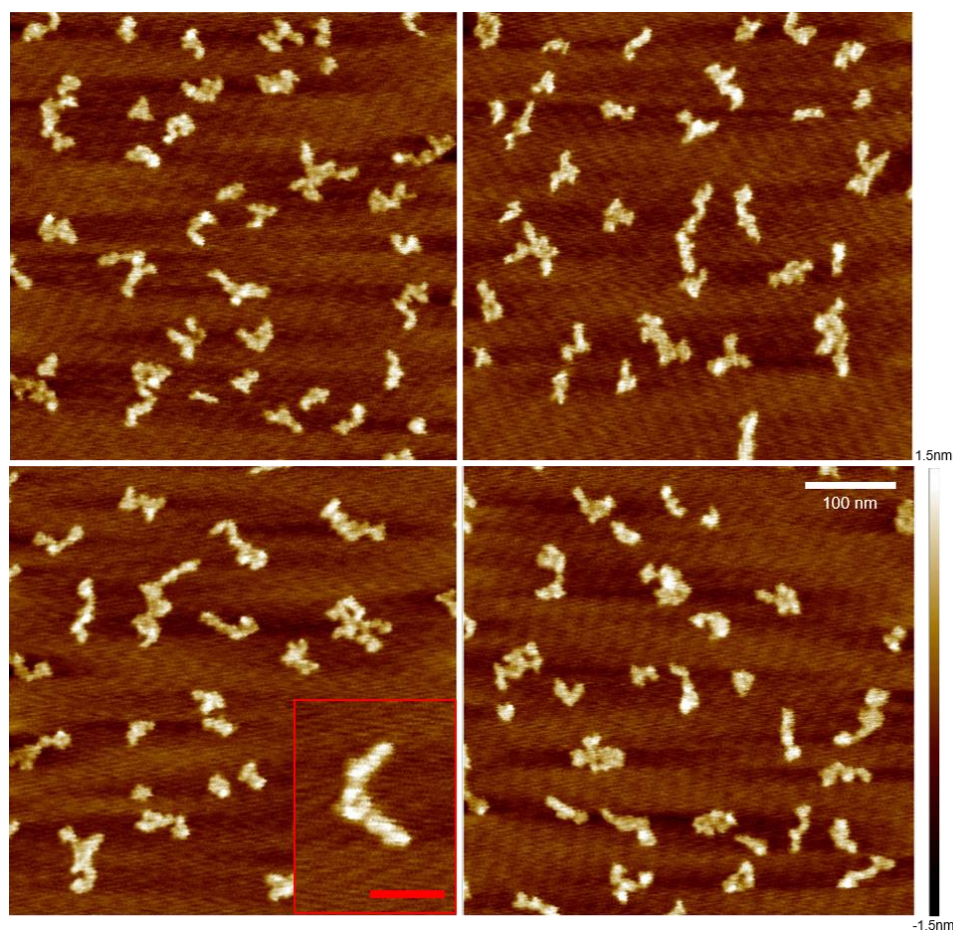


Figure 4.3. Multi-mode AFM height images (500×500 nm area) of individual **db-BBP2s** on a HOPG substrate. The inserted red box is a zoomed-in image of an individual bottlebrush. Scale bars: 50 nm (red), 100 nm (white).

The average diameter of **db-BBP2** observed by AFM (21 ± 2.0 nm) was consistent with a theoretical value of the BBP diameter based on the contour length calculated from the chemical compositions of **db-BBP2** (32 nm). Meanwhile, the backbone length observed from AFM images of deposited **db-BBP2** on the HOPG substrate was much longer (56 ± 15 nm) than a theoretical value of calculated backbone contour length (28 nm) and showed that the size distribution. The higher value of observed backbone length by

AFM compared to a theoretical backbone contour length can be endorsed by the extension of side-chain polymers in a direction parallel to the backbone direction (Figure 4.4b), as BBPs were randomly dispersed on the substrate during the spin-casting process of a dilute polymer solution.

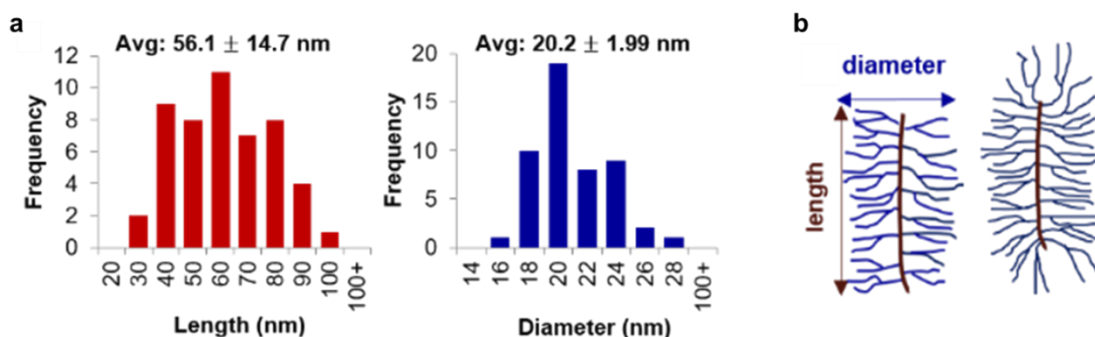


Figure 4.4. (a) Histogram of the size distribution of **db-BBP2** by AFM characterization. The average of **db-BBP2** size was calculated by counting 100 individual particles from AFM height images. (b) Schematic depicts of bottlebrush polymers on the HOPG substrates. An illustration of BBP on the left is showing the possible morphology with extending side-chains parallel to backbone polymer.

4.3 Conclusion

Densely grafted amphiphilic bottlebrush polymers, **d-BBP** and **db-BBP**, that have a higher number of graft polymers emerging out from the backbone than single-grafted BBP. The inverse amphiphilic double grafted BBP, **db-BBP2**, was successfully prepared and the morphology of prepared polymer was characterized by AFM. Although, the morphologies of **db-BBP2** observed by AFM did not have a perfect rod-shape, the impact of side-chain density of BBP on the polymer morphology. Our results underpinned that

the increment of grafting density encourages a reduction in the degree of entanglement, as well as an augmentation of backbone rigidity, inducing more-extended shapes of BBPs.

4.4 Experimental Section

4.4.1 Materials

The Grubbs G3 catalyst,¹⁶⁷ methyl 10-((*tert*-butyl diphenyl silyl)oxy)decanoate (**db-S1**),¹⁶⁸ methyl 10-((*tert*-butyl diphenyl silyl)oxy)decanoic acid (**db-S2**),¹⁶⁸ ((10-Bromodecyl)oxy)(*tert*-butyl)diphenyl silane (**d-S1**),¹⁶⁹ and (10-bromodecyloxy)(*tert*-butyl)diphenylsilane¹⁷⁰ were synthesized according to the literature reports. Other chemicals and reagents were purchased from Sigma-Aldrich, Acros, and VWR and were used without further purification unless otherwise noted. Tetrahydrofuran (THF) and dichloromethane (CH₂Cl₂) were purified by passing them under argon pressure through a solvent purification system (JC Meyer Solvent Systems) before use.

4.4.2 Instrumentation and Characterization

Column chromatography was performed on a CombiFlash Rf4x (Teledyne ISCO) with RediSep Rf columns (Teledyne ISCO).

¹H and ¹³C NMR spectra were recorded on a Varian 500 spectrometer, interfaced to a LINUX computer using VNMR-J software, or a Bruker AVANCE NEO 400 spectrometer interfaced to Linux Centos 7 using Topspin 4.5.5 software. Chemical shifts were defined based on the solvent proton resonance peaks.

FTIR spectra were recorded on an IR Prestige 21 system (Shimadzu Corp., Japan) equipped with an Attenuated Total Reflection (ATR) accessory and analyzed by using IRsolution v.1.40 software.

Electrospray ionization mass spectrometry (ESI-MS) and atmospheric pressure chemical ionization mass spectrometry (APCI-MS) experiments were performed using a Thermo Scientific LCQ-DECA instrument. The sample was directly infused at a flow rate of 6 $\mu\text{L}/\text{min}$. The spray voltage was set to -4.5 kV, and the sheath gas and auxiliary gas flow rates were set to 50 and 10 arbitrary units, respectively. The capillary transfer temperature was held at 250 $^{\circ}\text{C}$. Xcalibur 2.0 software was used for data acquisition and processing.

Size Exclusion Chromatography (SEC) was used to determine polymer molecular weight and molecular weight distribution (or dispersity, \mathcal{D}). The SEC was conducted on a Waters 1515HPLC (Waters Chromatography, Inc.) equipped with a differential refractive index (RI) detector (Wyatt Technology, Optilab T-rEX), a multi-angle laser light scattering (MALLS) detector (Wyatt Technology, DAWN HELEOS II, 658 nm) using ASTRA software (Wyatt Technology; the dn/dc values of the analyzed polymers were determined from the differential refractometer response based on sample concentration), and three-column series (Phenogel 5 μm ; 100 \AA , 10⁴ \AA , and Linear (2); 300 \times 4.6 mm columns; Phenomenex, Inc.). Polymer solutions were prepared at a known concentration (3-5 mg/mL) and 200 μL of an injection volume was used. After the filtration through a 0.2 μm PTFE filter, the polymer sample was passed through the SEC

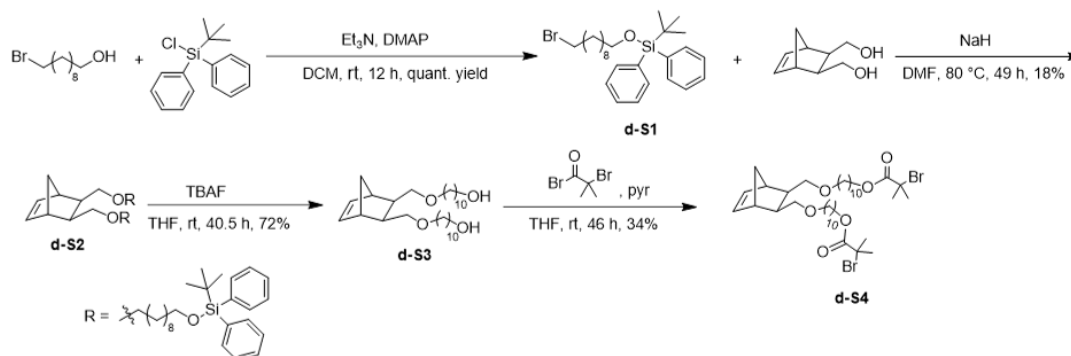
system equilibrated at 40°C in tetrahydrofuran (THF) as the mobile phase with the flow rate of 0.35 mL/min.

The Atomic Force Microscopy (AFM) imaging was performed on a Bruker Multimode 8 system (Bruker Corp.) in PeakForce Tapping® Mode with ScanAsyst® image optimization software using ScanAsyst®-Air tips (Bruker Corp.; spring constant: 0.4 N/m; resonance constant: 70 kHz). AFM images were analyzed using the Nanoscope Analysis software (Bruker Corp.) to obtain the height and the length of nanostructures. BBPs were dispersed on freshly-cleaved HOPG substrates by spin-casting ((i) 500 rpm for 10 seconds, (ii) 3000 rpm for 30 seconds; acceleration rate at 200 rpm/s) of a dilute solution of BBPs in MeOH/CHCl₃ mixture (20 µL, 0.02 mg/mL). The averages and deviations of heights and lengths were obtained by analyzing 100 counts of BBPs.

4.4.3 Synthesis and Sample Preparations

A. Preparation of Double-chain Templating BBP

Scheme 4.3. Synthesis of dual ATRP initiator (**d-S4**).



Synthesis of d-S2. To the two-neck RBF equipped with a stir bar and a condenser dried with flame under the vacuum, was added NaH (191 mg, 7.96 mmol) and suspended in 5 mL of anhydrous dimethylformamide (DMF). In a separated vial dried with flame under vacuum, was added *exo*-5-norbornene-2,3-dimethanol (528 mg, 3.42 mmol) and dissolved in 2.5 mL of anhydrous DMF. To the NaH suspension, an *exo*-5-norbornene-2,3-dimethanol solution was added and allowed to stir for 35 min until no bubbles were generated. Meanwhile, **d-S1** (4.03 g, 8.48 mmol) was dissolved in 8 mL of anhydrous DMF. After 10 min of stirring, the solution of **d-S1** was added to the RBF, equipped with a dried condenser. The resulting reaction mixture was stirred for 60 h at 80 °C. After 60 h, the reaction mixture was cooled down to room temperature and 2 mL of H₂O was added to quench the excess NaH and stirred for further 1 h. The organic solution was extracted with 80 mL of ethyl acetate and washed with H₂O (2 × 20 mL) and brine solution (30 mL). The collected organic solution was then dried over Na₂SO₄ for 2 h. The crude product was concentrated under the reduced pressure, and isolated by column chromatography (diethyl ether/hexane), yielding 43% of the disubstituted product. ¹H NMR (400 MHz, CD₂Cl₂) δ 7.69–7.64 (8H, m, (*ortho*-) ArH), 7.41–7.36 (12H, m, (*meta*- and *para*-) ArH), 6.18–6.11 (2H, m, NB CH=CH), 3.67 (4H, t, (*J* = 6.5 Hz), CH₂CH₂OTBDPS), 3.60–3.17 (8H, m, NB-2,3-(CH₂OCH₂)), 2.71 (2H, p (*J* = 1.7 Hz), NB allylic H), 1.78–1.67 (2H, m, CHs from 2,3-position of NB), 1.61–1.19 (32H, m, OCH₂(CH₂)₈CH₂OTBDPS), 1.06–0.83(20H, m, CH₃ from TBDPS and CHCH₂CH bridgehead) ppm. ¹³C NMR (101 MHz, CD₂Cl₂) δ 135.9, 134.6, 129.9, 128.0, 127.9, 72.4, 71.5, 64.5, 45.3, 42.8, 41.0, 33.0, 30.3, 30.0, 29.9, 29.8, 27.1, 26.7, 26.2, 19.5. FT-IR

(ATR): 3062, 2931, 2855, 1729, 1584, 1470, 1432, 1395–1343, 1255, 1191, 1097, 1007, 936, 910, 822 cm^{-1} . HRMS (APCI) m/z : $[\text{M} + \text{H}]^+$ Calc'd for $\text{C}_{61}\text{H}_{91}\text{O}_4\text{Si}_2$ 943.6450; Found 943.6429.

Synthesis of d-S3. To the RBF equipped with a stir bar and dried with flame under the vacuum, was added **d-S2** (510 mg, 540 μmol) and dissolved 8 mL of anhydrous THF. To the **d-S2** solution, was added 3.3 mL of tetrabutylammonium fluoride (TBAF) (1.0 M in THF) dropwise, then the reaction mixture was stirred for 48.5 h at rt. After 48.5 h, the solution was concentrated under the reduced pressure yielding yellow crude oil. The crude product was purified by column chromatography (ethyl acetate/hexane) and the isolated product was concentrated under the reduced pressure, yielding viscous clear oil (180.8 mg, 72% yield). ^1H NMR (400 MHz, CDCl_3) δ 6.22–6.11 (2H, m, CH=CH from NB), 3.61–3.23 (12H, m, CH_2OH and $\text{NBCH}_2\text{OCH}_2$), 2.17 (2H, p ($J = 1.7$ Hz), NB allylic **H**), 1.78–0.93 (38H, m, **CH**s from 2,3-position of NB, $\text{OCH}_2(\text{CH}_2)_8\text{O}$, **OH**s and CHCH_2CH bridgehead) ppm. ^{13}C NMR (101 MHz, CDCl_3) δ 137.7, 129.9, 115.7, 72.4, 71.5, 63.2, 45.3, 43.1, 41.0, 33.3, 30.5, 30.2, 30.0, 26.7, 26.2 ppm. FT-IR (ATR): 3589–2790, 3056, 2920, 2857, 1604, 1463, 1374, 1341, 1239, 1104, 1059, 899, 827 cm^{-1} . HRMS (ESI) m/z : $[\text{M} + \text{H}]^+$ Calc'd for $\text{C}_{29}\text{H}_{55}\text{O}_4$ 467.4095; Found 467.4093, $[\text{M} + \text{NH}_4]^+$ Calc'd for $\text{C}_{29}\text{H}_{58}\text{O}_4\text{N}$ 484.4360; Found 484.4359, $[\text{M} + \text{Na}]^+$ Calc'd for $\text{C}_{29}\text{H}_{54}\text{O}_4\text{Na}$ 489.3914; Found 489.3911.

Synthesis of d-S4. To the RBF equipped with a stir bar and dried with flame under the vacuum, were added **d-S3** (62.5 mg, 134 μmol (268 μmol of alcohol end-groups)) and 7.5 mL of anhydrous THF, then stirred for 10 min before adding α -bromoisobutyryl

bromide (BIBB) (123 mg, 540 μmol) solution. The resulting reaction mixture was stirred for 46 h at room temperature. After 46 h, the white solid was filtered through a celite plug and the celite plug was washed with 10 mL of CH_2Cl_2 . The collected mixture was filtered through a 200 nm PTFE syringe filter and the solvent was removed under reduced pressure. The resulting mixture was partitioned into an organic and an aqueous solution with 50 mL of $\text{CH}_2\text{Cl}_2/\text{H}_2\text{O}$ (v/v=1:1). The organic solution was collected and washed with brine (30 mL) twice, then dried over Na_2SO_4 . The resulting solution was concentrated and the product was isolated by column chromatography ($\text{Et}_2\text{O}/\text{hexane}$) and concentrated under the reduced pressure, yielding viscous liquid product (35.1 mg, 34% yield). ^1H NMR (400 MHz, CD_2Cl_2) δ 6.21–6.12 (2H, m, NB $\text{CH}=\text{CH}$), 4.14 (4H, t (J = 6.6 Hz), $\text{CH}_2\text{O}(\alpha\text{-BIB})$), 3.57–3.19 (8H, m, NB CH_2OCH_2), 2.71 (2H, p (J = 1.7 Hz), NB allylic H), 1.91 (12H, s, CH_3 from $\alpha\text{-BIB}$ groups), 1.72–1.20 (36H, m, CH s from 2,3-position of NB, $\text{OCH}_2(\text{CH}_2)_8\text{O}$, and CHCH_2CH bridgehead) ppm. ^{13}C NMR (101 MHz, CD_2Cl_2) δ 171.9, 137.7, 72.4, 71.4, 66.5, 56.8, 45.3, 43.0, 41.0, 31.0, 30.3, 29.9, 29.6, 28.8, 26.72, 26.2. FT-IR (ATR): 3061, 2923, 2858, 1734, 1465, 1375, 1278, 1163, 1105, 1021, 976, 911, 827 cm^{-1} . HRMS (APCI) m/z : $[\text{M} + \text{H}]^+$ Calc'd for $\text{C}_{37}\text{H}_{65}\text{Br}_2\text{O}_6$ 765.3122; Found 765.3114.

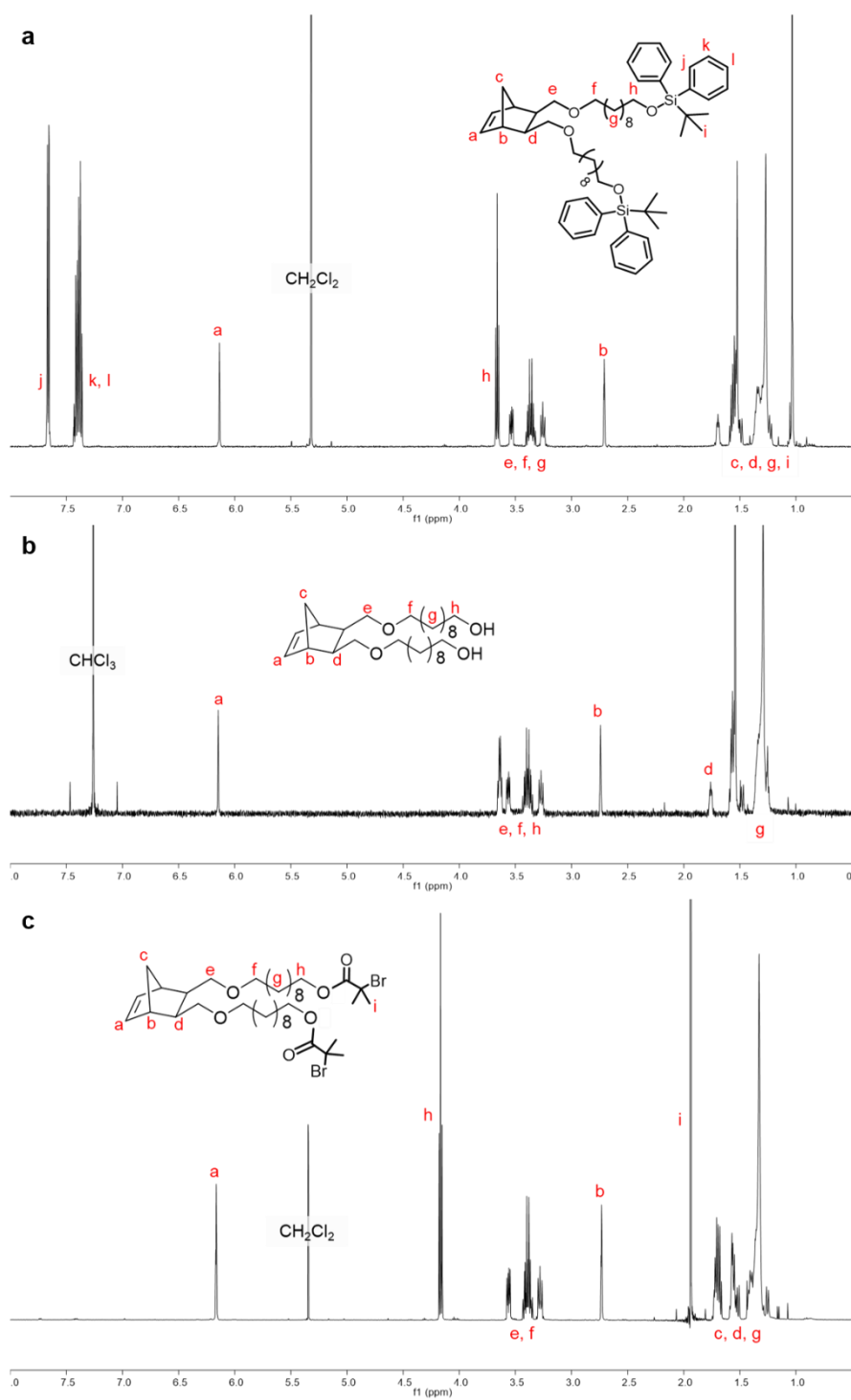


Figure 4.5. ^1H NMR (500 MHz) spectra of (a) **d-S2** (CD_2Cl_2), (b) **d-S3** (CDCl_3), and (c) **d-S4** (CD_2Cl_2).

Synthesis of d-MM1 (*exo*-5-norbornene-(dual-poly(*tert*-butyl acrylate)₁₁) (NB-d-tBA₁₁)). To a Schlenk flask equipped with a magnetic stirring bar dried with flame under the vacuum, were added *tert*-butyl acrylate (*t*BA) (5.89 g, 46.0 mmol), copper(I) bromide (Cu(I)Br) (16.0 mg, 111 μ mol), and *N,N,N',N'',N''*-pentamethyldiethylenetriamine (PMDETA) (21.5 mg, 124 μ mol), then were dissolved in 3 mL of anisole. The solution mixture was then deoxygenated through one cycles of freeze-pump-thaw and back-filled with N₂. To the resulting solution, was added the solution of *exo*-norbornene ATRP dual-initiator (**d-S4**) (35.1 mg, 45.9 μ mol (91.9 μ mol of Br end-groups)) in 3.7 mL of anisole. The reaction mixture then was deoxygenated through three cycles of freeze-pump-thaw and back-filled with N₂ before stirring at room temperature for 20 min to ensure homogeneity of the reaction mixture. The resulting homogeneous solution was stirred at 65 °C for 15.5 h. After 15.5 h, the polymerization was quenched by liquid N₂ and the solution was filtered through an Al₂O₃ (neutral)/celite column to remove Cu complex. The resulting eluent was concentrated to 10 mL solution and precipitated with 180 mL of cold methanol/water (v/v=6:4). The precipitates were collected by centrifugation and re-dissolved in 15 mL of THF. The resulting solution was precipitated with 180 mL of cold methanol/water (v/v=6:4) and collected by centrifugation. Resulting oil-like precipitates were washed with 120 mL of cold methanol/water (v/v=6:4) and dried under vacuum overnight (49 mg, 18% yield based upon ~ 2 % monomer conversion). $M_{n,SEC}$ = 3.4 kDa, D = 1.08. ¹H-NMR (500 MHz, CDCl₃) δ 6.16-6.12 (br t, NB **CH=CH**), 4.20-3.97 (br m, **CH₂OCO**), 3.62-3.20 (br m, NB-2,3-**CH₂OCH₂**), 2.77-2.72 (br quint, NB allylic **Hs**), 2.64-2.52 (br s, **CH₂s** from *t*BA

units), 2.41-2.08 (br m, CH_2s , CHs from *t*BA units), 2.07-0.70 (m, all CH_3s , CH_2s from dual-graft spacing moieties, CH_3s from *t*BA units, and CH_2s , 2,3- CHs from norbornene) ppm.

Synthesis of d-MM2 (*exo*-5-norbornene-dual-(poly(*tert*-butyl acrylate)₁₁-*b*-polystyrene₁₄) (NB-d-(PtBA₁₁-*b*-PS₁₄))). To a Schlenk flask equipped with a magnetic stirring bar dried with flame under the vacuum, was added the solution of **d-MM1** (49.0 mg, 14.4 μmol (28.8 μmol of Br end-groups)) and *N,N,N',N'',N''*-pentamethyldiethylenetriamine (PMDETA) (15.2 mg, 87.4 μmol) in styrene (4.20 g, 40.4 mmol; filtered through an Al_2O_3 /celite plug). The solution was then deoxygenated through two cycles of freeze-pump-thaw. To the frozen solution, was added copper(I) bromide (Cu(I)Br) (12.6 mg, 87.5 μmol) under N_2 flow. The reaction mixture then was deoxygenated through four cycles of freeze-pump-thaw and back-filled with N_2 before stirring at room temperature for 20 min to ensure homogeneity of the reaction mixture. The resulting homogeneous solution was stirred at 50 °C for 36 h. After 36 h, the polymerization was quenched by liquid N_2 and the solution was diluted with 5 mL of THF and filtered through an Al_2O_3 (neutral)/celite plug to remove Cu complex. The resulting eluent was precipitated with 180 mL of cold methanol/water (v/v=6:4). The precipitates were collected by centrifugation and re-dissolved in 10 mL of THF. The resulting solution was precipitated with 180 mL of cold methanol/water (v/v=6:4) and collected by centrifugation. Resulting precipitates were dried under vacuum overnight (43.0 mg, 43% yield based upon ~ 1.1 % monomer conversion). $M_{n,\text{SEC}} = 5.90$ kDa, $D = 1.01$. $^1\text{H-NMR}$ (500 MHz, CD_2Cl_2) δ 7.34-6.34 (br m, Ar Hs from PS units), 6.16-6.12 (br t, NB $\text{CH}=\text{CH}$),

4.64-4.35 (br m, CHs from PS units), 4.05-3.94 (br m, CH_2OCO), 3.56-3.21 (br m, NB-2,3- CH_2OCH_2), 2.74-2.69 (br quint, NB allylic Hs) 2.54-0.70 (br m, CH_3s , CH_2s CHs from $t\text{BA}$ units, CHs from PS units, all CH_3s , CH_2s from dual-graft spacing moieties, and CH_2s , 2,3- CHs from norbornene) ppm.

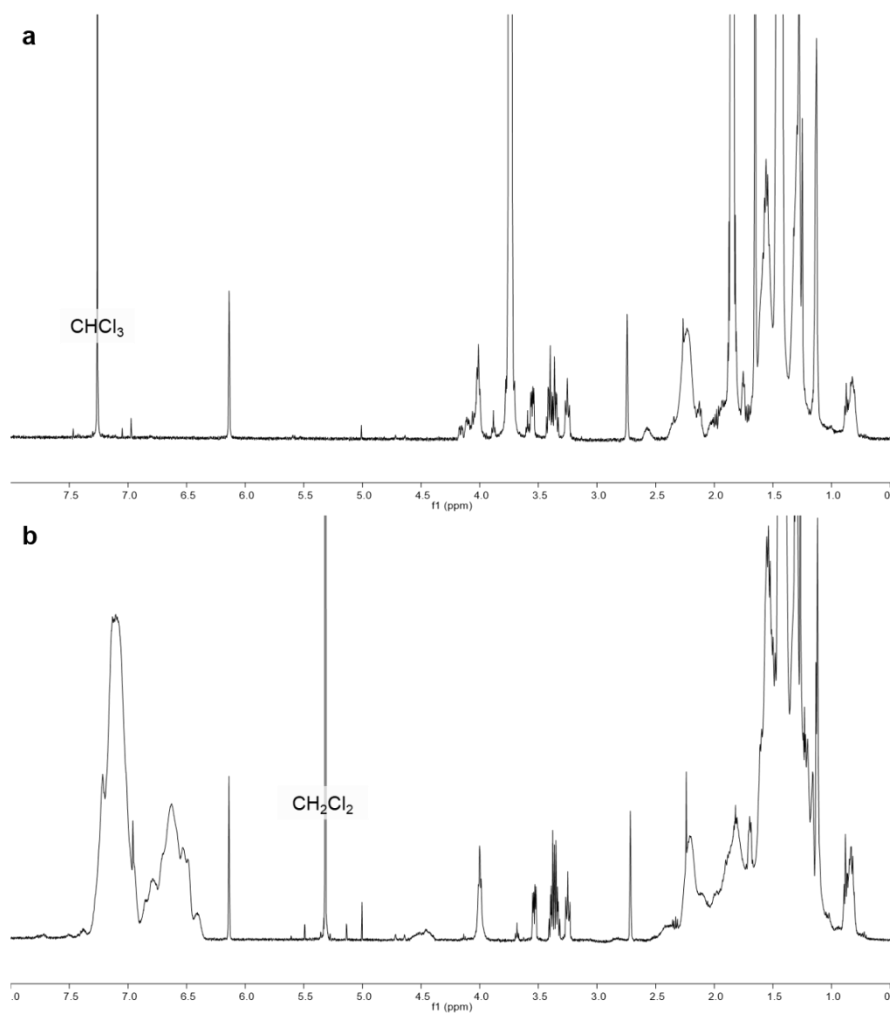
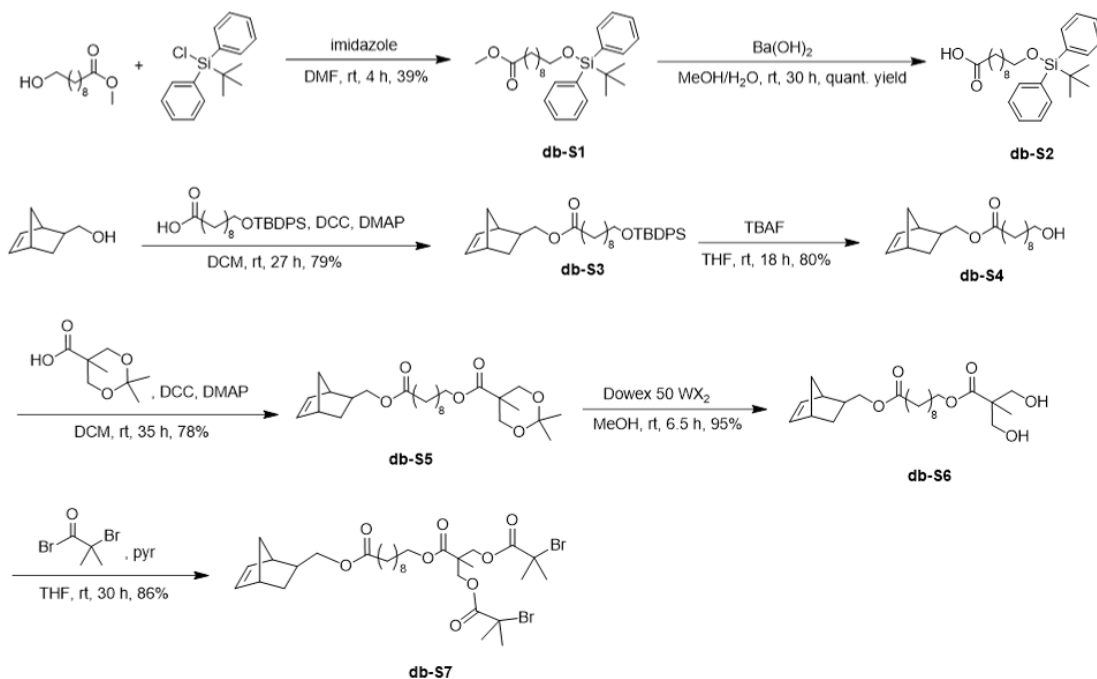


Figure 4.6. ^1H NMR (500 MHz) spectra of (a) **d-MM1** (CDCl_3), and (b) **d-MM2** (CD_2Cl_2).

Synthesis of d-BBP1 (poly[norbornene-graft-(dual-(poly(*tert*-butyl acrylate)₁₁-*b*-polystyrene₁₄))]₅₀ (P[NB-*g*-(d**-(PtA₁₁-*b*-PS₁₄))]₅₀)).** To a Schlenk flask equipped with a magnetic stir bar dried with flame under the reduced pressure, was added the solution of modified Grubbs catalyst (94.4 μg , 0.130 μmol) in 0.6 mL of anhydrous dichloromethane (CH_2Cl_2) and was deoxygenated through three cycles freeze-pump-thaw and back-filled with N_2 . To a deoxygenated catalyst solution, **d-MM2** (30.1 mg, 6.42 μmol ; in 0.5 mL of anhydrous CH_2Cl_2) solution (deoxygenated through two cycles of freeze-pump-thaw) was quickly added *via* an airtight syringe. The reaction solution was stirred at room temperature for 4.5 h, before quenching with 0.5 mL of ethyl vinyl ether (EVE)/ CH_2Cl_2 . The resulting mixture was stirred at room temperature for 2 h. The product was precipitated in 45 mL of cold MeOH/ H_2O (v/v=4:1) and collected by centrifugation. Collected product was re-dissolved into 1 mL of THF and precipitated in 48 mL of cold MeOH/ H_2O (v/v=4:1). Precipitates then were washed with 50 mL of cold MeOH/ H_2O (v/v=4:1) and dried under vacuum overnight (11.8 mg product, 42% mass yield, 20 % ROMP conversion).

B. Preparation of Double-chain Templating BBP

Scheme 4.4. Synthesis of double ATRP initiator (**db-S7**).



Preparation of db-S3. To a flask equipped with a stir bar, was added the solution of *exo*-5-norbornene-2-methanol (0.30 g, 2.42 mmol) and **db-S2** (1.25 g, 2.91 mmol) in 25 mL of anhydrous dichloromethane (CH₂Cl₂). To resulting solution, were added *N,N'*-dicyclohexylcarbodiimide (DCC) (600 mg, 2.91 mmol) and 4-dimethylaminopyridine (DMAP) (60 mg, 0.49 mmol). The reaction mixture was stirred at room temperature for 27 h. After 27 h, resulting mixture was filtered through a celite pad and the collected solution was filtered through PTFE filter (200 nm pore-size) to remove dicyclohexylurea (DCU). The resulting solution concentrated under the reduced pressure and purified by column chromatography (diethyl ether/hexane). The isolated product was concentrated

under the reduced pressure, yielding viscous liquid product (1.02 g, 79% yield). ^1H NMR (500 MHz, CDCl_3) δ 7.72–7.68 (4H, m; (*ortho*-) ArH), 7.45–7.38 (6H, m; (*meta*- and *para*-) ArH), 6.09 (2H, qd ($J = 5.6, 2.7$ Hz); NB CH=CH), 4.15 (1H, dd ($J = 10.9, 6.5$ Hz); NB-2-CH₂OCO), 3.97 (1H, dd ($J = 10.9, 9.1$ Hz); NB-2-CH₂OCO), 3.65 (2H, t ($J = 6.5$ Hz); (CH₂)₈CH₂OTBDPS), 2.84 (1H, br, NB allylic H), 2.68 (1H, br, NB allylic H), 2.32 (2H, t ($J = 7.5$ Hz); NB-2-CH₂OCOCH₂), 1.79–1.50 (8H, m; CHCH₂CH bridgehead, CH₂ from 3-position of NB, CH from 2-position of NB, NB-2-CH₂OCOCH₂CH₂, CH₂CH₂OTBDPS), 1.38–1.22 (11H, m; CH₂ from 3-position of NB, COCH₂CH₂(CH₂)₅CH₂CH₂OTBDPS), 1.05 (9H, s; CH₃ from TBDPS) ppm. ^{13}C NMR (126 MHz, CDCl_3) δ 174.5, 136.0, 134.9, 130.1, 129.1, 127.9, 66.4, 64.5, 43.5, 42.1, 41.8, 40.9, 33.2, 32.2, 30.1, 29.8, 29.7, 29.5, 29.2, 27.0, 26.5, 25.2, 19.4 ppm. HRMS (APCI) m/z : [M + H]⁺ Calc'd for C₃₄H₄₉O₃Si 533.3451; Found 533.3442.

Preparation of db-S4. To a flask equipped with a stir bar, was added the solution of **db-S3** (1.01 g, 1.89 mmol) in 10 mL of tetrahydrofuran (THF). To **db-S3** solution, was added tetrabutylammonium fluoride (TBAF) (1.0 M in THF, 7.56 mmol) and the resulting reaction mixture was stirred at room temperature for 18 h. The product was concentrated under the reduced pressure, yielding a colorless oil (420 mg, 75% yield). ^1H NMR (500 MHz, CDCl_3) δ 6.08 (2H, m; NB CH=CH), 4.14 (1H, dd ($J = 10.9, 6.5$ Hz); NB-2-CH₂OCO), 3.96 (1H, ddd ($J = 10.9, 9.1, 1.2$ Hz); NB-2-CH₂OCO), 3.63 (2H, t ($J = 6.6$ Hz); (CH₂)₈CH₂OH), 2.82 (1H, br; NB allylic H), 2.68 (1H, br; NB allylic H), 2.32 (2H, t ($J = 7.6$ Hz); NB-2-CH₂OCOCH₂), 1.73–1.10 (20H, m; CHCH₂CH bridgehead, CH₂ from 3-position of NB, CH from 2-position of NB, NB-2-CH₂OCOCH₂(CH₂)₇CH₂OH,

OH) ppm. ^{13}C NMR (126 MHz, CDCl_3) δ 174.2, 136.0, 66.5, 63.6, 43.4, 42.1, 41.8, 41.0, 33.5, 32.3, 29.9, 29.7, 29.6, 29.2, 28.9, 27.0, 25.9, 25.2 ppm. HRMS (ESI) m/z : $[\text{M} + \text{H}]^+$ Calc'd for $\text{C}_{18}\text{H}_{31}\text{O}_3$ 295.2273; Found 295.2270.

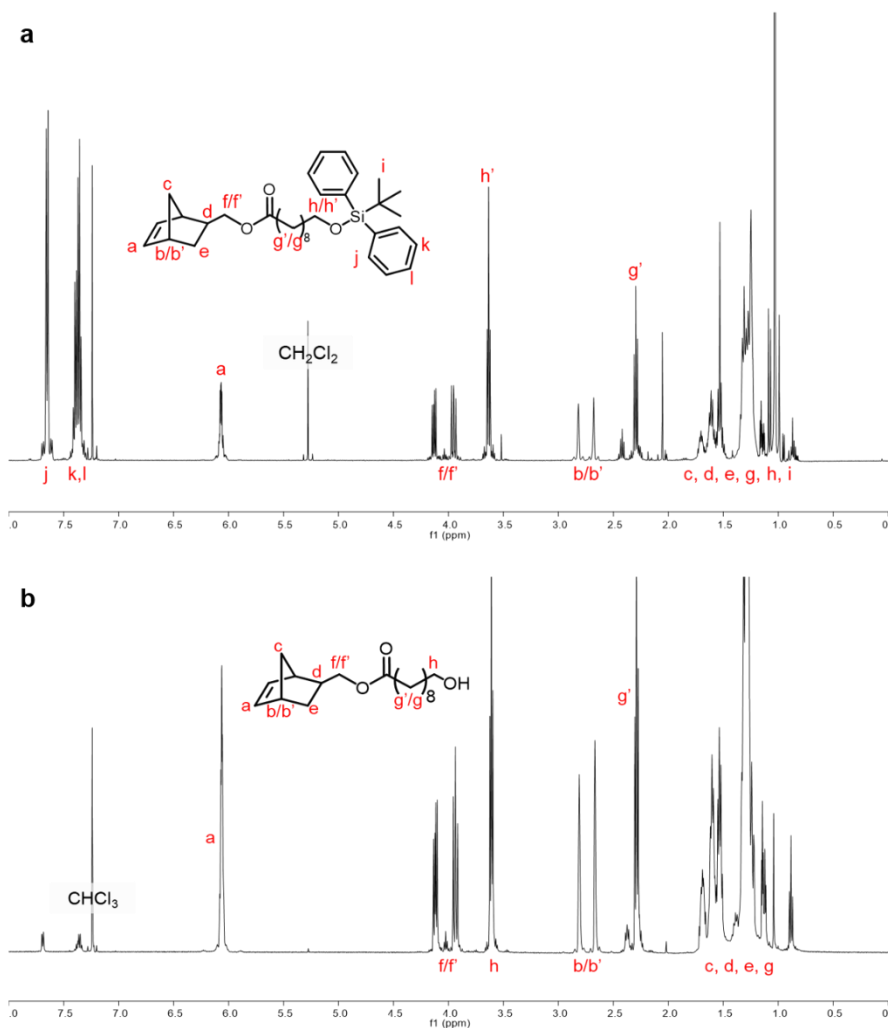


Figure 4.7. ^1H NMR (500 MHz) spectra of (a) **db-S3** (CD_2Cl_2), and (b) **db-S4** (CDCl_3).

Synthesis of db-S5. To a flask equipped with a stir bar, was added the solution of **db-S4** (0.41 g, 1.39 mmol) and 2,2,5-trimethyl-1,3-dioxane-5-carboxylic acid (TDC) (315

mg, 1.81 mmol) in 20 mL of anhydrous dichloromethane (CH_2Cl_2). To the resulting solution, were added *N,N'*-dicyclohexylcarbodiimide (DCC) (373 mg, 1.81 mmol) and 4-dimethyl aminopyridine (DMAP) (51 mg, 0.42 mmol). Then the reaction mixture was stirred at room temperature for 35 h. After 35h, the resulting solution was diluted with 30 mL of diethyl ether (Et_2O) and filtered through a celite pad. The collected solution was concentrated under the reduced pressure and the product was isolated by column chromatography (diethyl ether/hexane), yielding viscous liquid (480 mg, 78% yield). ^1H NMR (500 MHz, CDCl_3) δ 6.08 (2H, m; NB $\text{CH}=\text{CH}$), 4.20–3.90 (6H, m; NB-2- CH_2OCO , $(\text{CH}_2)_8\text{CH}_2\text{TDC}$, CH_2 of TDC unit (from C4 and C6 respectively), 3.64 (1H, s; CH_2 of TDC unit), 3.62 (1H, s; CH_2 of TDC unit), 2.83 (1H, br; NB allylic H), 2.69 (1H, br; NB allylic H), 2.31 (2H, td ($J = 7.5, 1.2$ Hz); NB-2- $\text{CH}_2\text{OCOCH}_2$), 1.71 (1H, m; CH from 2-position of NB), 1.67–1.58 (5H, m; 1H from CHCH_2CH bridgehead, $\text{CH}_2\text{CH}_2(\text{CH}_2)_5\text{CH}_2\text{CH}_2\text{TDC}$), 1.43–1.13 (22H, m; 1H from CHCH_2CH bridgehead, CH_2 from 3-position of NB, CHCH_2CH bridgehead, CH_2 from 3-position of NB, CH from 2-position of NB, $(\text{CH}_2)_2(\text{CH}_2)_5(\text{CH}_2)_2\text{TDC}$, CH_3 s from TDC unit) ppm. ^{13}C NMR (126 MHz, CDCl_3) δ 174.3, 173.6, 135.9, 98.1, 67.4, 66.8, 65.7, 45.0, 43.4, 42.0, 41.4, 41.1, 33.7, 29.9, 29.6, 29.5, 29.3, 29.2, 28.8, 27.2, 26.0, 25.9, 18.2 ppm. HRMS (ESI) m/z : $[\text{M} + \text{H}]^+$ Calc'd for $\text{C}_{26}\text{H}_{43}\text{O}_6$ 451.3060; Found 451.3052.

Synthesis of db-S6. To a flask equipped with a stir bar, was added a suspension of Dowex 50WX2 (400 mg) in 3 mL of methanol. To the suspension, was added the solution of **db-S5** (480 mg, 1.06 mmol) in 13 mL of methanol. The resulting mixture was stirred vigorously at room temperature for 6.5 h. The resin was filtered out after 6.5 h of

stirring and the filtrate was washed with methanol (10 mL) three times. The combined filtrates were concentrated under the reduced pressure and purified by column chromatography (ethyl acetate/hexane), yielding a colorless oil (0.42 g, 95% yield). ^1H NMR (500 MHz, CDCl_3) δ 6.08 (2H, m; NB $\text{CH}=\text{CH}$), 4.18–4.09 (3H, m; 1H from NB-2- CH_2OCO , 2Hs from $\text{OCO}(\text{C}(\text{CH}_3)(\text{CH}_2\text{OH})_2)$), 3.98–3.87 (3H, m; 1H from NB-2- CH_2OCO , $(\text{CH}_2)_8\text{CH}_2\text{OCO}(\text{C}(\text{CH}_3)(\text{CH}_2\text{OH})_2)$), 3.72 (1H, d ($J = 6.4$ Hz); 1H from $\text{OCO}(\text{C}(\text{CH}_3)(\text{CH}_2\text{OH})_2)$), 3.70 (1H, d ($J = 6.4$ Hz); 1H from $\text{OCO}(\text{C}(\text{CH}_3)(\text{CH}_2\text{OH})_2)$), 2.88–2.81 (3H, m; NB (C4) allylic H , OH s), 2.69 (1H, br m; NB (C1) allylic H), 2.31 (2H, t ($J = 7.5$ Hz); NB-2- $\text{CH}_2\text{OCOCH}_2$), 1.74–1.59 (6H, m; $\text{OCOCH}_2\text{CH}_2(\text{CH}_2)_5\text{CH}_2\text{CH}_2\text{O}$, CH from 2-position of NB, 1H from CHCH_2CH bridgehead), 1.39–1.23 (13H, m; 1H from CHCH_2CH bridgehead, 1H of CH_2 from 3-position of NB, $\text{OCO}(\text{CH}_2)_2(\text{CH}_2)_5(\text{CH}_2)_2\text{OCO}$), 1.39–1.23 (1H, m; 1H of CH_2 from 3-position of NB), 1.06 (3H, s, CH_3) ppm. ^{13}C NMR (126 MHz, CDCl_3) δ 174.4, 173.6, 135.9, 67.4, 65.7, 65.2, 47.0, 45.5, 43.4, 42.0, 41.4, 33.8, 29.9, 29.6, 29.5, 29.3, 29.2, 26.0, 25.2, 17.6 ppm. HRMS (ESI) m/z : $[\text{M} + \text{H}]^+$ Calc'd for $\text{C}_{23}\text{H}_{39}\text{O}_6$ 411.2747; Found 411.2744.

Synthesis of db-S7. To a flask equipped with a stir bar, were added the solution of **db-S6** (0.41 g, 995 μmol (1.99 mmol of alcohol end-groups)) in 25 mL of anhydrous tetrahydrofuran (THF), and pyridine (692 mg, 8.76 mmol). The resulting solution was stirred at room temperature for 5 min before adding the solution of α -Bromoisobutyryl bromide (BIBB) (916 mg, 3.98 mmol) in 5 mL of anhydrous THF. The reaction mixture was stirred at room temperature for 30 h. After 30 h, the resulting mixture was filtered through PTFE filter (200 nm pore-size) and the filtrate was concentrated under the reduced

pressure. The resulting concentrate was diluted with 40 mL of CH₂Cl₂, then washed with D.I. H₂O (20 mL) twice, followed by washing with brine (25 mL). The crude organic extracts were dried over sodium sulfate (Na₂SO₄) and the product was isolated by column chromatography (diethyl ether/hexane), yielding viscous liquid product (610 mg, 86% yield). ¹H NMR (500 MHz, CDCl₃) δ 6.08 (2H, m; NB **CH=CH**), 4.39 (2H, d (*J* = 11.0 Hz); OCO(C(CH₃)(CH₂O(α-BIB))₂)), 4.33 (2H, d (*J* = 11.0 Hz); OCO(C(CH₃)(CH₂O(α-BIB))₂)), 3.98–3.93 (3H, m; 1H from NB-2-CH₂OCO, (CH₂)₈CH₂OCO(C(CH₃)(CH₂O(α-BIB))₂)), 3.96 (1H, dd (*J* = 10.9, 9.2 Hz); 1H from NB-2-CH₂OCO), 2.83 (1H, br m; NB (C4) allylic **H**), 2.69 (1H, br m; NB (C1) allylic **H**), 2.31 (2H, t (*J* = 7.5 Hz); NB-2-CH₂OCOCH₂), 1.91 (12H, d (*J* = 13.0, 5.0 Hz); CH₃s from α-BIB units), 1.71 (1H, m; **CH** from 2-position of NB), 1.67–1.58 (4H, m; CHCH₂CH bridgehead, CH₂ from 3-position of NB), 1.37–1.23 (17H, br m; OCOCH₂(CH₂)₇CH₂OCO, OCO(C(CH₃)(CH₂O(α-BIB))₂)) ppm. ¹³C NMR (126 MHz, CDCl₃) δ 174.6, 173.6, 135.8, 67.4, 65.7, 65.2, 51.7, 51.6, 47.1, 45.5, 43.4, 42.0, 41.4, 33.9, 33.0, 32.9, 29.8, 29.6, 29.5, 29.2, 29.0, 26.0, 25.4, 17.5 ppm. HRMS (ESI) *m/z*: [M + H]⁺ Calc'd for C₃₁H₄₉O₈ 549.3427; Found 549.3425.

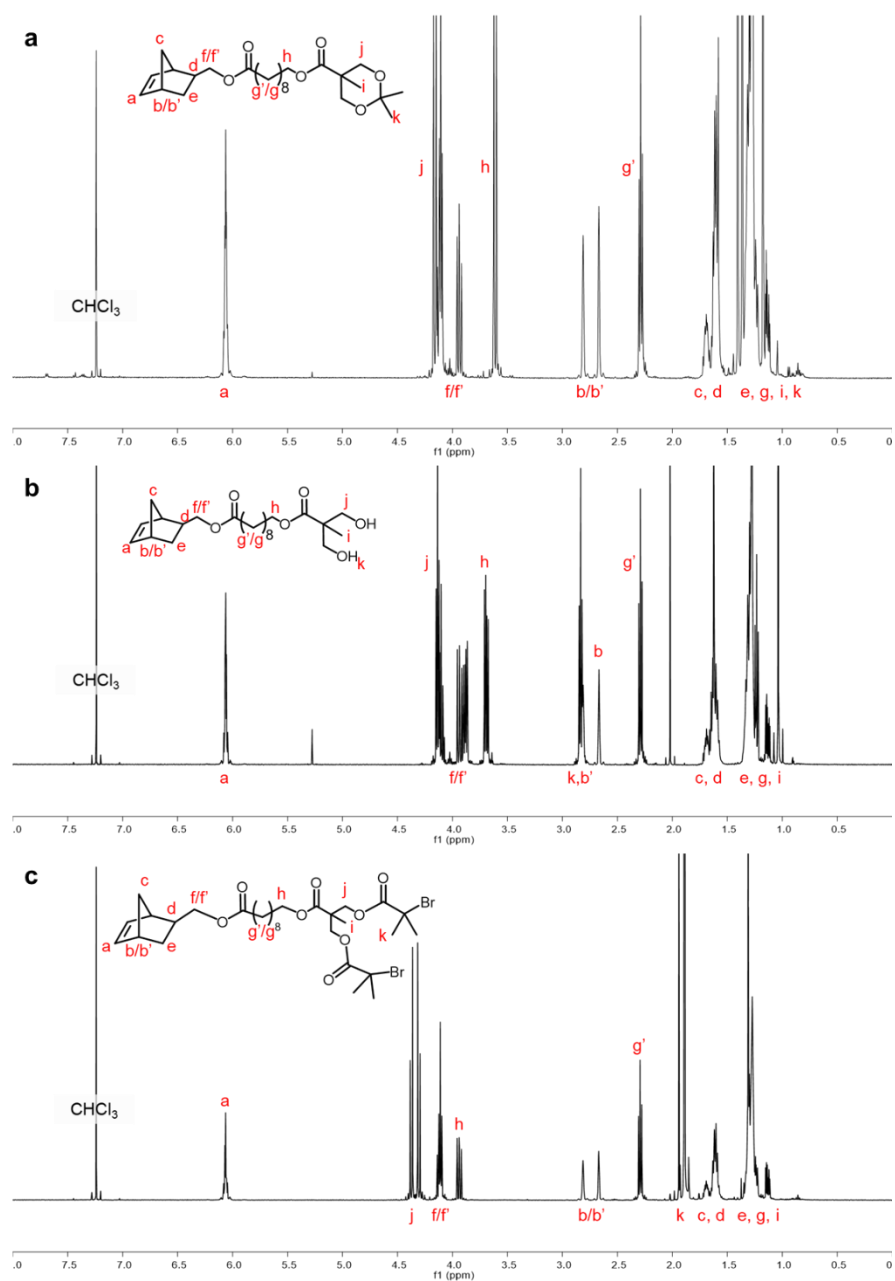


Figure 4.8. ^1H NMR (500 MHz, CDCl_3) spectra of (a) **db-S5**, (b) **d-S6**, and (c) **d-S7**.

Synthesis of db-MM1 (*exo*-5-norbornene-2-double-poly(*tert*-butyl acrylate)₂₇ (NB-db-tBA₂₇)). To a Schlenk flask equipped with a magnetic stirring bar dried with flame under the vacuum, were added *tert*-butyl acrylate (*tBA*) (24.7 g, 193 mmol),

copper(I) bromide (Cu(I)Br) (69.4 mg, 482 μmol), and *N,N,N',N'',N''*-pentamethyldiethylenetriamine (PMDETA) (90.2 mg, 522 μmol), then were dissolved in 24.5 mL of anisole. The solution mixture was then deoxygenated through two cycles of freeze-pump-thaw and back-filled with N_2 . To the resulting solution, was added the solution of *exo*-norbornene ATRP double-initiator (**db-S7**) (137 mg, 193 μmol (386 μmol of Br end-groups)) in 3 mL of anisole. The reaction mixture then was deoxygenated through four cycles of freeze-pump-thaw and back-filled with N_2 before stirring at room temperature for 20 min to ensure homogeneity of the reaction mixture. The resulting homogeneous solution was stirred at 65 °C for 13.5 h. After 13.5 h, the polymerization was quenched by liquid N_2 and the solution was filtered through an Al_2O_3 (neutral) column to remove Cu complex. The resulting eluent was concentrated to 10 mL solution and precipitated with 180 mL of cold methanol/water (v/v=6:4). The precipitates were collected by centrifugation and re-dissolved in 12 mL of THF. The resulting solution was precipitated with 180 mL of cold methanol/water (v/v=6:4) and collected by centrifugation. Resulting precipitates were washed with 120 mL of cold methanol/water (v/v=6:4) and dried under vacuum overnight (52% yield based upon ~ 6 % monomer conversion). $M_{n,\text{SEC}} = 6.7 \text{ kDa}$, $\mathcal{D} = 1.10$. $M_{n,\text{NMR}} = 7.6 \text{ kDa}$. $^1\text{H-NMR}$ (500 MHz, CDCl_3) δ 6.08-6.03 (m, NB **CH=CH**), 4.23-3.89 (br m, $\text{OCO}(\text{C}(\text{CH}_3)(\text{CH}_2\text{O}(\alpha\text{-BIB}))_2)$), NB-2-**CH₂OCO**), 2.82 (br s, NB (C4) allylic **H**), 2.70 (br s, NB (C1) allylic **H**), 2.47-0.58 (m, all **CH₃s**, **CH₂s** from double-graft spacing moieties, **CH₃s** from *t*BA units, and **CH₂s**, 2,3-**CHs** from norbornene) ppm.

Synthesis of db-MM2 (*exo*-5-norbornene-2-double-(poly(*tert*-butyl acrylate)₂₇-*b*-polystyrene₂₅) (NB-db-(PtBA₂₇-*b*-PS₂₅))). To a Schlenk flask equipped with a magnetic stirring bar dried with flame under the vacuum, was added the solution of **db-MM1** (341 mg, 44.8 μmol (89.5 μmol of Br end-groups)) and *N,N,N',N'',N''*-pentamethyldiethylenetriamine (PMDETA) (46.5 mg, 269 μmol) in styrene (8.01 g, 77.0 mmol; filtered through an Al₂O₃/celite plug). The solution was then deoxygenated through two cycles of freeze-pump-thaw. To the frozen solution, was added copper(I) bromide (Cu(I)Br) (38.7 mg, 269 μmol) under N₂ flow. The reaction mixture then was deoxygenated through four cycles of freeze-pump-thaw and back-filled with N₂ before stirring at room temperature for 20 min to ensure homogeneity of the reaction mixture. Resulting homogeneous solution was stirred at 50 °C for 31 h 50 min. After 31 h 50 min, the polymerization was quenched by liquid N₂ and the solution was diluted with 10 mL of THF and filtered through an Al₂O₃ (neutral)/celite plug to remove Cu complex. The resulting eluent was concentrated and diluted with 5 mL of THF and precipitated with 180 mL of cold methanol/water (v/v=1:1). The precipitates were collected by centrifugation and re-dissolved in 15 mL of THF. The resulting solution was precipitated with 180 mL of cold methanol/water (v/v=1:1) and collected by centrifugation. Resulting precipitates were washed with 200 mL of cold methanol/water (v/v=1:1) and dried under vacuum overnight (78% yield based upon ~ 3 % monomer conversion). $M_{n,SEC} = 11.1 \text{ kDa}$, $\mathcal{D} = 1.12$. ¹H-NMR (500 MHz, CD₂Cl₂) δ 7.39-6.35 (br m, Ar **H**s from PS units), 6.15-6.07 (br t, NB **CH=CH**), 4.73-4.31 (br m, **CH**s from PS units), 4.25-3.91 (br m, **CH**₂OCO), 2.83 (br s, NB (C4) allylic **H**), 2.70 (br s, NB (C1) allylic **H**), 2.53-0.78 (m, br m, **CH**₃s,

CH_2 s CH s from *t*BA units, CH s from PS units, all CH_3 s, CH_2 s from double-graft spacing moieties, and CH_2 s, 2,3- CH s from norbornene) ppm.

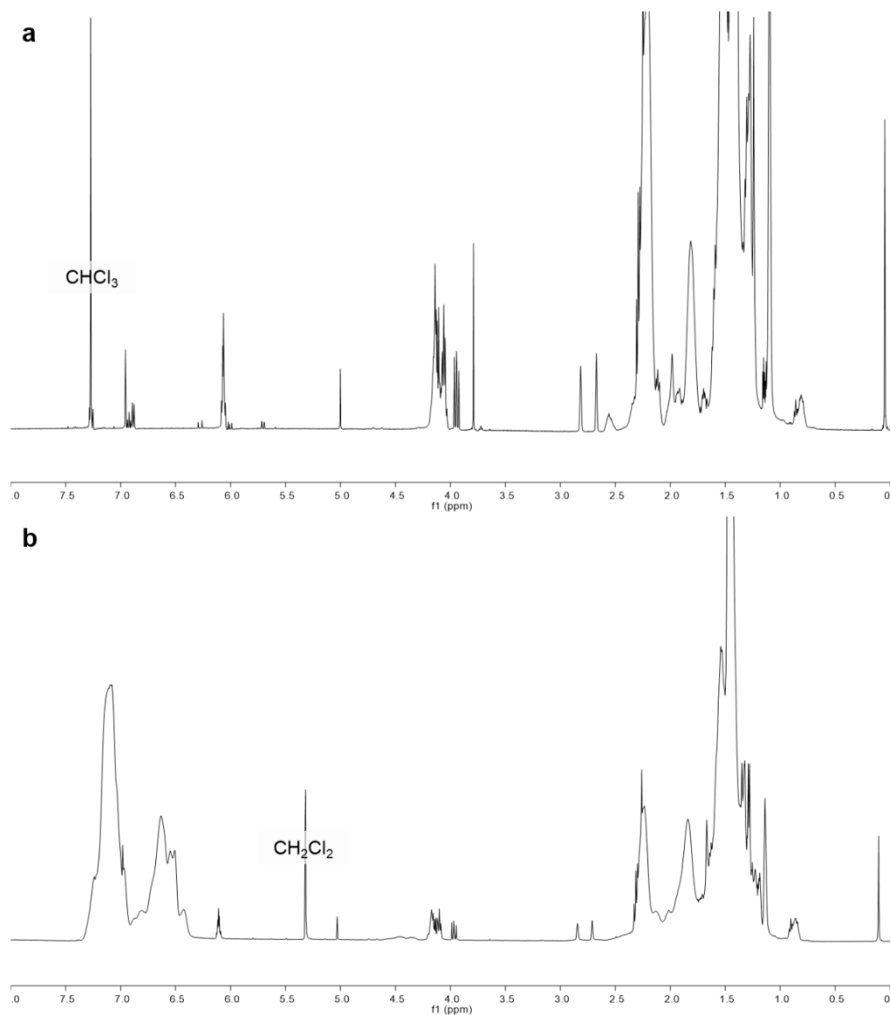


Figure 4.9. 1H NMR (500 MHz) spectra of (a) **db-MM1** ($CDCl_3$), and (b) **db-MM2** (CD_2Cl_2).

Synthesis of db-BBP1 (poly[norbornene-*graft*-(double-(poly(*tert*-butyl acrylate)₂₇-*b*-polystyrene)₂₅))]₅₀ (P[NB-*g*-db-(PtBA₂₇-*b*-PS₂₅)]₅₀). To a Schlenk flask equipped with a magnetic stir bar dried with flame under the reduced pressure, was added

the solution of modified Grubbs catalyst (230 μg , 0.313 μmol) in 0.2 mL of anhydrous dichloromethane (CH_2Cl_2) and was deoxygenated through three cycles freeze-pump-thaw and back-filled with N_2 . To a deoxygenated catalyst solution, **db-MM2** (200 mg, 15.6 μmol ; in 1.8 mL of anhydrous CH_2Cl_2) solution (deoxygenated through two cycles of freeze-pump-thaw) was quickly added *via* an airtight syringe. The reaction solution was stirred at room temperature for 3 h, before quenching with 0.4 mL of ethyl vinyl ether (EVE)/ CH_2Cl_2 . The resulting mixture was stirred at room temperature for 1.5 h. The solvent was removed under the reduced pressure and the resulting crude product was dissolved in 2 mL of THF. The product was precipitated in 45 mL of cold MeOH/ H_2O (v/v=4:1) and collected by centrifugation. Collected product was washed with 50 mL of cold MeOH/ H_2O (v/v=4:1) twice and dried under vacuum overnight (89% yield, > 90 % ROMP conversion). $^1\text{H-NMR}$ (500 MHz, CD_2Cl_2) δ 7.36-6.31 (br m, Ar **H**s from PS units), 4.61-3.92 (br m, $\text{CH}_2\text{CH}_2\text{O}$, **CH**s from PS units), 2.58-2.06 (br m, **CHCOO**, CH_2 from PS units), 2.05-1.71 (br, **CH**s from backbone polymer, **CH**s from *Pt*BA units), 1.69-1.50 (m, CH_2 s from backbone polymer), 1.50-1.35 (s, CH_3 s from *Pt*BA units), 1.34-1.01 (m, CH_3 s from dual chains, CH_2 s from *Pt*BA units, CH_2 s from backbone polymer), 0.95-0.78 (br m, CH_3 s from dimethyl groups) ppm.

Synthesis of db-BBP2 (poly[norbornene-*graft*-(double-(poly(acrylic acrylate)_{27-b}-polystyrene₂₅))]₅₀ (P[NB-*g*-db-(PAA_{27-b}-PS₂₅)]₅₀)). To a flask equipped with a magnetic stir bar, was added the solution of **db-BBP1** brush polymer (100 mg, 211 μmol (422 μmol of *t*BA groups)) in 1.5 mL of CH_2Cl_2 . To a **db-BBP1** brush polymer solution, was added trifluoroacetic acid (TFA) (2.40 g, 21.1 mmol). The turbid reaction

mixture was stirred at room temperature for 53 h. After 53 h, the solution was precipitated with 45 mL of Et₂O and the precipitates were collected by centrifugation. Resulting precipitates were washed with 50 mL of Et₂O three times and dried under vacuum overnight (68% yield based upon 640 kDa of **db-BBP1** molecular weight). ¹H-NMR (500 MHz, DMSO-*d*₆) δ 12.51-11.86, (br s, COOH), 8.54-5.25, 4.16-0.16 ppm.

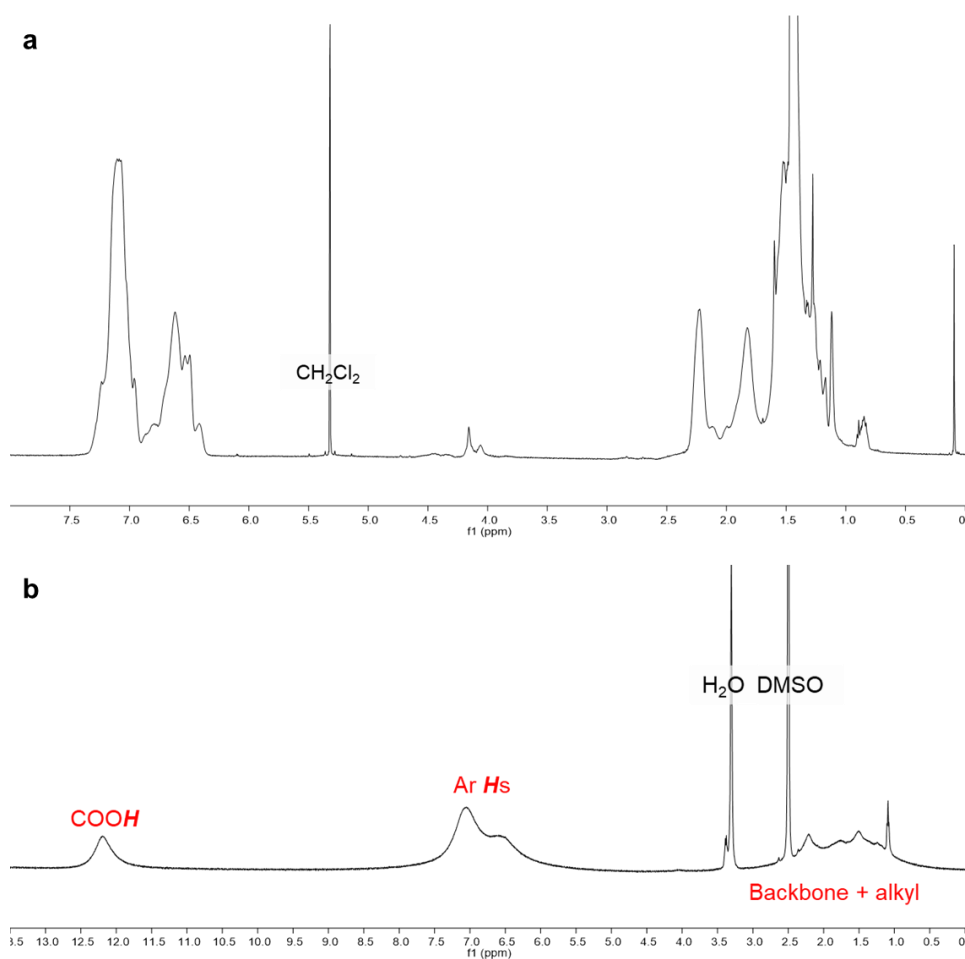


Figure 4.10. ¹H NMR (500 MHz) spectra of (a) **db-BBP1** (CD₂Cl₂), and (b) **db-BBP2** (DMSO-*d*₆).

CHAPTER V

CONCLUSIONS

This dissertation presents diverse facets of BBPs with different functionalities and applications. Each research topic encompasses several aspects of the newly designed BBP systems, including synthetic strategies for precise control of chemical compositions and dimensions, chemical and physical properties at both microscopic and macroscopic scales, and their potential applications. By the combination of controlled radical polymerizations and olefin metathesis polymerization, BBPs were prepared *via* a “grafting-through” approach which enables a high degree of control in their lengthwise and widthwise dimensions, as well as their chemical compositions at targeted positions within the BBP structure. The material properties of prepared BBP systems were explored by many characterization tools, such as AFM, SIMS, GIWAXS, GISAXS, and SEM, to name a few. In each design for a specific application, unique properties of BBPs were introduced by the functional groups of selected monomer building blocks and/or macromonomer frameworks to exhibit desired performances for the corresponding application.

In Chapter II, a thin layer of assembled BBPs consisting of hole transporting functionalities was fabricated for use as an HTL in the multilayered OLED application. The aim of the hole transporting (HT) BBPs design was to improve the “face-on” packing alignments of HT functional groups, triphenylamines (TPAs), to the substrate which would enhance the OLED performances by maximizing π - π overlappings and facilitating the movement of holes within the HTL. Horizontal alignments of TPAs were achieved by

applying topological strategy—the vertical alignment of BBPs—upon spin-casting of prepared HT BBP solutions with appropriate concentrations to obtain a monolayered film. The vertical alignment of the BBP assembly within the spin-cast thin film was accomplished by employing a surface energy reducing moiety, or F-enriched moiety, located at one-side of the BBP backbone. As a result, the block of backbone polymer including surface energy reducing groups faced towards the air-film interface and induced the vertical alignment of BBP backbones within an HTL thin film. The set of HT BBPs was synthesized to optimize the compositional and dimensional ratio and the selected HT BBPs were applied to fabricate OLED devices. The OLED performances of HT BBPs compared to linear HT polymers and commercial HT polymers, TFB, showed enhanced device performances, in terms of current density, power, and external quantum efficiencies.

For the project in Chapter III, the BBP was applied as a sacrificial porogen to fabricate porous polymer membranes for gas separation applications. The key concept of the designed porous polymer membrane herein is the “phototriggered porogenesis process” by utilizing the chemistry of contrast tones of CAR, positive-tone and negative-tone photoresists. The modulation of solubilities of these two photoresists by phototriggered reactions allows one type of CAR, a positive-tone resist, to be removed by dissolution into a developer, while a negative-tone CAR is crosslinked to retain their positions in a membrane. Using these combinational effects, pores were generated with a UV lithographic process of the cast membranes prepared with sacrificial BBPs and negative-tone matrix polymers. The porous morphologies of the prepared materials were

confirmed by SEM imaging and this membrane exhibited enhanced selective gas adsorption for CO₂ over N₂ over the control membrane sample with no porous features.

Lastly, in Chapter IV, the potential of amphiphilic BBPs having cylindrical shapes with a longer axis than the diameter were explored as templating agents for nanorod growth. To ensure the anisotropic shape of BBPs with minimized flexibility, we designed the synthesis of dual- and double-grafted BBPs. However, the designed dual-chain BBP could not be prepared due to several issues during the synthetic process that is still under investigation. On the other hand, the double-grafted BBPs were successfully synthesized and used for further exploration of the morphology and chemical structure relationships. The molecular morphologies of double-grafted BBPs were analyzed by AFM characterization and double-grafted BBPs displayed anisotropic polymer shapes with a certain degree of rigidity, giving promise of future applications of densely grafted BBPs for assisting the growth of inorganic nanorods.

Potentials of BBPs are attributed not only to their molecular architectures but also to the effect of their topological arrangements in solid-states and/or thin-film states. By using these topologically advantageous facets of BBPs in addition to the ability to precisely control their chemical compositions and molecular dimensions, it is expected to open up more fields of BBP applications for advanced technologies.

REFERENCES

1. Schaeffgen, J. R.; Flory, P. J., Synthesis of Multichain Polymers and Investigation of their Viscosities. *Journal of the American Chemical Society* **1948**, *70* (8), 2709-2718.
2. Mojzesz, S. M. N., Roper A.; Emil, Steiner H. M. Production of polymers from aromatic and the like compounds. 1952.
3. Percec, V.; Heck, J.; Lee, M.; Ungar, G.; Alvarez-Castillo, A., Poly{2-vinyloxyethyl 3,4,5-tris[4-(n-dodecanyloxy)benzyloxy]benzoate}: a self-assembled supramolecular polymer similar to tobacco mosaic virus. *Journal of Materials Chemistry* **1992**, *2* (10), 1033-1039.
4. Masson, P.; Franta, E.; Rempp, P., Synthèse et homopolymérisation de macromères de polystyrène. *Die Makromolekulare Chemie, Rapid Communications* **1982**, *3* (7), 499-504.
5. Rempp, P.; Lutz, P.; Masson, P.; Chaumont, P., Macromonomers: A new class of polymeric intermediates in macromolecular synthesis - II - homo- and copolymerization. *Die Makromolekulare Chemie* **1985**, *13* (S19851), 47-66.
6. Buhleier, E.; Wehner, W.; VÖGtle, F., "Cascade"- and "Nonskid-Chain-like" Syntheses of Molecular Cavity Topologies. *Synthesis* **1978**, *1978* (02), 155-158.
7. Stanford, J. L.; Stepto, R. F. T.; Waywell, D. R., Rate theory of irreversible linear random polymerisation. Part 2.—Application to intramolecular reaction in A—A + B—B type polymerisations. *Journal of the Chemical Society, Faraday Transactions 1: Physical Chemistry in Condensed Phases* **1975**, *71* (0), 1308-1326.
8. Gordon, M.; Temple, W. B., Ring-chain competition kinetics in linear polymers. *Die Makromolekulare Chemie* **1972**, *152* (1), 277-289.
9. Wooley, K. L., From Dendrimers to Knedel-like Structures. *Chemistry – A European Journal* **1997**, *3* (9), 1397-1399.
10. Kakkar, A.; Traverso, G.; Farokhzad, O. C.; Weissleder, R.; Langer, R., Evolution of macromolecular complexity in drug delivery systems. *Nature Reviews Chemistry* **2017**, *1* (8), 0063.
11. Pan, D.; Turner, J. L.; Wooley, K. L., Folic acid-conjugated nanostructured materials designed for cancer cell targeting. *Chemical Communications* **2003**, (19), 2400-2401.

12. Koji, M.; Akinori, K.; Kazuaki, O.; Yoshiaki, K.; Hideki, M.; Hiroshi, H.; Masahiro, H.; Kouichi, O., High-Contrast Fluorescence Imaging of Tumors In Vivo Using Nanoparticles of Amphiphilic Brush-Like Copolymers Produced by ROMP. *Angewandte Chemie International Edition* **2011**, *50* (29), 6567-6570.
13. Adhikari, B.; Majumdar, S., Polymers in sensor applications. *Progress in Polymer Science* **2004**, *29* (7), 699-766.
14. Kumar, V.; Maiti, B.; Chini, M. K.; De, P.; Satapathi, S., Multimodal Fluorescent Polymer Sensor for Highly Sensitive Detection of Nitroaromatics. *Scientific Reports* **2019**, *9* (1), 7269.
15. Park, J.; Ahn, D. B.; Kim, J.; Cha, E.; Bae, B.-S.; Lee, S.-Y.; Park, J.-U., Printing of wirelessly rechargeable solid-state supercapacitors for soft, smart contact lenses with continuous operations. *Science Advances* **2019**, *5* (12), eaay0764.
16. He, Z.; Zhang, Z.; Asare-Yeboah, K.; Bi, S., Poly(α -methylstyrene) polymer and small-molecule semiconductor blend with reduced crystal misorientation for organic thin film transistors. *Journal of Materials Science: Materials in Electronics* **2019**, *30* (15), 14335-14343.
17. Huang, F.; Cheng, Y.-J.; Zhang, Y.; Liu, M. S.; Jen, A. K. Y., Crosslinkable hole-transporting materials for solution processed polymer light-emitting diodes. *Journal of Materials Chemistry* **2008**, *18* (38), 4495-4509.
18. Facchetti, A., Polymer donor–polymer acceptor (all-polymer) solar cells. *Materials Today* **2013**, *16* (4), 123-132.
19. Sun, G.; Cho, S.; Clark, C.; Verkhoturov, S. V.; Eller, M. J.; Li, A.; Pavía-Jiménez, A.; Schweikert, E. A.; Thackeray, J. W.; Trefonas, P.; Wooley, K. L., Nanoscopic Cylindrical Dual Concentric and Lengthwise Block Brush Terpolymers as Covalent Preassembled High-Resolution and High-Sensitivity Negative-Tone Photoresist Materials. *Journal of the American Chemical Society* **2013**, *135* (11), 4203-4206.
20. Cho, S.; Yang, F.; Sun, G.; Eller, M. J.; Clark, C.; Schweikert, E. A.; Thackeray, J. W.; Trefonas, P.; Wooley, K. L., Directing Self-Assembly of Nanoscopic Cylindrical Diblock Brush Terpolymers into Films with Desired Spatial Orientations: Expansion of Chemical Composition Scope. *Macromolecular Rapid Communications* **2014**, *35* (4), 437-441.
21. Sun, G.; Cho, S.; Yang, F.; He, X.; Pavía-Sanders, A.; Clark, C.; Raymond, J. E.; Verkhoturov, S. V.; Schweikert, E. A.; Thackeray, J. W.; Trefonas, P.; Wooley, K. L., Advanced photoresist technologies by intricate molecular brush architectures: Diblock

brush terpolymer-based positive-tone photoresist materials. *Journal of Polymer Science Part A: Polymer Chemistry* **2015**, *53* (2), 193-199.

22. Zhang, B.; Gröhn, F.; Pedersen, J. S.; Fischer, K.; Schmidt, M., Conformation of Cylindrical Brushes in Solution: Effect of Side Chain Length. *Macromolecules* **2006**, *39* (24), 8440-8450.

23. Hu, M.; Xia, Y.; McKenna, G. B.; Kornfield, J. A.; Grubbs, R. H., Linear Rheological Response of a Series of Densely Branched Brush Polymers. *Macromolecules* **2011**, *44* (17), 6935-6943.

24. Cheng, C.; Qi, K.; Khoshdel, E.; Wooley, K. L., Tandem Synthesis of Core-Shell Brush Copolymers and Their Transformation to Peripherally Cross-Linked and Hollowed Nanostructures. *Journal of the American Chemical Society* **2006**, *128* (21), 6808-6809.

25. Cheng, C.; Khoshdel, E.; Wooley, K. L., ATRP from a Norbornenyl-Functionalized Initiator: Balancing of Complementary Reactivity for the Preparation of α -Norbornenyl Macromonomers/ ω -Haloalkyl Macroinitiators. *Macromolecules* **2005**, *38* (23), 9455-9465.

26. Ma, J.; Cheng, C.; Wooley, K. L., The Power of RAFT for Creating Polymers Having Imbedded Side-Chain Functionalities: Norbornenyl-Functionalized Polymers and their Transformations via ROMP and Thiol-ene Reactions. *Australian Journal of Chemistry* **2009**, *62* (11), 1507-1519.

27. Matyjaszewski, K.; Spanswick, J., Controlled/living radical polymerization. *Materials Today* **2005**, *8* (3), 26-33.

28. Jha, S.; Dutta, S.; Bowden, N. B., Synthesis of Ultralarge Molecular Weight Bottlebrush Polymers Using Grubbs' Catalysts. *Macromolecules* **2004**, *37* (12), 4365-4374.

29. Cheng, C.; Khoshdel, E.; Wooley, K. L., Facile One-Pot Synthesis of Brush Polymers through Tandem Catalysis Using Grubbs' Catalyst for Both Ring-Opening Metathesis and Atom Transfer Radical Polymerizations. *Nano Letters* **2006**, *6* (8), 1741-1746.

30. Xia, Y.; Kornfield, J. A.; Grubbs, R. H., Efficient Synthesis of Narrowly Dispersed Brush Polymers via Living Ring-Opening Metathesis Polymerization of Macromonomers. *Macromolecules* **2009**, *42* (11), 3761-3766.

31. Li, Z.; Zhang, K.; Ma, J.; Cheng, C.; Wooley, K. L., Facile syntheses of cylindrical molecular brushes by a sequential RAFT and ROMP "grafting-through"

methodology. *Journal of Polymer Science Part A: Polymer Chemistry* **2009**, *47* (20), 5557-5563.

32. Li, A.; Ma, J.; Sun, G.; Li, Z.; Cho, S.; Clark, C.; Wooley, K. L., One-pot, facile synthesis of well-defined molecular brush copolymers by a tandem RAFT and ROMP, "Grafting-through" strategy. *J. of Polym. Sci., Part A: Polym. Chem.* **2012**, *50* (9), 1681-1688.

33. Bielawski, C. W.; Grubbs, R. H., Living ring-opening metathesis polymerization. *Progress in Polymer Science* **2007**, *32* (1), 1-29.

34. Choi, T.-L.; Grubbs, R. H., Controlled Living Ring-Opening-Metathesis Polymerization by a Fast-Initiating Ruthenium Catalyst. *Angewandte Chemie International Edition* **2003**, *42* (15), 1743-1746.

35. Yokoyama, D., Molecular orientation in small-molecule organic light-emitting diodes. *Journal of Materials Chemistry* **2011**, *21* (48), 19187-19202.

36. Brütting, W.; Frischeisen, J.; Schmidt, T. D.; Scholz, B. J.; Mayr, C., Device efficiency of organic light-emitting diodes: Progress by improved light outcoupling. *physica status solidi (a)* **2013**, *210* (1), 44-65.

37. Fung, M.-K.; Li, Y.-Q.; Liao, L.-S., Tandem Organic Light-Emitting Diodes. *Advanced Materials* **2016**, *28* (47), 10381-10408.

38. Schmidt, T. D.; Lampe, T.; Sylvinson M. R, D.; Djurovich, P. I.; Thompson, M. E.; Brütting, W., Emitter Orientation as a Key Parameter in Organic Light-Emitting Diodes. *Physical Review Applied* **2017**, *8* (3), 037001.

39. Kim, K.-H.; Kim, J.-J., Origin and Control of Orientation of Phosphorescent and TADF Dyes for High-Efficiency OLEDs. *Advanced Materials* **2018**, *30* (42), 1705600.

40. Ediger, M. D.; de Pablo, J.; Yu, L., Anisotropic Vapor-Deposited Glasses: Hybrid Organic Solids. *Accounts of Chemical Research* **2019**, *52* (2), 407-414.

41. Salehi, A.; Fu, X.; Shin, D.-H.; So, F., Recent Advances in OLED Optical Design. *Advanced Functional Materials* **2019**, *29* (15), 1808803.

42. Watanabe, Y.; Sasabe, H.; Kido, J., Review of Molecular Engineering for Horizontal Molecular Orientation in Organic Light-Emitting Devices. *Bulletin of the Chemical Society of Japan* **2019**, *92* (3), 716-728.

43. Yokoyama, D.; Sakaguchi, A.; Suzuki, M.; Adachi, C., Horizontal molecular orientation in vacuum-deposited organic amorphous films of hole and electron transport materials. *Applied Physics Letters* **2008**, *93* (17), 173302.

44. Yokoyama, D.; Sakaguchi, A.; Suzuki, M.; Adachi, C., Horizontal orientation of linear-shaped organic molecules having bulky substituents in neat and doped vacuum-deposited amorphous films. *Organic Electronics* **2009**, *10* (1), 127-137.
45. Kim, J. Y.; Yokoyama, D.; Adachi, C., Horizontal Orientation of Disk-like Hole Transport Molecules and Their Application for Organic Light-Emitting Diodes Requiring a Lower Driving Voltage. *The Journal of Physical Chemistry C* **2012**, *116* (15), 8699-8706.
46. Kim, J. Y.; Yasuda, T.; Yang, Y. S.; Adachi, C., Bifunctional Star-Burst Amorphous Molecular Materials for OLEDs: Achieving Highly Efficient Solid-State Luminescence and Carrier Transport Induced by Spontaneous Molecular Orientation. *Advanced Materials* **2013**, *25* (19), 2666-2671.
47. Wakamiya, A.; Nishimura, H.; Fukushima, T.; Suzuki, F.; Saeki, A.; Seki, S.; Osaka, I.; Sasamori, T.; Murata, M.; Murata, Y.; Kaji, H., On-Top π -Stacking of Quasipolar Molecules in Hole-Transporting Materials: Inducing Anisotropic Carrier Mobility in Amorphous Films. *Angewandte Chemie International Edition* **2014**, *53* (23), 5800-5804.
48. Gujral, A.; O'Hara, K. A.; Toney, M. F.; Chabynyc, M. L.; Ediger, M. D., Structural Characterization of Vapor-Deposited Glasses of an Organic Hole Transport Material with X-ray Scattering. *Chemistry of Materials* **2015**, *27* (9), 3341-3348.
49. Wu, C.-c.; Liu, T.-L.; Hung, W.-Y.; Lin, Y.-T.; Wong, K.-T.; Chen, R.-T.; Chen, Y.-M.; Chien, Y.-Y., Unusual Nondispersive Ambipolar Carrier Transport and High Electron Mobility in Amorphous Ter(9,9-diarylfuorene)s. *Journal of the American Chemical Society* **2003**, *125* (13), 3710-3711.
50. Yokoyama, D.; Sakaguchi, A.; Suzuki, M.; Adachi, C., Enhancement of electron transport by horizontal molecular orientation of oxadiazole planar molecules in organic amorphous films. *Applied Physics Letters* **2009**, *95* (24), 243303.
51. Yokoyama, D.; Setoguchi, Y.; Sakaguchi, A.; Suzuki, M.; Adachi, C., Orientation Control of Linear-Shaped Molecules in Vacuum-Deposited Organic Amorphous Films and Its Effect on Carrier Mobilities. *Advanced Functional Materials* **2010**, *20* (3), 386-391.
52. Yokoyama, D.; Sasabe, H.; Furukawa, Y.; Adachi, C.; Kido, J., Molecular Stacking Induced by Intermolecular C-H \cdots N Hydrogen Bonds Leading to High Carrier Mobility in Vacuum-Deposited Organic Films. *Advanced Functional Materials* **2011**, *21* (8), 1375-1382.
53. Watanabe, Y.; Sasabe, H.; Yokoyama, D.; Beppu, T.; Katagiri, H.; Pu, Y.-J.; Kido, J., Simultaneous Manipulation of Intramolecular and Intermolecular Hydrogen

Bonds in n-Type Organic Semiconductor Layers: Realization of Horizontal Orientation in OLEDs. *Advanced Optical Materials* **2015**, *3* (6), 769-773.

54. Watanabe, Y.; Yoshioka, R.; Sasabe, H.; Kamata, T.; Katagiri, H.; Yokoyama, D.; Kido, J., Fundamental functions of peripheral and core pyridine rings in a series of bis-terpyridine derivatives for high-performance organic light-emitting devices. *Journal of Materials Chemistry C* **2016**, *4* (38), 8980-8988.

55. Müller, C. D.; Falcou, A.; Reckefuss, N.; Rojahn, M.; Wiederhirn, V.; Rudati, P.; Frohne, H.; Nuyken, O.; Becker, H.; Meerholz, K., Multi-colour organic light-emitting displays by solution processing. *Nature* **2003**, *421* (6925), 829-833.

56. Chen, M. S.; Lee, O. P.; Niskala, J. R.; Yiu, A. T.; Tassone, C. J.; Schmidt, K.; Beaujuge, P. M.; Onishi, S. S.; Toney, M. F.; Zettl, A.; Fréchet, J. M. J., Enhanced Solid-State Order and Field-Effect Hole Mobility through Control of Nanoscale Polymer Aggregation. *Journal of the American Chemical Society* **2013**, *135* (51), 19229-19236.

57. Noriega, R.; Rivnay, J.; Vandewal, K.; Koch, F. P. V.; Stingelin, N.; Smith, P.; Toney, M. F.; Salleo, A., A general relationship between disorder, aggregation and charge transport in conjugated polymers. *Nature Materials* **2013**, *12* (11), 1038-1044.

58. Pu, Y.-J.; Chiba, T.; Ideta, K.; Takahashi, S.; Aizawa, N.; Hikichi, T.; Kido, J., Fabrication of Organic Light-Emitting Devices Comprising Stacked Light-Emitting Units by Solution-Based Processes. *Advanced Materials* **2015**, *27* (8), 1327-1332.

59. Kulkarni, A. P.; Tonzola, C. J.; Babel, A.; Jenekhe, S. A., Electron Transport Materials for Organic Light-Emitting Diodes. *Chemistry of Materials* **2004**, *16* (23), 4556-4573.

60. Beaujuge, P. M.; Fréchet, J. M. J., Molecular Design and Ordering Effects in π -Functional Materials for Transistor and Solar Cell Applications. *Journal of the American Chemical Society* **2011**, *133* (50), 20009-20029.

61. Iwan, A.; Sek, D., Polymers with triphenylamine units: Photonic and electroactive materials. *Progress in Polymer Science* **2011**, *36* (10), 1277-1325.

62. Xiao, L.; Chen, Z.; Qu, B.; Luo, J.; Kong, S.; Gong, Q.; Kido, J., Recent Progresses on Materials for Electrophosphorescent Organic Light-Emitting Devices. *Advanced Materials* **2011**, *23* (8), 926-952.

63. Xing, X.; Zhong, L.; Zhang, L.; Chen, Z.; Qu, B.; Chen, E.; Xiao, L.; Gong, Q., Essential Differences of Organic Films at the Molecular Level via Vacuum Deposition and Solution Processes for Organic Light-Emitting Diodes. *The Journal of Physical Chemistry C* **2013**, *117* (48), 25405-25408.

64. Verduzco, R.; Li, X.; Pesek, S. L.; Stein, G. E., Structure, function, self-assembly, and applications of bottlebrush copolymers. *Chemical Society Reviews* **2015**, *44* (8), 2405-2420.
65. Müllner, M.; Müller, A. H. E., Cylindrical polymer brushes – Anisotropic building blocks, unimolecular templates and particulate nanocarriers. *Polymer* **2016**, *98*, 389-401.
66. Xie, G.; Martinez, M. R.; Olszewski, M.; Sheiko, S. S.; Matyjaszewski, K., Molecular Bottlebrushes as Novel Materials. *Biomacromolecules* **2019**, *20* (1), 27-54.
67. Crossland, E. J. W.; Cunha, P.; Scroggins, S.; Moratti, S.; Yurchenko, O.; Steiner, U.; Hillmyer, M. A.; Ludwigs, S., Soft-Etch Mesoporous Hole-Conducting Block Copolymer Templates. *ACS Nano* **2010**, *4* (2), 962-966.
68. Williams, P. E.; Moughton, A. O.; Patterson, J. P.; Khodabakhsh, S.; O'Reilly, R. K., Exploring RAFT polymerization for the synthesis of bipolar diblock copolymers and their supramolecular self-assembly. *Polymer Chemistry* **2011**, *2* (3), 720-729.
69. Brendel, J. C.; Liu, F.; Lang, A. S.; Russell, T. P.; Thelakkat, M., Macroscopic Vertical Alignment of Nanodomains in Thin Films of Semiconductor Amphiphilic Block Copolymers. *ACS Nano* **2013**, *7* (7), 6069-6078.
70. Chong, Y. K.; Moad, G.; Rizzardo, E.; Thang, S. H., Thiocarbonylthio End Group Removal from RAFT-Synthesized Polymers by Radical-Induced Reduction. *Macromolecules* **2007**, *40* (13), 4446-4455.
71. Lin, H.-W.; Lin, C.-L.; Chang, H.-H.; Lin, Y.-T.; Wu, C.-C.; Chen, Y.-M.; Chen, R.-T.; Chien, Y.-Y.; Wong, K.-T., Anisotropic optical properties and molecular orientation in vacuum-deposited ter(9,9-diaryluorene)s thin films using spectroscopic ellipsometry. *Journal of Applied Physics* **2004**, *95* (3), 881-886.
72. Müller, D. C.; Braig, T.; Nothofer, H.-G.; Arnoldi, M.; Gross, M.; Scherf, U.; Nuyken, O.; Meerholz, K., Efficient Blue Organic Light-Emitting Diodes with Graded Hole-Transport Layers. *ChemPhysChem* **2000**, *1* (4), 207-211.
73. Yang, X.; Müller, D. C.; Neher, D.; Meerholz, K., Highly Efficient Polymeric Electrophosphorescent Diodes. *Advanced Materials* **2006**, *18* (7), 948-954.
74. Chu, T.-Y.; Song, O.-K., Hole mobility of N,N'-bis(naphthalen-1-yl)-N,N'-bis(phenyl) benzidine investigated by using space-charge-limited currents. *Applied Physics Letters* **2007**, *90* (20), 203512.

75. Uoyama, H.; Goushi, K.; Shizu, K.; Nomura, H.; Adachi, C., Highly efficient organic light-emitting diodes from delayed fluorescence. *Nature* **2012**, *492* (7428), 234-238.
76. Tao, Y.; Yuan, K.; Chen, T.; Xu, P.; Li, H.; Chen, R.; Zheng, C.; Zhang, L.; Huang, W., Thermally Activated Delayed Fluorescence Materials Towards the Breakthrough of Organoelectronics. *Advanced Materials* **2014**, *26* (47), 7931-7958.
77. Feuillastre, S.; Pauton, M.; Gao, L.; Desmarchelier, A.; Riives, A. J.; Prim, D.; Tondelier, D.; Geffroy, B.; Muller, G.; Clavier, G.; Pieters, G., Design and Synthesis of New Circularly Polarized Thermally Activated Delayed Fluorescence Emitters. *Journal of the American Chemical Society* **2016**, *138* (12), 3990-3993.
78. Wu, T.-L.; Huang, M.-J.; Lin, C.-C.; Huang, P.-Y.; Chou, T.-Y.; Chen-Cheng, R.-W.; Lin, H.-W.; Liu, R.-S.; Cheng, C.-H., Diboron compound-based organic light-emitting diodes with high efficiency and reduced efficiency roll-off. *Nature Photonics* **2018**, *12* (4), 235-240.
79. McKeown, N. B.; Badriya, S.; Helliwell, M.; Shkunov, M., The synthesis of robust, polymeric hole-transport materials from oligoarylamine substituted styrenes. *Journal of Materials Chemistry* **2007**, *17* (20), 2088-2094.
80. Thesen, M. W.; Höfer, B.; Debeaux, M.; Janietz, S.; Wedel, A.; Köhler, A.; Johannes, H.-H.; Krueger, H., Hole-transporting host-polymer series consisting of triphenylamine basic structures for phosphorescent polymer light-emitting diodes. *Journal of Polymer Science Part A: Polymer Chemistry* **2010**, *48* (15), 3417-3430.
81. Masui, K.; Nakanotani, H.; Adachi, C., Analysis of exciton annihilation in high-efficiency sky-blue organic light-emitting diodes with thermally activated delayed fluorescence. *Organic Electronics* **2013**, *14* (11), 2721-2726.
82. Tonge, C. M.; Sauv e, E. R.; Cheng, S.; Howard, T. A.; Hudson, Z. M., Multiblock Bottlebrush Nanofibers from Organic Electronic Materials. *Journal of the American Chemical Society* **2018**, *140* (37), 11599-11603.
83. Li, Z.; Ma, J.; Lee, N. S.; Wooley, K. L., Dynamic Cylindrical Assembly of Triblock Copolymers by a Hierarchical Process of Covalent and Supramolecular Interactions. *Journal of the American Chemical Society* **2011**, *133* (5), 1228-1231.
84. Lindner, S. M.; Thelakkat, M., Nanostructures of n-Type Organic Semiconductor in a p-Type Matrix via Self-Assembly of Block Copolymers. *Macromolecules* **2004**, *37* (24), 8832-8835.
85. Andruzzi, L.; Chiellini, E.; Galli, G.; Li, X.; Kang, S. H.; Ober, C. K., Engineering low surface energy polymers through molecular design: synthetic routes to

- fluorinated polystyrene-based block copolymers. *Journal of Materials Chemistry* **2002**, *12* (6), 1684-1692.
86. Eller, M. J.; Verkhoturov, S. V.; Schweikert, E. A., Testing Molecular Homogeneity at the Nanoscale with Massive Cluster Secondary Ion Mass Spectrometry. *Analytical Chemistry* **2016**, *88* (15), 7639-7646.
87. Eller, M. J.; Vinjamuri, A.; Tomlin, B. E.; Schweikert, E. A., Molecular Colocalization Using Massive Gold Cluster Secondary Ion Mass Spectrometry. *Analytical Chemistry* **2018**, *90* (21), 12692-12697.
88. Jiang, Z.; Li, X.; Strzalka, J.; Sprung, M.; Sun, T.; Sandy, A. R.; Narayanan, S.; Lee, D. R.; Wang, J., The dedicated high-resolution grazing-incidence X-ray scattering beamline 8-ID-E at the Advanced Photon Source. *Journal of Synchrotron Radiation* **2012**, *19* (4), 627-636.
89. Jiang, Z., GIXSGUI: a MATLAB toolbox for grazing-incidence X-ray scattering data visualization and reduction, and indexing of buried three-dimensional periodic nanostructured films. *Journal of Applied Crystallography* **2015**, *48* (3), 917-926.
90. Becke, A. D., Density-functional thermochemistry. III. The role of exact exchange. *The Journal of Chemical Physics* **1993**, *98* (7), 5648-5652.
91. Lee, C.; Yang, W.; Parr, R. G., Development of the Colle-Salvetti correlation-energy formula into a functional of the electron density. *Physical Review B* **1988**, *37* (2), 785-789.
92. Miehlich, B.; Savin, A.; Stoll, H.; Preuss, H., Results obtained with the correlation energy density functionals of Becke and Lee, Yang and Parr. *Chemical Physics Letters* **1989**, *157* (3), 200-206.
93. Ditchfield, R.; Hehre, W. J.; Pople, J. A., Self-Consistent Molecular-Orbital Methods. IX. An Extended Gaussian-Type Basis for Molecular-Orbital Studies of Organic Molecules. *The Journal of Chemical Physics* **1971**, *54* (2), 724-728.
94. Hehre, W. J.; Ditchfield, R.; Pople, J. A., Self-Consistent Molecular Orbital Methods. XII. Further Extensions of Gaussian-Type Basis Sets for Use in Molecular Orbital Studies of Organic Molecules. *The Journal of Chemical Physics* **1972**, *56* (5), 2257-2261.
95. Gordon, M. S., Ring strain in cyclopropane, cyclopropene, silacyclopropane, and silacyclopropene. *Journal of the American Chemical Society* **1980**, *102* (25), 7419-7422.
96. *Gaussian 09, Revision A.02*, Gaussian Inc.: Wallingford, CT, 2009.

97. Le Moulllec, Y., Assessment of carbon capture thermodynamic limitation on coal-fired power plant efficiency. *International Journal of Greenhouse Gas Control* **2012**, *7*, 192-201.
98. Moran, A.; Talu, O., Limitations of Portable Pressure Swing Adsorption Processes for Air Separation. *Industrial & Engineering Chemistry Research* **2018**, *57* (35), 11981-11987.
99. Rufford, T. E.; Smart, S.; Watson, G. C. Y.; Graham, B. F.; Boxall, J.; Diniz da Costa, J. C.; May, E. F., The removal of CO₂ and N₂ from natural gas: A review of conventional and emerging process technologies. *Journal of Petroleum Science and Engineering* **2012**, *94-95*, 123-154.
100. Meisen, A.; Shuai, X., Research and development issues in CO₂ capture. *Energy Conversion and Management* **1997**, *38*, S37-S42.
101. Wood, C. D.; Tan, B.; Trewin, A.; Su, F.; Rosseinsky, M. J.; Bradshaw, D.; Sun, Y.; Zhou, L.; Cooper, A. I., Microporous Organic Polymers for Methane Storage. *Advanced Materials* **2008**, *20* (10), 1916-1921.
102. Yu, S.; Tan, H.; Wang, J.; Liu, X.; Zhou, K., High Porosity Supermacroporous Polystyrene Materials with Excellent Oil–Water Separation and Gas Permeability Properties. *ACS Applied Materials & Interfaces* **2015**, *7* (12), 6745-6753.
103. Dawson, R.; Adams, D. J.; Cooper, A. I., Chemical tuning of CO₂ sorption in robust nanoporous organic polymers. *Chemical Science* **2011**, *2* (6), 1173-1177.
104. Han, S. S.; Furukawa, H.; Yaghi, O. M.; Goddard, W. A., Covalent Organic Frameworks as Exceptional Hydrogen Storage Materials. *Journal of the American Chemical Society* **2008**, *130* (35), 11580-11581.
105. Li, B.; Huang, X.; Liang, L.; Tan, B., Synthesis of uniform microporous polymer nanoparticles and their applications for hydrogen storage. *Journal of Materials Chemistry* **2010**, *20* (35), 7444-7450.
106. Du, N.; Robertson, G. P.; Song, J.; Pinnau, I.; Thomas, S.; Guiver, M. D., Polymers of Intrinsic Microporosity Containing Trifluoromethyl and Phenylsulfone Groups as Materials for Membrane Gas Separation. *Macromolecules* **2008**, *41* (24), 9656-9662.
107. Lanson, D.; Ariura, F.; Schappacher, M.; Borsali, R.; Deffieux, A., Comb Copolymers with Polystyrene and Polyisoprene Branches: Effect of Block Topology on Film Morphology. *Macromolecules* **2009**, *42* (12), 3942-3950.

108. Percec, V.; Ahn, C. H.; Ungar, G.; Yeardley, D. J. P.; Möller, M.; Sheiko, S. S., Controlling polymer shape through the self-assembly of dendritic side-groups. *Nature* **1998**, *391*, 161.
109. CO₂ Permeation with Pebax®-based Membranes for Global Warming Reduction. In *Membrane Gas Separation*, pp 255-277.
110. Membrane Engineering: Progress and Potentialities in Gas Separations. In *Membrane Gas Separation*, pp 279-312.
111. Bernardo, P.; Drioli, E.; Golemme, G., Membrane Gas Separation: A Review/State of the Art. *Industrial & Engineering Chemistry Research* **2009**, *48* (10), 4638-4663.
112. Yampolskii, Y., Polymeric Gas Separation Membranes. *Macromolecules* **2012**, *45* (8), 3298-3311.
113. Budd, P. M.; McKeown, N. B., Highly permeable polymers for gas separation membranes. *Polymer Chemistry* **2010**, *1* (1), 63-68.
114. Du, N.; Dal-Cin, M. M.; Robertson, G. P.; Guiver, M. D., Decarboxylation-Induced Cross-Linking of Polymers of Intrinsic Microporosity (PIMs) for Membrane Gas Separation. *Macromolecules* **2012**, *45* (12), 5134-5139.
115. Jeon, J. W.; Kim, D.-G.; Sohn, E.-h.; Yoo, Y.; Kim, Y. S.; Kim, B. G.; Lee, J.-C., Highly Carboxylate-Functionalized Polymers of Intrinsic Microporosity for CO₂-Selective Polymer Membranes. *Macromolecules* **2017**, *50* (20), 8019-8027.
116. Usman, M.; Ahmed, A.; Yu, B.; Peng, Q.; Shen, Y.; Cong, H., A review of different synthetic approaches of amorphous intrinsic microporous polymers and their potential applications in membrane-based gases separation. *European Polymer Journal* **2019**, *120*, 109262.
117. Tan, X.; Hu, C.; Zhu, Z.; Liu, H.; Qu, J., Electrically Pore-Size-Tunable Polypyrrole Membrane for Antifouling and Selective Separation. *Advanced Functional Materials* **2019**, *29* (35), 1903081.
118. Oh, W.; Park, J.-W., Facile Synthesis of Robust and Pore-Size-Tunable Nanoporous Covalent Framework Membrane by Simultaneous Gelation and Phase Separation of Covalent Network/Poly(methyl methacrylate) Mixture. *ACS Applied Materials & Interfaces* **2019**, *11* (35), 32398-32407.
119. Dong, L.; Fan, W.; Zhang, H.; Chen, M.; Zhao, Y., CO₂-Responsive polymer membranes with gas-tunable pore size. *Chemical Communications* **2017**, *53* (69), 9574-9577.

120. Scherman, O. A.; Walker, R.; Grubbs, R. H., Synthesis and Characterization of Stereoregular Ethylene-Vinyl Alcohol Copolymers Made by Ring-Opening Metathesis Polymerization. *Macromolecules* **2005**, *38* (22), 9009-9014.
121. Martinez, H.; Ren, N.; Matta, M. E.; Hillmyer, M. A., Ring-opening metathesis polymerization of 8-membered cyclic olefins. *Polymer Chemistry* **2014**, *5* (11), 3507-3532.
122. Ahmadi, M.; Janakiram, S.; Dai, Z.; Ansaloni, L.; Deng, L., Performance of Mixed Matrix Membranes Containing Porous Two-Dimensional (2D) and Three-Dimensional (3D) Fillers for CO₂ Separation: A Review. *Membranes* **2018**, *8* (3).
123. Aguilar-Lugo, C.; Suárez-García, F.; Hernández, A.; Miguel, J. A.; Lozano, Á. E.; de la Campa, J. G.; Álvarez, C., New Materials for Gas Separation Applications: Mixed Matrix Membranes Made from Linear Polyimides and Porous Polymer Networks Having Lactam Groups. *Industrial & Engineering Chemistry Research* **2019**, *58* (22), 9585-9595.
124. Fan, L.; Kang, Z.; Shen, Y.; Wang, S.; Zhao, H.; Sun, H.; Hu, X.; Sun, H.; Wang, R.; Sun, D., Mixed Matrix Membranes Based on Metal–Organic Frameworks with Tunable Pore Size for CO₂ Separation. *Crystal Growth & Design* **2018**, *18* (8), 4365-4371.
125. Ding, F.; Yakobson, B. I., Challenges in hydrogen adsorptions: from physisorption to chemisorption. *Frontiers of Physics* **2011**, *6* (2), 142-150.
126. Berger, A. H.; Bhowan, A. S., Comparing physisorption and chemisorption solid sorbents for use separating CO₂ from flue gas using temperature swing adsorption. *Energy Procedia* **2011**, *4*, 562-567.
127. Benco, L.; Hafner, J.; Hutschka, F.; Toulhoat, H., Physisorption and Chemisorption of Some n-Hydrocarbons at the Brønsted Acid Site in Zeolites 12-Membered Ring Main Channels: Ab Initio Study of the Gmelinite Structure. *The Journal of Physical Chemistry B* **2003**, *107* (36), 9756-9762.
128. Barajas-Barraza, R. E.; Guirado-López, R. A., Endohedral nitrogen storage in carbon fullerene structures: Physisorption to chemisorption transition with increasing gas pressure. *The Journal of Chemical Physics* **2009**, *130* (23), 234706.
129. Zhu, X.; Hua, Y.; Tian, C.; Abney, C. W.; Zhang, P.; Jin, T.; Liu, G.; Browning, K. L.; Sacci, R. L.; Veith, G. M.; Zhou, H.-C.; Jin, W.; Dai, S., Accelerating Membrane-based CO₂ Separation by Soluble Nanoporous Polymer Networks Produced by Mechanochemical Oxidative Coupling. *Angewandte Chemie International Edition* **2018**, *57* (11), 2816-2821.

130. Sun, L.-B.; Kang, Y.-H.; Shi, Y.-Q.; Jiang, Y.; Liu, X.-Q., Highly Selective Capture of the Greenhouse Gas CO₂ in Polymers. *ACS Sustainable Chemistry & Engineering* **2015**, *3* (12), 3077-3085.
131. Lu, W.; Sculley, J. P.; Yuan, D.; Krishna, R.; Wei, Z.; Zhou, H.-C., Polyamine-Tethered Porous Polymer Networks for Carbon Dioxide Capture from Flue Gas. *Angewandte Chemie International Edition* **2012**, *51* (30), 7480-7484.
132. Hu, X.; Wang, H.; Faul, C. F. J.; Wen, J.; Wei, Y.; Zhu, M.; Liao, Y., A crosslinking alkylation strategy to construct nitrogen-enriched tetraphenylmethane-based porous organic polymers as efficient carbon dioxide and iodine adsorbents. *Chemical Engineering Journal* **2020**, *382*, 122998.
133. Martín, C. F.; Stöckel, E.; Clowes, R.; Adams, D. J.; Cooper, A. I.; Pis, J. J.; Rubiera, F.; Pevida, C., Hypercrosslinked organic polymer networks as potential adsorbents for pre-combustion CO₂ capture. *Journal of Materials Chemistry* **2011**, *21* (14), 5475-5483.
134. Sekizkardes, A. K.; Hammache, S.; Hoffman, J. S.; Hopkinson, D., Polymers of Intrinsic Microporosity Chemical Sorbents Utilizing Primary Amine Appendage Through Acid-Base and Hydrogen-Bonding Interactions. *ACS Applied Materials & Interfaces* **2019**, *11* (34), 30987-30991.
135. Klein, P.; Jötten, H. J.; Aitchison, C. M.; Clowes, R.; Preis, E.; Cooper, A. I.; Sprick, R. S.; Scherf, U., Aromatic polymers made by reductive polydehalogenation of oligocyclic monomers as conjugated polymers of intrinsic microporosity (C-PIMs). *Polymer Chemistry* **2019**, *10* (38), 5200-5205.
136. Patel, H. A.; Hyun Je, S.; Park, J.; Chen, D. P.; Jung, Y.; Yavuz, C. T.; Coskun, A., Unprecedented high-temperature CO₂ selectivity in N₂-phobic nanoporous covalent organic polymers. *Nature Communications* **2013**, *4* (1), 1357.
137. Xiang, Z.; Zhou, X.; Zhou, C.; Zhong, S.; He, X.; Qin, C.; Cao, D., Covalent-organic polymers for carbon dioxide capture. *Journal of Materials Chemistry* **2012**, *22* (42), 22663-22669.
138. Yuan, D.; Zhao, D.; Sun, D.; Zhou, H.-C., An Isoreticular Series of Metal-Organic Frameworks with Dendritic Hexacarboxylate Ligands and Exceptionally High Gas-Uptake Capacity. *Angewandte Chemie International Edition* **2010**, *49* (31), 5357-5361.
139. Banerjee, R.; Furukawa, H.; Britt, D.; Knobler, C.; O’Keeffe, M.; Yaghi, O. M., Control of Pore Size and Functionality in Isoreticular Zeolitic Imidazolate Frameworks and their Carbon Dioxide Selective Capture Properties. *Journal of the American Chemical Society* **2009**, *131* (11), 3875-3877.

140. Couck, S.; Denayer, J. F. M.; Baron, G. V.; Rémy, T.; Gascon, J.; Kapteijn, F., An Amine-Functionalized MIL-53 Metal–Organic Framework with Large Separation Power for CO₂ and CH₄. *Journal of the American Chemical Society* **2009**, *131* (18), 6326-6327.
141. Amir, R. J.; Zhong, S.; Pochan, D. J.; Hawker, C. J., Enzymatically Triggered Self-Assembly of Block Copolymers. *Journal of the American Chemical Society* **2009**, *131* (39), 13949-13951.
142. Li, A.; Ma, J.; Sun, G.; Li, Z.; Cho, S.; Clark, C.; Wooley, K. L., One-pot, facile synthesis of well-defined molecular brush copolymers by a tandem RAFT and ROMP, “Grafting-through” strategy. *Journal of Polymer Science Part A: Polymer Chemistry* **2012**, *50* (9), 1681-1688.
143. Cho, S.; Son, J.; Kim, I.; Ahn, H.; Jang, H.-S.; Joo, S. H.; Park, K. H.; Lee, E.; Kim, Y.; Ahn, S.-k., Asymmetric polystyrene-poly lactide bottlebrush random copolymers: Synthesis, self-assembly and nanoporous structures. *Polymer* **2019**, *175*, 49-56.
144. Lu, W.; Verdegaal, W. M.; Yu, J.; Balbuena, P. B.; Jeong, H.-K.; Zhou, H.-C., Building multiple adsorption sites in porous polymer networks for carbon capture applications. *Energy & Environmental Science* **2013**, *6* (12), 3559-3564.
145. Lee, S. M.; Cho, S. N.; Cheon, J., Anisotropic Shape Control of Colloidal Inorganic Nanocrystals. *Advanced Materials* **2003**, *15* (5), 441-444.
146. Murphy, C. J.; Sau, T. K.; Gole, A. M.; Orendorff, C. J.; Gao, J.; Gou, L.; Hunyadi, S. E.; Li, T., Anisotropic Metal Nanoparticles: Synthesis, Assembly, and Optical Applications. *The Journal of Physical Chemistry B* **2005**, *109* (29), 13857-13870.
147. Bahish, H. B.; Nils, F.; Gert, I.; Jochan, M.; Irina, K. P.; Ravy, P.; Vasilii Yu, R.; Yurii, V. R.; Peter, G. S.; Melvin, C. O., Anisotropy of Optoelectronic Properties and Atomic Ordering in CdGeAs₂. *Japanese Journal of Applied Physics* **2000**, *39* (S1), 353.
148. Thorkelsson, K.; Bai, P.; Xu, T., Self-assembly and applications of anisotropic nanomaterials: A review. *Nano Today* **2015**, *10* (1), 48-66.
149. Nie, Z.; Petukhova, A.; Kumacheva, E., Properties and emerging applications of self-assembled structures made from inorganic nanoparticles. *Nature Nanotechnology* **2009**, *5*, 15.
150. Wang, J.; Gudixsen, M. S.; Duan, X.; Cui, Y.; Lieber, C. M., Highly Polarized Photoluminescence and Photodetection from Single Indium Phosphide Nanowires. *Science* **2001**, *293* (5534), 1455.

151. Golberg, D.; Mitome, M.; Yin, L. W.; Bando, Y., In situ growth of Indium nanocrystals on InP nanorods mediated by electron beam of transmission electron microscope. *Chemical Physics Letters* **2005**, *416* (4), 321-326.
152. Myung-Hyun, L.; Jung-Jin, J.; Woon Jin, C.; Seung Koo, P.; Min-su, K.; Hong Seok, S.; Hyo Jin, K.; Ki-Won, J.; Sang Il, S. In *Optical and structural characterization of InP nanorods*, International Conference on Indium Phosphide and Related Materials, 2005, 8-12 May 2005; 2005; pp 283-285.
153. Ahrenkiel, S. P.; Mičić, O. I.; Miedaner, A.; Curtis, C. J.; Nedeljković, J. M.; Nozik, A. J., Synthesis and Characterization of Colloidal InP Quantum Rods. *Nano Letters* **2003**, *3* (6), 833-837.
154. Zhang, M.; Drechsler, M.; Müller, A. H. E., Template-Controlled Synthesis of Wire-Like Cadmium Sulfide Nanoparticle Assemblies within Core-Shell Cylindrical Polymer Brushes. *Chemistry of Materials* **2004**, *16* (3), 537-543.
155. Djalali, R.; Li, S.-Y.; Schmidt, M., Amphipolar Core-Shell Cylindrical Brushes as Templates for the Formation of Gold Clusters and Nanowires. *Macromolecules* **2002**, *35* (11), 4282-4288.
156. Pang, X.; He, Y.; Jung, J.; Lin, Z., 1D nanocrystals with precisely controlled dimensions, compositions, and architectures. *Science* **2016**, *353* (6305), 1268.
157. Yuan, J.; Müller, A. H. E., One-dimensional organic-inorganic hybrid nanomaterials. *Polymer* **2010**, *51* (18), 4015-4036.
158. Hood, M. A.; Mari, M.; Muñoz-Espí, R., Synthetic Strategies in the Preparation of Polymer/Inorganic Hybrid Nanoparticles. *Materials* **2014**, *7* (5), 4057-4087.
159. Choucair, A.; Lavigueur, C.; Eisenberg, A., Polystyrene-b-poly(acrylic acid) Vesicle Size Control Using Solution Properties and Hydrophilic Block Length. *Langmuir* **2004**, *20* (10), 3894-3900.
160. Burguière, C.; Pascual, S.; Bui, C.; Vairon, J.-P.; Charleux, B.; Davis, K. A.; Matyjaszewski, K.; Bétremieux, I., Block Copolymers of Poly(styrene) and Poly(acrylic acid) of Various Molar Masses, Topologies, and Compositions Prepared via Controlled/Living Radical Polymerization. Application as Stabilizers in Emulsion Polymerization. *Macromolecules* **2001**, *34* (13), 4439-4450.
161. Mai, Y.; Eisenberg, A., Controlled Incorporation of Particles into the Central Portion of Block Copolymer Rods and Micelles. *Macromolecules* **2011**, *44* (8), 3179-3183.

162. Burke, S. E.; Eisenberg, A., Kinetics and Mechanisms of the Sphere-to-Rod and Rod-to-Sphere Transitions in the Ternary System PS310-b-PAA52/Dioxane/Water. *Langmuir* **2001**, *17* (21), 6705-6714.
163. Liang, H.; Morgan, B. J.; Xie, G.; Martinez, M. R.; Zhulina, E. B.; Matyjaszewski, K.; Sheiko, S. S.; Dobrynin, A. V., Universality of the Entanglement Plateau Modulus of Comb and Bottlebrush Polymer Melts. *Macromolecules* **2018**, *51* (23), 10028-10039.
164. Liang, H.; Grest, G. S.; Dobrynin, A. V., Brush-Like Polymers and Entanglements: From Linear Chains to Filaments. *ACS Macro Letters* **2019**, *8* (10), 1328-1333.
165. Sheiko, S. S.; Prokhorova, S. A.; Beers, K. L.; Matyjaszewski, K.; Potemkin, I. I.; Khokhlov, A. R.; Möller, M., Single Molecule Rod–Globule Phase Transition for Brush Molecules at a Flat Interface. *Macromolecules* **2001**, *34* (23), 8354-8360.
166. Xu, Y.; Bolisetty, S.; Drechsler, M.; Fang, B.; Yuan, J.; Harnau, L.; Ballauff, M.; Müller, A. H. E., Manipulating cylindrical polyelectrolyte brushes on the nanoscale by counterions: collapse transition to helical structures. *Soft Matter* **2009**, *5* (2), 379-384.
167. Li, Z.; Ma, J.; Cheng, C.; Zhang, K.; Wooley, K. L., Synthesis of Hetero-Grafted Amphiphilic Diblock Molecular Brushes and Their Self-Assembly in Aqueous Medium. *Macromolecules* **2010**, *43* (3), 1182-1184.
168. Knapp-Reed, B.; Mahandru, G. M.; Montgomery, J., Access to Macrocyclic Endocyclic and Exocyclic Allylic Alcohols by Nickel-Catalyzed Reductive Cyclization of Ynals. *Journal of the American Chemical Society* **2005**, *127* (38), 13156-13157.
169. Cravatt, B. F.; Lerner, R. A.; Boger, D. L., Structure Determination of an Endogenous Sleep-Inducing Lipid, cis-9-Octadecenamide (Oleamide): A Synthetic Approach to the Chemical Analysis of Trace Quantities of a Natural Product. *Journal of the American Chemical Society* **1996**, *118* (3), 580-590.
170. Zou, Y.; Mouhib, H.; Stahl, W.; Goeke, A.; Wang, Q.; Kraft, P., Efficient Macrocyclization by a Novel Oxy-Oxonio-Cope Reaction: Synthesis and Olfactory Properties of New Macrocyclic Musks. *Chemistry – A European Journal* **2012**, *18* (23), 7010-7015.